GSSI

Gran Sasso Science Institute

Search for neutrinoless double beta decay of ^{128}Te with the CUORE experiment

Astroparticle Physics

PhD thesis

submitted March 1, 2021

Advisors

Oliviero Cremonesi
INFN, Sezione di Milano - Bicocca

Paolo Gorla
INFN, Laboratori Nazionali del Gran Sasso

PhD Candidate

Valentina Dompè
Gran Sasso Science Institute

Gran Sasso Science Institute

XXXIII Cycle – A. Y. 2017-2020

Search for neutrinoless double beta decay of ^{128}Te with the CUORE experiment

V. Dompè

Abstract

The observation of the neutrinoless double beta decay ($0\nu\beta\beta$) would unambiguously demonstrate that the lepton number is not a fundamental symmetry of nature, and would establish that neutrinos are Majorana particles. This would represent a manifest signature of Physics beyond the Standard Model: for this reason, the search of this decay is currently one of the priorities in Neutrino Physics. A measurement of the half life of this decay would also provide important indications on the neutrino absolute mass scale and ordering, which are still unknown properties of this lepton. The Cryogenic Underground Observatory for Rare Events (CUORE) at Laboratori Nazionali del Gran Sasso of INFN, in Italy, is an outstanding experiment in the search of $0\nu\beta\beta$ decay, operating 988 TeO_2 bolometric crystals at the cryogenic temperature of 11 mK. Its main goal is to investigate the $0\nu\beta\beta$ decay of ^{130}Te, but its ton-scale mass and low background make this detector sensitive to other rare processes as well. The main outcome of my PhD thesis regards the search of the $0\nu\beta\beta$ decay of the ^{128}Te, another isotope of tellurium at a high natural isotopic abundance of 31.7%. I found no evidence of this decay, and by means of a custom developed Bayesian analysis code I extracted 90% C.I. limits on the signal rate and half life of this process. The results obtained in this work improve the past limit on the half life of such decay by a factor of $\sim$33, and represent the most stringent limits on this isotope currently in literature.

Contents

Introduction

The search for neutrinoless double beta decay ($0\nu\beta\beta$) represents nowadays one of the leading topics of Neutrino Physics. The interest on the investigation of this process was boosted by the observation of the neutrino flavor oscillations, which demonstrated that neutrinos are massive particles. The $0\nu\beta\beta$ decay violates the lepton number (L) by two units: its observation would establish that L is not a symmetry of nature and that neutrinos are Majorana particles, providing a clear signature of Physics beyond the Standard Model. This would also represent an ingredient to the understanding of the matter-antimatter asymmetry in the Universe via leptogenesis. In addition, since the amplitude of this decay would be proportional to the neutrino mass, its observation would give an important indication on the absolute mass scale and ordering of this lepton.

One of the leading experiments in the $0\nu\beta\beta$ decay search landscape is the Cryogenic Underground Observatory for Rare Events (CUORE), located at the Laboratori Nazionali del Gran Sasso (LNGS) of INFN, in Italy. It consists of an array of 988 cryogenic TeO_2 bolometers operated at a base temperature of 11 mK; with a total TeO_2 mass of 742 kg corresponding to 206 kg of ^{130}Te, CUORE has the main goal of investigating the $0\nu\beta\beta$ decay of ^{130}Te. Thanks to its ton-scale mass and to the low achieved background level, CUORE is also suitable for the search of other rare processes, one of these being the $0\nu\beta\beta$ decay of ^{128}Te. The ^{128}Te is the second high natural abundance isotope of tellurium (37.1%), and is present in the CUORE detectors in the amount of 188 kg. The CUORE data taking started at the beginning of 2017, and after optimization campaigns that allowed to achieve stable and reliable detector conditions it is currently proceeding smoothly.

My PhD work took place within the CUORE experiment at LNGS. My work was focused on the search of the $0\nu\beta\beta$ decay of ^{128}Te: the outcome of this research resulted in the most stringent limits on this process currently in literature. I provided several contributions that allowed to achieve this final result. I took part to the detector operation activities, aimed at providing and maintaining optimal conditions during the data taking, as well as in the data processing and analysis. Within the Background Model working group, I was involved in the study and the understanding of the CUORE measured spectrum.

This PhD thesis is organized as follows. In chapter 1, a brief outline of the Neutrino milestones is first reported, together with an overview of the main theoretical aspects of the neutrinos in the Standard Model theory as well as in the Majorana formulation. In this context, the important role of the $0\nu\beta\beta$ decay is introduced and its phenomenology is described; a discussion on the experimental aspects and on the current status of the $0\nu\beta\beta$ decay search is then provided. Chapter 2 is dedicated to the detailed description of the CUORE experimental setup. A review on how the bolometric technique, namely the detection technique adopted by CUORE, has developed during the last decades is outlined, and the precursor experiments that demonstrated the CUORE feasibility are briefly presented. The bolometric technique is then illustrated, together with the operational principles of this type of detectors. The CUORE crystals and cryogenic system are then detailed, as well as the adopted cooling techniques. Chapter 3 reports on the steps that bring the raw data waveforms acquired by the CUORE bolometers to the high level data processing. The DAQ system and the software trigger algorithms aimed at identifying the particle pulses are described. The organization of the CUORE data collection and the procedures that are constantly applied for the data quality real-time monitoring are then presented, as well as all the data processing sequences performed with the CUORE software to extract the physical information from the triggered waveforms. Chapter 4 can be divided into two parts: first, a description of the study performed to identify and constrain the various contributions of the CUORE measured spectrum is provided. The Monte Carlo (MC) simulation software aimed at evaluating the effect of the background sources in the CUORE detector are described, and the Bayesian analysis addressed to the Background Model reconstruction is presented. The second part of the chapter includes original contributions that I provided in the study of the alpha region of the CUORE energy spectrum, to improve the present Background Model. In Chapter 5, the latest CUORE results on the search of the ^{130}Te $0\nu\beta\beta$ decay are presented together with the adopted analysis technique, as well as the most precise measurement obtained for the ^{130}Te $2\nu\beta\beta$ decay half life resulting from the Background Model analysis. Finally, the hearth of this PhD thesis work is illustrated in chapter 6: this includes the original work that I performed on the entire analysis of the search of the $0\nu\beta\beta$ decay in ^{128}Te. The motivations for this study and the presently available results are outlined. Then, the detailed description of the Bayesian analysis procedure and the model that I developed to extract the limit on the half life of this decay is provided. The tests that I performed to validate the fit model are described, and the obtained results are finally presented and discussed: as an outcome of this work, it was possible to set the most stringent limits on the $0\nu\beta\beta$ decay of ^{128}Te currently in literature, improving the last available limit by a factor $\sim$33. The CUORE median exclusion sensitivity on this process is also reported on. These results are summarized in the conclusion chapter of this thesis (chap. 7), together with a résumé of the contributions that I provided to the CUORE Collaboration during my PhD.

Chapter 1

Neutrino Physics and Double-Beta Decay

In 1937, just seven years after Wolfgang Pauli made the first prediction of the neutrinos existence and way before their observation, Ettore Majorana introduced a new formulation of the Dirac theory of fermions. Differently from the latter, which includes negative energy states and requires four-component spinors, the Majorana formulation does not require the existence of distinct representations for particles and antiparticles in case of neutral charge[1]. For neutrinos this leads to their physical identity with antineutrinos. This has been considered an exotic theory for decades since its first formulation, until the observation of neutrino flavor oscillations about 60 years later unexpectedly demonstrated that, contrarily to the Standard Model representation, these particles have a very small non-zero mass. The Dirac and Majorana representations are coincident in case of massless neutrinos; if not, a single Majorana quantum field can effectively describe a massive neutrino, providing a new alternative mechanism to the existence of its mass as an extension of the Standard Model.

The Majorana nature of neutrinos can be experimentally confirmed if a lepton number violating process is observed. During the past years, it has been established that among the candidate transitions of this type (see [2] and references therein), the *neutrinoless double beta decay* represents the most feasible process to be looking for. This is a second-order weak transition consisting of two neutrons transmuting into two protons with the emission of two electrons but without the emission of neutrinos, thus violating the total lepton number conservation by two units. Many experiments are nowadays putting a lot of effort in the realization of extremely challenging technological infrastructures to search for this process, since its observation would also shed light on several open issues in Neutrino Physics, such as the neutrinos absolute mass scale and ordering. In addition, establishing that the lepton number is not a symmetry of nature would provide a fundamental contribution to the understanding of the matter-antimatter asymmetry in the Universe, as this decay would be a matter-creating process without emission of antimatter.

1.1 Brief history of Neutrino Physics

The introduction of neutrinos in Particle Physics was due to Wolfgang Pauli in 1930. At that time, the atomic nucleus was believed to be composed by protons and electrons, and the beta decay was expected to correspond to the emission of one of the pre-existing electrons, characterized therefore by a mono-energetic spectrum according to the reaction $(A, Z) \rightarrow (A, Z+1)+e^{-}$. Nevertheless, experiments on beta decay showed that the emitted electrons were characterized by a continuum and wide spectrum of energy, giving rise to an apparent non-conservation of energy. In this framework, Pauli hypothesized the existence of a new neutral massive particle with spin 1/2 in the nucleus that was emitted in the final state of the beta decay with the electron, *as a desperate remedy to save [...] the law of conservation of energy*. Firstly, this exotic proposal was not seriously considered by the scientific community, and Pauli himself was not convinced of the existence of this particle. This instead raised the interest of Enrico Fermi, that three years later formulated a theory of beta decay emission including the new Pauli's particle and calling it *neutrino* for the first time[3][4].

The neutrino experimental detection was claimed only in 1956 by Clyde Cowan and Frederik Reines, who were able to observe the antineutrinos produced by fission-fragment decays in a nuclear reactor interacting with a hydrogenous liquid scintillator target via inverse beta decay $\bar{\nu_e} + p \rightarrow e^+ + n$ [5]. Few years later, in 1962, Leon Lederman, Melvin Schwartz and Jack Steinberger discovered the muon neutrino at the Brookhaven National Laboratories, demonstrating that neutrinos produced in association with muons are distinct from those produced with electrons, and thus that neutrinos exist in more than one flavor[6]. A third neutrino, the tau neutrino, was later discovered in 2000 by the DONUT experiment[7], completing the three lepton family doublets of the Standard Model.

1.1.1 Neutrino flavor oscillations

At the time of the first Standard Model formulation, experimental results were suggesting neutrinos to be massless leptons. Thus, they were introduced in the Standard Model theory with zero mass, and there were no hints to believe that this was not the case until the *neutrino flavor oscillations* were observed by solar and atmospheric neutrinos experiments. In 2015, A. B. McDonald and T. Kajita were awarded with the Nobel prize for this discovery[8][9], which is a crucial milestone of Neutrino Physics as it demonstrates that neutrinos have non-zero mass. In this situation, the flavor eigenstate ν_l produced in the weak charged current interaction of a lepton $l = e, \mu, \tau$ is a linear combination of the mass eigenstates ν_i[10]:

$$|\nu_l\rangle = \sum_{i=1}^{3} U_{li}^{*}|\nu_i\rangle \tag{1.1}$$

where U_{li}^{*} is the 3×3 Pontecorvo-Maki-Nakagawa-Sakata (PMNS) unitary mixing matrix, assuming 3 species of light neutrinos in this description. In case of Dirac neutrinos, the

PMNS matrix is parametrized with 3 mixing angles θ_{ij} and 1 Dirac CP-violation phase δ_{CP}:

$$U = \begin{pmatrix} c_{12}c_{13} & s_{12}c_{13} & s_{13}e^{-i\delta_{CP}} \\ -s_{12}c_{23} - c_{12}s_{13}s_{23}e^{i\delta_{CP}} & c_{12}c_{23} - s_{12}s_{13}s_{23}e^{i\delta_{CP}} & c_{13}s_{23} \\ s_{12}s_{23} - c_{12}s_{13}c_{23}e^{i\delta_{CP}} & -c_{12}s_{23} - s_{12}s_{13}c_{23}e^{i\delta_{CP}} & c_{13}c_{23} \end{pmatrix} \tag{1.2}$$

where $c_{ij} = \cos\theta_{ij}$ and $s_{ij} = \sin\theta_{ij}$. The time evolution of the lepton eigenstate in eq. 1.1 is given by:

$$|\nu_l(t)\rangle = \sum_{i=1}^{3} U^*_{li}|\nu_i(t)\rangle \tag{1.3}$$

In case of neutrino propagation in vacuum, the three mass eigenstates independently evolve in time according to $|\nu_i(t)\rangle = e^{-iE_it}|\nu_i(0)\rangle$, where $E_i = \sqrt{p^2 + m_i^2}$ is the energy of the eigenstate ν_i and m_i is its mass. As a consequence, the occurrence of a charged current interaction at time t after the neutrino has travelled a distance L can give rise to a charged lepton with any of the three flavors with a time dependent probability. The probability that a neutrino with flavor l is measured with a flavor l' at time t is represented as:

$$P_{l\to l'} = |\langle\nu_{l'}|\nu_l(t)\rangle|^2 = |\sum_{i=1}^{3}\sum_{j=1}^{3} U^*_{lj}U_{l'i}\langle\nu_i|\nu_j(t)\rangle|^2 \tag{1.4}$$

Being neutrinos ultra-relativistic in practical cases, it is possible to approximate $E_i \simeq p + \frac{m_i^2}{2p}$. Exploiting the orthogonality of the mass eigenstates $\langle\nu_j|\nu_i\rangle = \delta_{ij}$, the probability $P_{l\to l'}$ can be re-written as:

$$P_{l\to l'} = \delta_{ll'} - 4\sum_{j<i}^{3} \mathrm{Re}[U_{lj}U^*_{l'j}U^*_{li}U_{l'i}]\sin^2 X_{ji} + 2\sum_{j<i}^{3} \mathrm{Im}[U_{lj}U^*_{l'j}U^*_{li}U_{l'i}]\sin 2X_{ji} \tag{1.5}$$

where

$$X_{ji} = \frac{(m_j^2 - m_i^2)L}{4E} = 1.267\,\frac{\Delta m_{ji}^2}{\mathrm{eV}^2}\,\frac{L/E}{\mathrm{m/MeV}} \tag{1.6}$$

This expression shows that the probability of changing flavor for a neutrino with energy E travelling a distance L does not depend on the absolute values of the masses m_i but only on the difference of the squared masses $\Delta m_{ji}^2 = m_j^2 - m_i^2$. At this point it is straightforward that the neutrino oscillations phenomenon is admitted only if neutrinos have non-zero mass, and more specifically, if they have different masses. Oscillations experiments allowed to measure the values of the mass-squared differences Δm_{ji}^2 and the mixing angles θ_{ij} [11]; in case of neutrinos propagating through a dense medium, oscillation is also sensitive to the sign of Δm_{ji}^2, due to the coherent interaction of neutrinos with matter (MSW effect).

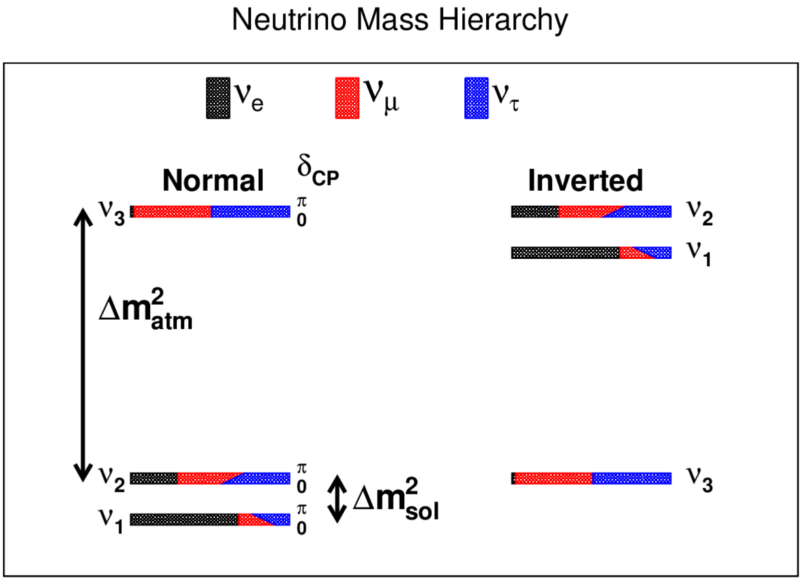

FIG. 1.1: Representation of normal and inverted hierarchy for neutrino masses, both compatible with the measured values of squared mass differences from solar and atmospheric neutrino oscillations experiments. Taken from [13].

Thanks to the measurement of oscillations from neutrinos propagating through the Sun, it was possible to establish that $\Delta m^2_{21} > 0$ [12]. On the contrary, determining the sign of m^2_{31}, whose value is extracted from atmospheric neutrinos oscillations in vacuum, is way more challenging and is still unknown. The uncertainty on m^2_{31} sign gives rise to two scenarios, depending on which neutrino mass eigenstate is the lighter among m_1 and m_3: the Normal Hierarchy (NH), according to which $m_1 < m_2 < m_3$, and the Inverted Hierarchy (IH), where $m_3 < m_1 < m_2$ (fig. 1.1). A third possibility, the Quasi-Degenerate case, occurs if the mass differences are much smaller than the absolute scale, namely $m_1 \simeq m_2 \simeq m_3$.

1.2 Neutrinos in Standard Model

The Standard Model (SM) is a non-abelian gauge quantum field theory with symmetry $\mathrm{U}(1)_Y \times \mathrm{SU}(2)_L \times \mathrm{SU}(3)_C$ describing how the fermions interact ruled by three fundamental forces, mediated by bosons[10]. The neutrino fields are singlets of the group $\mathrm{U}(1)_{EM} \times \mathrm{SU}(3)_C$, since they are not subject to electromagnetic nor to strong interaction. Neutrinos are included in the SM as neutral massless particles taking part to three left-handed doublets together with the associated charged leptons:

$$\begin{pmatrix} \nu_l \\ l \end{pmatrix}_L \tag{1.7}$$

where $l = e, \mu, \tau$ indicates the lepton flavor. The right-handed charged leptons are instead represented by SU(2) singlets. The chiral projectors applied to the lepton fields to get the left-handed and right-handed components are defined as $P_{\substack{L\\R}} = \frac{1 \mp \gamma^5}{2}$. Left-handed neutrinos are also called *active neutrinos*: this is the only component included in the SM, since experimental results have shown that only left-handed neutrinos and right-handed antineutrinos are observed[14]. Thus there are only three active neutrinos[1], namely $\nu_{eL}, \nu_{\mu L}, \nu_{\tau L}$. This situation is described in the SM by the first of the so-called Weyl equations:

$$\begin{cases} i\partial\!\!\!/ \psi_L - m\psi_R = 0 \\ i\partial\!\!\!/ \psi_R - m\psi_L = 0 \end{cases} \tag{1.8}$$

that are obtained from the Dirac equation by decoupling the fermion field into its left-handed and right-handed components $\psi = \psi_L + \psi_R$. In case of non-zero mass these two expressions are coupled, while if the mass vanishes as for neutrinos, they evolve in time independently. It can be shown that by substituting the left component $\psi_L = \left(\frac{1-\gamma_5}{2}\right)\psi$ into the first of 1.8 in absence of mass, a parity-violating equation is obtained. According to this equation, $+1$ helicity is associated to particles and -1 to antiparticles, just as it is observed for neutrinos and antineutrinos, due to the equivalence of helicity and chirality for zero-mass particles.

The discovery of flavor oscillations provided the unambiguous demonstration that neutrinos have non-zero mass. This makes the SM incomplete, since it cannot explain the experimental observation of this phenomenon. In this situation, it becomes necessary to introduce a gauge invariant mass term for neutrinos in the SM Lagrangian: as an attempt to do this within the SM, it is worth to adopt the same mechanism through which the charged leptons and the quarks assume their masses. This happens due to a spontaneous symmetry breaking via Higgs mechanism. Hence, a *Dirac mass term* can be generated in the Lagrangian for neutrinos coupling the scalar Higgs field H via Yukawa interaction with the right-handed and the left-handed components of a fermion field:

$$\mathcal{L}_{Y\,l} = Y^l_{ij}\bar{\psi}^i_L H \psi^j_R + h.c. \tag{1.9}$$

where i,j are flavor indexes and Y^l_{ij} is the 3×3 Yukawa coupling matrix for leptons. The symmetry breaking is due to the fact that the vacuum expectation value of the Higgs field is $|H| = v \neq 0$. This produces a mass for the charged leptons given by:

$$m^l_{ij} = Y^l_{ij}\frac{v}{\sqrt{2}} \tag{1.10}$$

Since the neutrino right-handed component ν_R is not included in the SM, the Higgs mechanism cannot generate the neutrino masses, that hence require some process beyond the SM.

[1] The number of left-handed neutrino states can be inferred by measuring the total decay width of the weak mediator Z_0 into neutrinos through neutral current interaction. From this measurement, $N_\nu = 2.984 \pm 0.008$ is obtained[10].

1.3 Dirac and Majorana neutrinos

Experimental results indicate that 3 light neutrinos coupled to Z exist in nature, thus neither more nor less than this should be included in any SM extension[10]. Instead, it is possible to build the new term in the Lagrangian introducing *sterile neutrinos*, as they are not subject to any SM interaction and thus the gauge invariance would be respected. The simplest thing is to introduce ν_R as sterile neutrino and to generate a mass term in the SM Lagrangian via Higgs mechanism, just as for charged leptons[15]. This *Dirac mass term* takes the form $M_D(\bar{\nu_R}\nu_L + \bar{\nu_L}\nu_R)$, where M_D is the *Dirac mass*. In this framework, four distinct left-/right-handed neutrino/antineutrino states are involved, and the total lepton number symmetry is conserved. However, this scenario has a weakness, since it cannot explain the smallness of neutrino mass with respect to charged leptons and quarks. Indeed, if the same mechanism is adopted to generate their masses, it is reasonable to expect that the Yukawa coefficients for neutrinos are of the same order of the others.

There is another way to construct the neutrino mass term after the inclusion of ν_R in the theory. A *Majorana mass term* can be added, and the most general form of the SM Lagrangian for neutrinos contains both the Dirac and the Majorana contributions:

$$\mathcal{L}_{D,M} = M_D(\bar{\nu_R}\nu_L + \bar{\nu_L}\nu_R) + M\nu_R^T C^{-1}\nu_R + h.c. \tag{1.11}$$

where the coupling constant M is the *Majorana mass*, and C is the charge conjugation operator. It can be noticed that only neutrino fields are involved in the new term: these fields satisfy the *Majorana hypothesis*, according to which there is no need for a system of elementary neutral particles to presume the existence of antiparticles as distinct entities. A Majorana field thus obeys

$$\psi = \psi^C = C\bar{\psi}^T \tag{1.12}$$

and the left-handed and right-handed components are not independent:

$$\psi_R = C\bar{\psi_L}^T \tag{1.13}$$

Contrarily to the 4-dimensional Dirac field, a Majorana field has only 2 components with different helicity states. In this sense, the antiparticle field becomes unnecessary. The consequence of this assumption is that the total lepton number L is not conserved, in fact it is violated by two units in the Majorana term of 1.11. This does not have implications on the structure of the SM, since the lepton number symmetry is not intrinsic and imposed in the model, but it is a global accidental symmetry that comes as a consequence of the gauge invariance and the fields representation.

The just described Majorana theory can also account for in a natural way the smallness of the neutrino mass with the *see-saw mechanism*[15]. This can be briefly described taking advantage of the Feynman diagrams shown in figure 1.2. The Dirac mass term gives rise to the top-left vertex, where a left-handed neutrino is converted into a right-handed one.

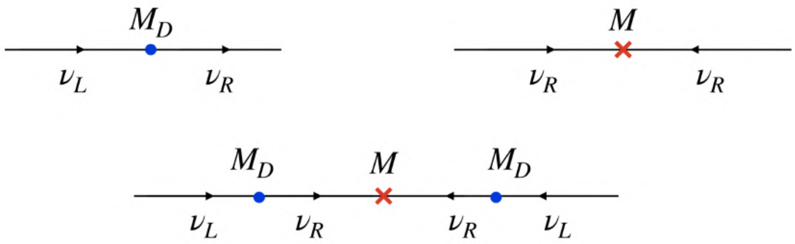

FIG. 1.2: Top-left: Dirac mass term vertex. Top-right: Majorana mass vertex. Bottom-center: combined Dirac and Majorana vertexes. Adapted from [15].

The Majorana mass term instead originates the top-right vertex, in which the total lepton number is violated; combining these two vertexes, the bottom-central representation is obtained. This third-order process can be expressed as a Majorana term for left-handed neutrinos: it cannot be explicitly written in the SM Lagrangian as it is not gauge invariant due to the presence of the active ν_L fields, but it induces a mass m for left-handed neutrinos as well. The transition amplitude of this diagram is proportional to $M_D \frac{i}{\not{p}-M} M_D$, and this provides an evaluation of m:

$$m \approx \frac{M_D^2}{M} \tag{1.14}$$

In eq. 1.14 a very large value of the Majorana mass M has been assumed, as it is expected to be of the order of the unification scale in the Grand Unified Theories (GUT). The Dirac mass M_D is reasonably of the same order of the charged leptons ones as it is generated via the same mechanism, hence $M_D \ll M$. In light of these considerations and from 1.14, it follows that $m \ll M_D$, namely the mass m induced on ν_L is predicted to be several order of magnitudes smaller than that of charged leptons which originates from the Dirac term only, provided that the Majorana term generates a mass M of the unification scale for ν_R.

The investigation of the Dirac or Majorana nature of neutrinos is one of the most important open issues of modern Particle Physics. Oscillation experiments cannot provide information on this aspect. In case of 3 Majorana neutrinos, the PMNS mixing matrix in eq. 1.2 is multiplied by a term containing 2 additional real parameters, namely the Majorana phases $\eta_{1,2}$:

$$U_M = U \times \mathrm{diag}(1, e^{i\eta_1}, e^{i\eta_2}) \tag{1.15}$$

However, if this expression is substituted in 1.5, it can be seen that the Majorana phases nullify in the oscillation probability, therefore this is not affected by the Majorana or Dirac nature of neutrinos. This can be instead probed with the search of the *neutrinoless double beta decay*, a lepton number violating process whose observation would confirm the Majorana nature of neutrinos. The next section is dedicated to a detailed description of this theorized reaction and the implications related to its possible observation.

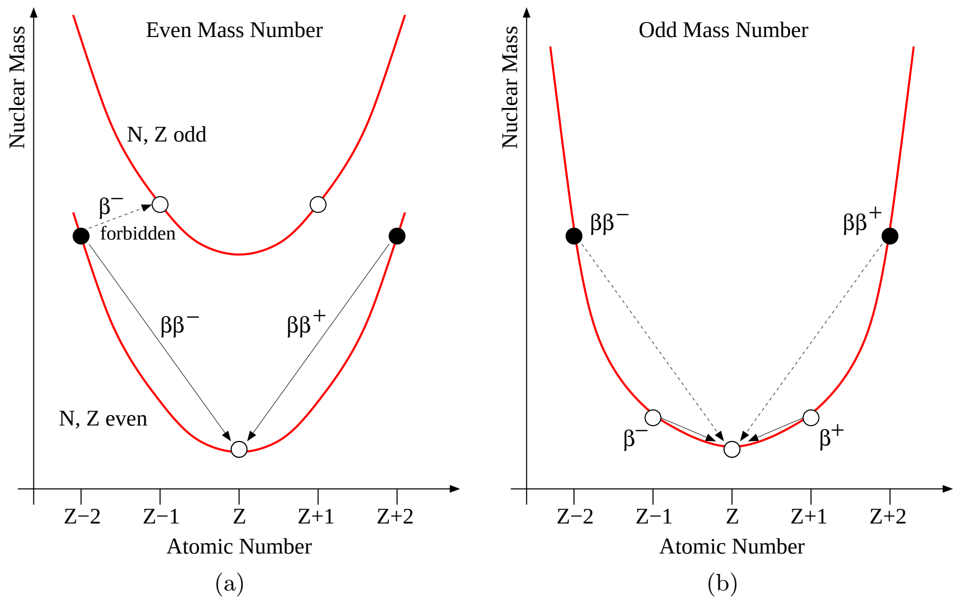

FIG. 1.3: Nuclear mass as a function of the atomic number for even (a) and odd (b) mass number nuclei. For some even-even nuclei, the single beta decay is energetically forbidden and the double beta decay search is favoured. For odd mass nuclei, both single and double beta decay are allowed, but the much higher decay rate of the first disturbs the observation of the latter.

1.4 Double beta decay

The double beta decay is a rare second-order Fermi interaction in which a nucleus (A, Z) transforms into its isobar $(A, Z+2)$ by the simultaneous transmutation of two neutrons into two protons. The most suitable candidates for the experimental observation of this interaction are the nuclei characterized by an even number of protons and an even number of neutrons, where the single beta decay is energetically forbidden while the double beta decay is favoured (fig. 1.3). The Standard Model admits the double beta decay with the emission of two electrons and two antineutrinos in the final state ($2\nu\beta\beta$ decay), so that the lepton number conservation holds:

$$(A, Z) \rightarrow (A, Z+2) + 2e^- + 2\bar{\nu}_e \tag{1.16}$$

A Feynman representation of this reaction is shown in figure 1.4-(a). The $2\nu\beta\beta$ decay was introduced for the first time by M. Goeppert-Mayer in 1935 when she calculated, from the Fermi theory of beta disintegration, that the expected half-life for this process would have been greater than 10^{17} years[17]. The first direct detection was in 1987 for ^{82}Se[18], and nowadays it has been measured for 11 even-even nuclei[19]: ^{48}Ca, ^{76}Ge, ^{82}Se, ^{96}Zr, ^{100}Mo, ^{116}Cd, ^{128,130}Te, ^{136}Xe, ^{150}Nd and ^{238}U. The obtained half-lives are larger than 10^{18}-10^{22} years. This process can be observed by measuring the summed energy of the two electrons. Due to the presence of the two neutrinos in the final state carrying part of the momentum, the measured energy form a continuous spectrum from 0 to the Q-value of the reaction

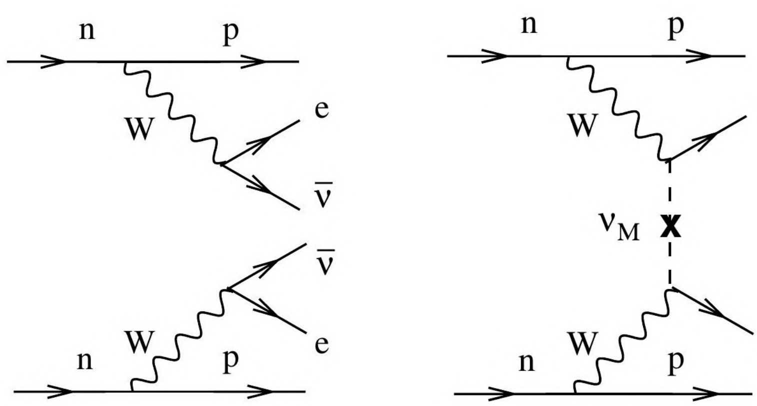

(a) (b)

FIG. 1.4: Feynman diagrams of the SM admitted two-neutrino double beta decay (a) and the lepton number violating neutrinoless double beta decay via light Majorana neutrino exchange (b). Taken from [16].

(fig. 1.5), which is given by

$$Q_{\beta\beta} = (M_p - M_d - 2m_e)c^2 \tag{1.17}$$

where M_p, M_d and m_e are the masses of the parent nucleus, the daughter nucleus and the electrons respectively. Both the neutrino masses and the energy of the recoiling nucleus are neglected. As it will be discussed later in sec. 1.5 and 5.2, the $2\nu\beta\beta$ decay spectrum represents an irreducible background source for the search of the neutrinoless double beta decay.

1.4.1 Neutrinoless double beta decay

The nature of neutrinos can be probed with the observation of the neutrinoless double beta decay ($0\nu\beta\beta$). This hypothesized process consists of a nucleus (A, Z) decaying into its daughter $(A, Z + 2)$ with the emission of two electrons and no neutrinos in the final state:

$$(A, Z) \rightarrow (A, Z + 2) + 2e^- \tag{1.18}$$

Differently from the $2\nu\beta\beta$ case, in this situation the two electrons carry the total amount of energy, thus the expected signal is a monochromatic peak at the Q-value (fig. 1.5).

Several implications of fundamental interest for Particle Physics would follow the observation of this lepton number violating process. First of all, it would unambiguously prove that the neutrino is a Majorana fermion, demonstrating that *there is no need to assume the existence of [...] antineutrinos*[1]. The fact that the lepton number is not a symmetry of Nature would shed light on the Universe unsolved mystery of the matter-antimatter asym-

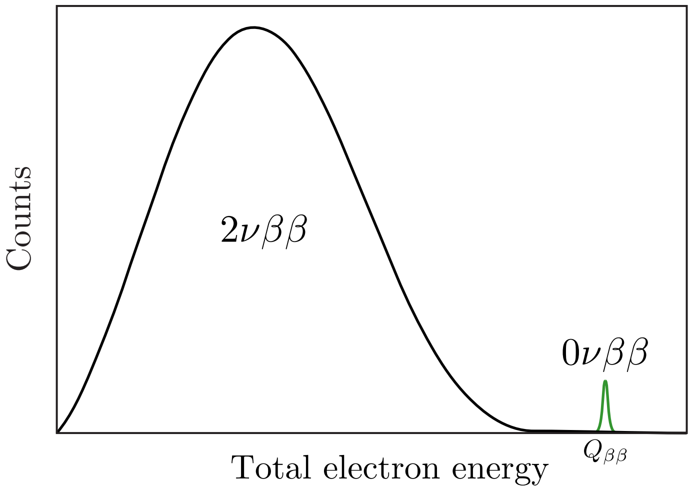

FIG. 1.5: Spectra of the two emitted electrons for $2\nu\beta\beta$ (black line) and for $0\nu\beta\beta$ (green line), not to scale. The gaussian shape of the $0\nu\beta\beta$ peak is due to the detector response.

metry. Indeed, a lepton number violating process could have generated a large number of leptons in the early Universe (*leptogenesis*). Through processes conserving B-L, where B is the baryon number and L is the lepton number, these leptons might be the responsible for the *baryogenesis*, the baryon asymmetry due to which the known Universe exists. This theory is named *baryogenesis via leptogenesis* and it is currently the most credited one. Detailed discussions on this topic can be found in [20][21].

Mechanisms for $0\nu\beta\beta$ decay are expected also in the framework of many extended models[22][23][24], however the hypothesis that it takes place through the exchange of a light Majorana neutrino is the most favored[25], and is the one that will be considered in this work. A schematic representation of this process is shown in figure 1.4-(b).

The $0\nu\beta\beta$ decay rate $\Gamma^{0\nu}$ is then proportional to the *effective Majorana mass* $m_{\beta\beta}$:

$$\Gamma^{0\nu} = G^{0\nu}|M^{0\nu}|^2 \frac{\langle m_{\beta\beta}\rangle^2}{m_e^2} \tag{1.19}$$

where $G^{0\nu}$ is the decay phase space taking into account the final state, $M^{0\nu}$ is the Nuclear Matrix Element (NME), m_e is the mass of the electron, that is conventionally taken as normalization factor[26], and $m_{\beta\beta}$ is nothing else than a combination of the mass m induced on left-handed neutrinos in eq. 1.14 weighted on the mixing matrix parameters:

$$m_{\beta\beta} = \left| \, e^{i\eta_1}|U_{e1}^2|m_1 + e^{i\eta_2}|U_{e2}^2|m_2 + |U_{e3}^2|m_3 \, \right| \tag{1.20}$$

In this expression, $\eta_{1,2}$ are the Majorana phases, $m_{1,2,3}$ are the masses associated to the respective neutrino mass eigenstates and $U_{e1,2,3}$ are the elements of the PMNS mixing matrix defined in eq. 1.2. The decay rate is related to the half-life of the process through $T_{1/2} = \ln 2/\Gamma^{0\nu}$, thus setting limits on $T_{1/2}^{0\nu}$ allows to obtain limits on $m_{\beta\beta}$. The phase space factor $G^{0\nu}$ has been computed very precisely in recent works[27], resulting in an uncertainty around 7%. The calculation of the NME $M^{0\nu}$ is instead much more compli-

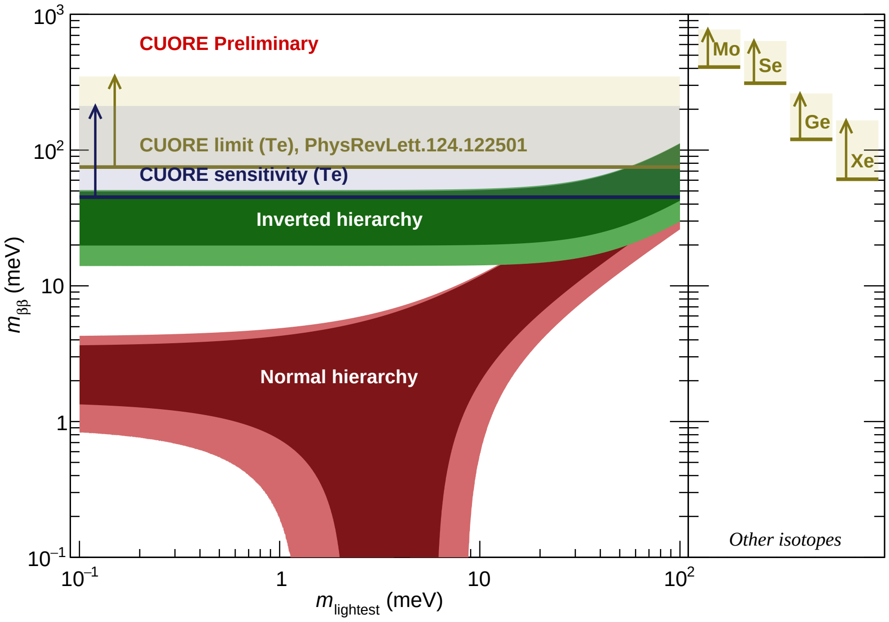

FIG. 1.6: Effective Majorana mass $m_{\beta\beta}$ as a function of the lightest neutrino mass $m_{lightest}$. The green and the red regions indicate the possible values of $m_{\beta\beta}$ and $m_{lightest}$ in case of IH and NH, respectively. The shaded areas represent the uncertainties on the oscillation parameters measurements.

cated. This contains the information on the nuclear structure and becomes more complex as the mass number increases. As previously mentioned in this section, the double beta decay mostly involves heavy nuclei, thus the determination of NME is too complicated to be analytically computed and only numerical calculations can be performed. To this purpose, several models using different approximations exist[28]. The most common ones are the Quasiparticle Random Phase Approximation (QRPA)[29][30][31], the Interacting Shell Model (ISM)[32][33] and the Interacting Boson Model (IBM2)[34]. A disagreement of a factor 2 to 3 is currently present among calculations obtained with different models; this represents the major source of uncertainty on the evaluation of $m_{\beta\beta}$.

Another crucial outcome of the observation of $0\nu\beta\beta$ decay is that it would constrain the neutrino absolute mass scale and it might clarify on the mass hierarchy issue. The definition of the Majorana mass in eq. 1.20 shows a dependence on the oscillations parameters, indeed their measurements allow to put constrains on $m_{\beta\beta}$. The effective Majorana mass depends now on only 3 unknowns, namely the lightest neutrino mass $m_{lightest}$ and the two Majorana phases $\eta_{1,2}$: $m_{\beta\beta}$ is usually represented as a function of $m_{lightest}$, where the dependence on $\eta_{1,2}$ is expressed by two regions for the Normal or Inverted Hierarchy (fig. 1.6). The Quasi-Degenerate case is represented by the area where these overlap. The band structure is due the fact that an observation of the $0\nu\beta\beta$ decay would access to an interval of values for $m_{\beta\beta}$, because of the uncertainties on the NME calculation and on the Majorana phases, that are left free to vary between $[0,2\pi]$. If $m_{\beta\beta}$ were measured to be in the Quasi-Degenerate region, there would be no distinction between NH and IH; however, cosmological constrains coming from the study of the three neutrino masses sum partially exclude this scenario, and slightly favour the NH with respect to the IH[35][36]. Currently no observations were claimed, and more and more stringent lower limits on the half-life of this decay are set. This corresponds to put upper limits on $m_{\beta\beta}$, excluding the regions of plot 1.6 going towards lower and lower masses.

1.5 Experimental search of $0\nu\beta\beta$ decay

The observable measured by experiments searching for $0\nu\beta\beta$ decay is the half-life $T^{0\nu}_{1/2}$. In case the expected signature is detected, the relation between the half-life and the number of signal events N_S measured in the time interval Δt can be obtained. The number of nuclear disintegrations occurred in Δt is expressed as:

$$N_S = -\frac{dN(t)}{dt}\Delta t \tag{1.21}$$

where $N(t) = N_{nuclei}e^{-\frac{t}{\tau}}$ is the well known decay law, being N_{nuclei} the number of available $\beta\beta$ emitting nuclei at time t=0. N_{nuclei} is calculated taking into account the molar mass A of the detector, its total mass M and the isotopic abundance η:

$$N_{nuclei} = \frac{N_a}{A}\,M\,\eta \tag{1.22}$$

where N_a is the Avogadro number. Assuming that the experimental time scale is much shorter than the lifetime of the process ($t \ll \tau$) and reminding that $\tau = T_{1/2}/\ln 2$, the relation between $T_{1/2}$ and N_S is obtained from eq. 1.21 and 1.22:

$$T^{0\nu}_{1/2} = \ln 2\,\epsilon\,\eta\,\frac{N_a}{A}\frac{M\Delta t}{N_S} \tag{1.23}$$

In this expression, the detection efficiency ϵ is also included. The product between the detector mass and the live time $M\Delta t$ is referred to as the *exposure* of the experiment. The expected number of background counts N_B within a energy window ΔE is, in case of a rate independent of energy:

$$N_B = b\,M\Delta t\Delta E \tag{1.24}$$

where b is the background index in units of counts/keV/kg/y in the Region Of Interest (ROI), namely an energy region around $Q_{\beta\beta}$, and ΔE is usually taken as the detector energy resolution at $Q_{\beta\beta}$. As the counts obey the Poissonian statistics, the $0\nu\beta\beta$ signature can be observed if the number of signal events is larger than the background fluctuations, namely if the condition $N_S \geq \sqrt{N_B}$ is satisfied.

If, on the contrary, no experimental evidence of the $0\nu\beta\beta$ peak is claimed, only a lower limit on the half life time can be imposed. A similar argument can be used to evaluate a parameter called *sensitivity* $S^{0\nu}$, which expresses the potential of the experiment to the searched phenomenon. The sensitivity is defined as the half-life corresponding to the minimum number of observable signals above the background at a given statistical significance n_σ:

$$S^{0\nu}(n_\sigma) = \frac{\ln 2}{n_\sigma}\,\epsilon\,\eta\,\frac{N_a}{A}\sqrt{\frac{M\,\Delta t}{b\,\Delta E}} \tag{1.25}$$

From this expression, the parameters that require to be optimized in order to realize a competitive $0\nu\beta\beta$ experiment are clearly shown. Before discussing the experimental choices related to this purpose, it is important to point out that the sensitivity expression in 1.25 is valid as long as $N_B \gg 1$, namely in a scenario that is limited by background statistical fluctuations. Indeed, it changes in the so-called *zero-background condition*, that is realized when the background level in the ROI is so low that the number of expected background events in this energy region is of the order of unity ($N_B \leq \mathcal{O}(1)$)[26]. In this situation the detector energy resolution becomes irrelevant and taking into account the background fluctuations makes no sense, thus the sensitivity becomes:

$$S^{0\nu}_{0-bkg} = \frac{\ln 2}{n_\sigma}\,\epsilon\,\eta\frac{N_a}{A}\,M\,\Delta t \tag{1.26}$$

Operating in the zero-background condition is therefore particularly convenient, since the sensitivity to the $0\nu\beta\beta$ decay half-life linearly increases with the experimental exposure, contrarily to the finite background case of eq. 1.25, where it grows with its square root. For these reasons, efforts are put by future experiments searching for $0\nu\beta\beta$ decay to manage operating in this regime.

The choice of the experimental parameters to maximize the sensitivity is crucial to realize a competitive $0\nu\beta\beta$ experiment, that should take care of the following characteristics:

- *$Q_{\beta\beta}$ of the emitter nucleus.* Isotopes with a Q-value higher than the 2615 keV γ peak from ^{208}Tl are preferred, as the natural γ radioactive contribution to the spectrum is significantly reduced beyond this line. Hence, an appropriate choice of the isotope is important to deal with a low background region of the spectrum. In addition, a high value of $Q_{\beta\beta}$ corresponds to a higher decay probability, since the phase space factor $G^{0\nu}$ is proportional to Q^5.

- *Natural isotopic abundance.* The sensitivity linearly increases with the isotopic abundance. A natural high value of this parameter means a large number of $\beta\beta$ emitting nuclei, and possibly allows to avoid economically expensive enrichment procedures that may also introduce radioactive contamination. ^{128}Te and ^{130}Te represent the two elements with higher natural isotopic abundances, 34.167% and 31.753% respectively[37]. Apart from these two exceptions, the majority of $0\nu\beta\beta$ candidates have natural abundances below 10%, thus isotopic enrichment is necessary to get an adequate number of active nuclei.

- *Background level.* This is the most critical aspect for a $0\nu\beta\beta$ experiment operating in the non-zero background regime. As previously shown, the sensitivity can have a square root or a linear dependence on the exposure depending on the background level: thus, a big effort should be put to suppress the numerous sources of background, with the aim of approaching and maintaining the zero-background ideal condition as long as possible. A background level of the order of 10^{-5} to 10^{-4} counts/keV/kg/y allows a ton-scale experiment with a few keV FWHM energy resolution to keep the zero-background condition likely for the entire time of its operation, which is typically less than 10 years. Working in underground location is a crucial requirement to protect the detector from the cosmic rays and the cosmogenic activation of the materials; an accurate choice of such materials in terms of radiopurity is essential, as well as the strict protocols that should be adopted for their transportation, cleaning and assembling procedures. Appropriate active and/or passive shieldings should also be employed to protect the detector from any external source of radioactivity, and other background rejection strategies such the use of active vetoes should be used. Further discussion on this will follow in the next section.

- *Energy resolution.* As just discussed for the background level, a few keV energy resolution is a crucial requirement to achieve the zero-background condition, as a broad $Q_{\beta\beta}$ peak means a larger region where background counts can be introduced. The most significant example regards the $2\nu\beta\beta$ decay contribution to the ROI: the energy resolution has the effect of broadening the tail of this spectrum, thus its events are smeared into the ROI representing a crucial and irreducible background source for $0\nu\beta\beta$ decay. The only possibility to mitigate this effect is to better disentangle it from the $0\nu\beta\beta$ peak by means of an excellent energy resolution.
  Once the zero-background condition is satisfied, the sensitivity does not depend on the resolution anymore. On the contrary, in case of background-dominated experiments, the sensitivity explicitly depends on the square root of this parameter.

- *Detection efficiency.* Maximizing the probability that a $\beta\beta$ event is fully contained in the detector is essential. To this purpose, experimental approaches where the emitter isotope is embedded into the detector revealed to be particularly convenient, providing detection efficiency levels beyond 90%. This aspect will be further discussed in the next section.

- *Detector mass.* A large exposure is another requirement to achieve a competitive sensitivity. To this purpose, increasing the detector mass, thus increasing the number of $\beta\beta$ emitting nuclei is crucial, as the experimental live time generally lasts few years. Current generation experiments aim at operating with ton-scale detector masses, and for this reason it is important that the chosen experimental technique and the detector design are suitable for mass scalability.

Unfortunately, an optimal choice simultaneously satisfying all these requirements does not exist, and compromise solutions have to be adopted. In figure 1.7, a comparison among the Q-values and natural isotopic abundances η of the most commonly studied isotopes is

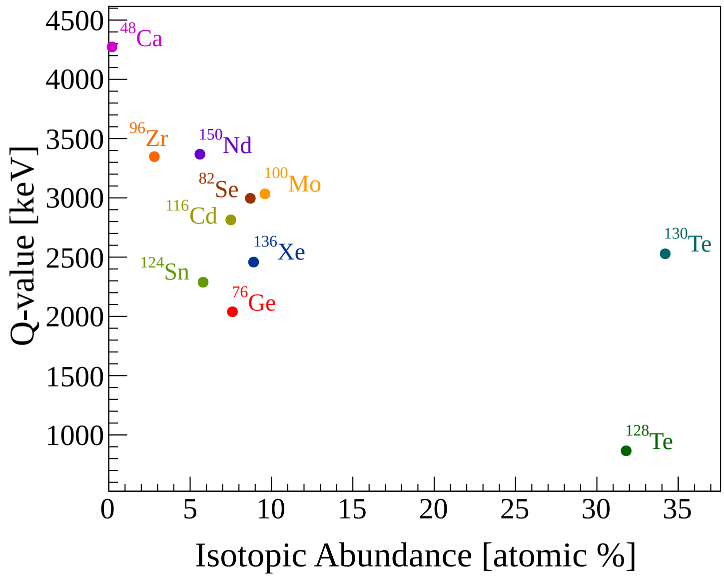

FIG. 1.7: Comparison of the Q-values and natural isotopic abundances among the most commonly studied $0\nu\beta\beta$ decay isotope.

shown, while in table 1.8 some of the most recent limits on the $0\nu\beta\beta$ decay half-lives are listed for different isotopes.

1.5.1 Overview on experimental techniques

The experimental signatures from $0\nu\beta\beta$ decay are well defined: the summed energy of the two emitted electrons is expected to produce a sharp peak at $Q_{\beta\beta}$. However, this process is predicted to be extremely rare, with an half-life larger than 10^{26} years, thus the detection of the $Q_{\beta\beta}$ peak gets difficult as several background sources contribute to deposit energy in the same region. A large international effort is dedicated to the search of this process, and several experimental techniques are used. Two main approaches can be distinguished: the

$\beta\beta$ Decay Reaction	$T^{0\nu}_{1/2}$ limit [y]
$^{48}Ca\rightarrow^{48}Ti$	$> 6.2 \cdot 10^{22}$ [38]
$^{76}Ge\rightarrow^{76}Se$	$> 1.8 \cdot 10^{26}$ [39]
$^{82}Se\rightarrow^{82}Kr$	$> 3.5 \cdot 10^{24}$ [40]
$^{96}Zr\rightarrow^{96}Mo$	$> 1.29 \cdot 10^{22}$ [41]
$^{100}Mo\rightarrow^{100}Ru$	$> 1.5 \cdot 10^{24}$ [42]
$^{116}Cd\rightarrow^{116}Sn$	$> 1.9 \cdot 10^{23}$ [43]
$^{128}Te\rightarrow^{128}Xe$	$> 1.1 \cdot 10^{23}$ [44]
$^{130}Te\rightarrow^{130}Xe$	$> 3.2 \cdot 10^{25}$ [45]
$^{136}Xe\rightarrow^{136}Ba$	$> 1.07 \cdot 10^{26}$ [46]

TABLE 1.8: List of the current lower limits on the $0\nu\beta\beta$ decay half lives of different isotopes.

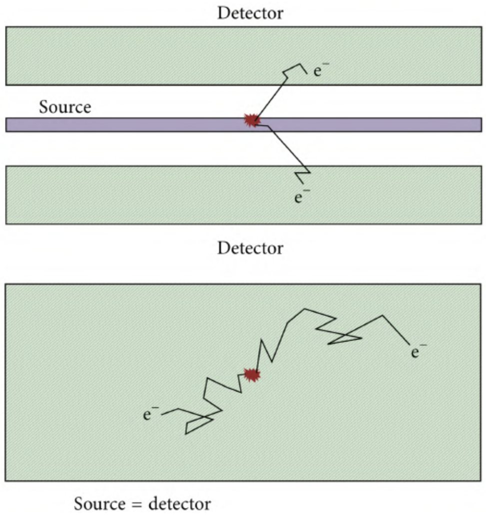

FIG. 1.9: Sketch of the external source technique (top) and the calorimetric technique (bottom), employed for the experimental search of $0\nu\beta\beta$ decay. Taken from [25].

calorimetric technique and the *external source technique* (fig. 1.9)[25]. The calorimetric technique is based on the fact that the $\beta\beta$ emitting isotope is embedded in the detector material. This method has the advantage of gathering an intrinsic efficiency $> 90\%$, thus hundred to ton scale detector masses can be achieved. In addition, this approach allows to reach a few keV energy resolution, and this helps in distinguishing the $0\nu\beta\beta$ peak from the $2\nu\beta\beta$ spectrum tail. On the other hand, the event topology information is usually not available. On the contrary, the external source approach exploits the information from particle tracking, hence providing a precise reconstruction of the event topology. This aspect is crucial for an effective background identification and rejection to achieve the zero-background condition. However, this technique provides poor performances in terms of a $\sim 30\%$ detection efficiency and a $\sim 10\%$ energy resolution, hence it is not possible to distinguish between electron pairs emitted by $0\nu\beta\beta$ or $2\nu\beta\beta$ decay.

To date, the most stringent limits on the $0\nu\beta\beta$ decay half-lives have been obtained with the calorimetric technique, that is the one used by CUORE. However, an effective strategy for background reduction consists of combining different experimental techniques, as operating a detector that embeds the $\beta\beta$ emitter and employing other materials such as scintillators as active vetoes for background events. The GERDA experiment, for example, uses this approach for the search of $0\nu\beta\beta$ decay in ^{76}Ge[47]: the Ge-diode detectors enriched in the studied isotope provide an excellent energy resolution of 3-4 keV and are immersed in a tank of liquid Argon instrumented with SiPMs and PMTs. This keeps the diodes at cryogenic temperature and is exploited as active scintillating veto. A water tank instrumented with PMTs surrounds the experiment, acting as muon veto. Events in coincidence with scintillation light can thus be identified as background and rejected, and thanks to this discrimination GERDA was successfully operated in zero-background condition for the entire design exposure. The KamLAND-ZEN experiment is instead currently searching for $0\nu\beta\beta$ decay of ^{136}Xe with a liquid scintillator loaded with Xe. This is contained in a balloon surrounded by another liquid scintillator instrumented with PMTs, which scintillation light allows the background discrimination and rejection. A different technique will be used by the NEXT project, which will search for $0\nu\beta\beta$ decay of ^{136}Xe with a high-pressure xenon gas time projection chamber with electroluminescent (HPXe-EL) amplification[48]. This method will provide a less than 1% energy resolution at the $Q_{\beta\beta}$ and will take advantage of the charged particles tracking as a background rejection strategy. In addition, the HPXe-EL technology may allow to detect the presence of the Ba++ ion emitted in ^{136}Xe $0\nu\beta\beta$ decay, providing a determining contribution towards the background-free condition. One last example that it is worth to mention is the method that will be employed by the CUPID project. CUPID is a next generation experiment that is willing to search for $0\nu\beta\beta$ decay of ^{100}Mo with scintillating bolometers combined with light detectors, that will allow to perform particle identification to discriminate and reject background the events.

Chapter 2

The CUORE Experiment

The CUORE experiment, namely the "Cryogenic Underground Observatory for Rare Events", is a 1 ton-scale array of cryogenic bolometers aimed at the search of neutrinoless double beta decay in ^{130}Te. Its detector is comprised of 988 TeO_2 crystals, operated at a base temperature of ∼10 mK. With a TeO_2 total mass of 742 kg, corresponding to 206 kg of ^{130}Te, CUORE is currently the largest experimental setup of its kind for the $0\nu\beta\beta$ decay search.

CUORE is located in Hall A at the Laboratori Nazionali del Gran Sasso (LNGS) of INFN in Assergi (AQ), Italy. The LNGS were built inside the Gran Sasso Mountain, at an average depth of 3650 m water equivalent (fig. 2.1). This rock coverage allows to suppress the muon and neutron fluxes at a value of $3 \cdot 10^{-8}\,\mathrm{cm}^{-2}\mathrm{s}^{-1}$[49] and $4 \cdot 10^{-6}\,\mathrm{cm}^{-2}\mathrm{s}^{-1}$[50], respectively. For this reason, this environment is particulaly favorable for a rare events experiment like CUORE.

CUORE is currently taking data since January 2017. Its goal after 5 years live time is a sensitivity of $S_{0\nu} \sim 9 \cdot 10^{25}$ y (90% C.L.) [51], which corresponds to an upper limit range for the Majorana neutrino mass of 50-130 meV. CUORE has been realized aiming at a background index of 10^{-2} counts/(keV · kg · y) and an energy resolution of 5 keV FWHM in the Region Of Interest (ROI).

2.1 CUORE predecessors

The first proposal of the bolometric technique (section 2.2) for the search of rare events dates back to 1984, when E. Fiorini and T.O. Niinikoski explored the capability of low temperature calorimetry to overcome the limitations of the experiments of that time searching for rare processes such as $0\nu\beta\beta$ decay [52]. Starting from 1991, a group of few researchers led by E. Fiorini pioneered the use of TeO_2 bolometers as thermal detectors. The first measurements were performed on small mass crystals of 6 g to 73 g ([53],[54],[55]): the promising results obtained in terms of the achievable energy resolution and low background level raised the interest in the development of this technique. The large effort made in this direction and in increasing the detector mass brought Fiorini, in 1997, to propose the re-

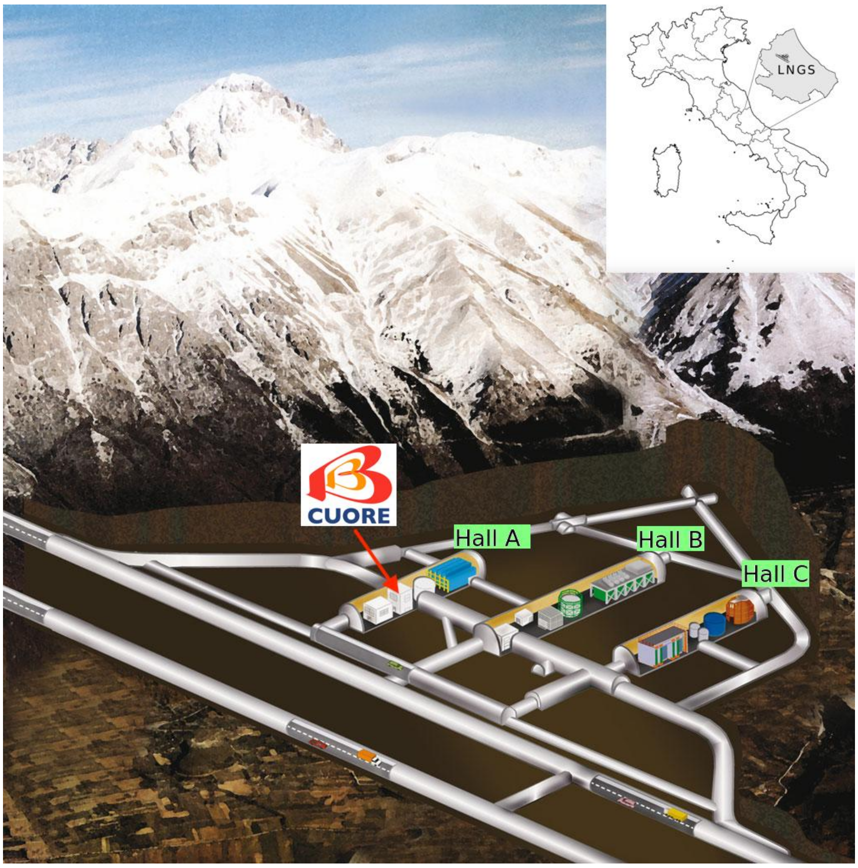

FIG. 2.1: A scheme of the Laboartori Nazionali del Gran Sasso, in the center of Italy.

alization of CUORE [56]. Before its installation at LNGS, two smaller-scale predecessors, Cuoricino (2003-2008) and CUORE-0 (2013-2015), demonstrated the efficiency of the TeO_2 bolometers for the $0\nu\beta\beta$ decay search at the mass scale of a few tens of kg. Figure 2.2 shows the significant evolution of experiments using this technique over the last decades.

2.1.1 CUORICINO

Cuoricino is the italian for "small CUORE". This experiment operated for 5 years at LNGS, from 2003 to 2008. The detector was an array of 44 $(5 \times 5 \times 5)\,\mathrm{cm}^3$ plus 18 $(6\times3\times3)\,\mathrm{cm}^3$ TeO_2 crystals, including natural and enriched ones (82% in ^{130}Te and 75% in ^{128}Te), arranged in a single tower. Cuoricino had an active TeO_2 mass of 40.7 kg with $\sim$11 kg of ^{130}Te, and collected a total exposure of 19.75 kg·y TeO_2 during the entire period of its data taking. The best performance in terms of achieved energy resolution and background index (BI) was obtained by the 5 cm sided crystals, that showed an average FWHM of (5.8 ± 2.1) keV at the 2615 keV ^{208}Tl line and a BI of (0.153 ± 0.006) counts/(keV·kg·y) in the region of interest. As a matter of fact, 5 cm sided crystals were used to realize the forthcoming CUORE-0 and CUORE. Cuoricino provided a lower limit on ^{130}Te $0\nu\beta\beta$ decay half life at 90% C.L. of $T^{0\nu}_{1/2} > 2.8 \cdot 10^{24}$ y, which was the best limit at the time [57] [26]. One of the most important outcome of this experiment in view of the realization of

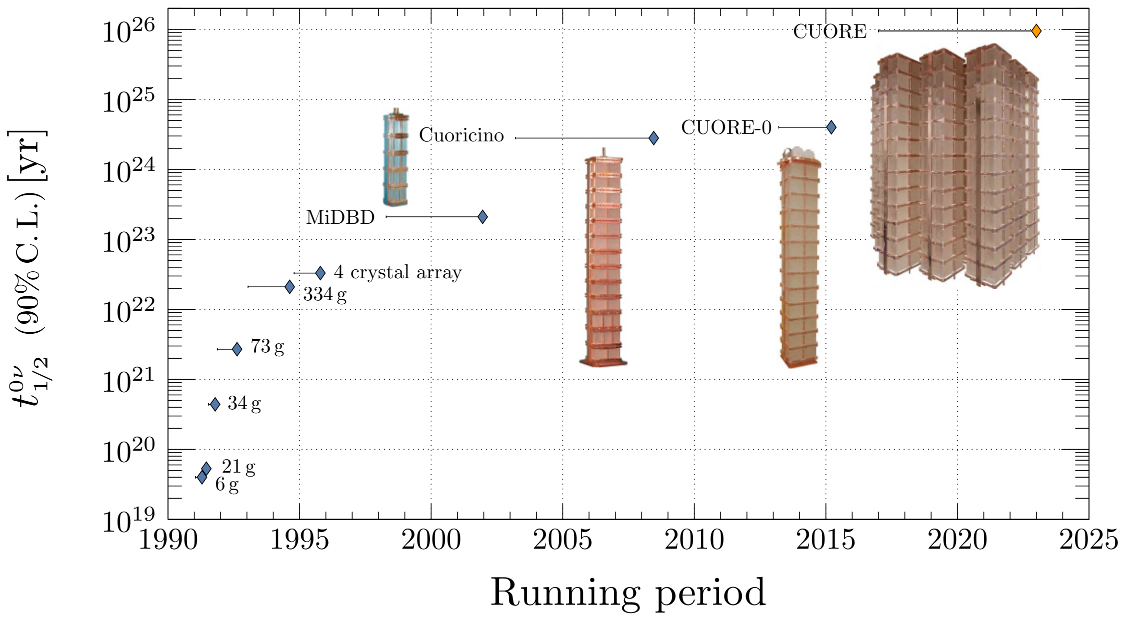

FIG. 2.2: Upgrades and sensitivity evolution of TeO_2 detectors experiments, from the first small mass prototypes to CUORE.

the future CUORE-0 and CUORE was the study of the background sources. In particular, Cuoricino revealed that the primary background contribution to the ROI counts was due to the degraded alpha particles coming from the surface radioactive contamination of the detector and the cryostat copper. Thanks to this results, new specific accurate protocols were adopted in CUORE-0 and CUORE for the cleaning procedure of the crystals, their supporting structure and the cryostat materials, as well as during the assembly phase.

2.1.2 CUORE-0

The CUORE-0 experiment ran from 2013 to 2015, and it was the last stage before the CUORE full scale realization. The CUORE-0 detector consisted of 52 natural 5 cm sided TeO_2 crystals for a total active mass of ~39 kg, arranged in a single tower structured just as one of those projected for CUORE. The detector array was hosted by the same cryostat employed for Cuoricino at LNGS. The main purpose of CUORE-0 was to test the new authomatized techniques employed for the assembly procedure and to validate the effectiveness of the new protocols for the cleaning operations and materials selection. Such accurate procedures had the positive effect of reducing the background rate in the alpha continuum region by a factor of ~7, passing from (0.110 ± 0.001) counts/(keV·kg·y) in Cuoricino to (0.019 ± 0.002) counts/(keV·kg·y) in CUORE-0 [58]. A significant background rate mitigation was also obtained over the whole energy range, in particular a factor ~3 was gained in the ROI, where the Cuoricino rate was measured to be (0.169 ± 0.006) counts/(keV·kg·y), while it was $(0.058 \pm 0.004(\text{stat.}) \pm 0.002(\text{syst.}))$ counts/(keV· kg· y) in CUORE-0 [57]. An improvement with respect to its predecessor was also obtained in the energy resolution, with an exposure weighted FWHM of (4.9 ± 2.1) keV at $Q_{\beta\beta}$.

During its operational period, CUORE-0 collected data for a total TeO_2 exposure of 35.2 kg·y corresponding to 9.8 kg·y of ^{130}Te, and a lower limit on ^{130}Te $0\nu\beta\beta$ decay half life of $T_{1/2} > 2.7 \cdot 10^{24}$ y at 90% C.I. was set. Combining this result with the previous of Cuoricino, a new most stringent limit of $T_{1/2} > 4.0 \cdot 10^{24}$ y at 90% C.I. was obtained [59].

2.2 The bolometric tecnhique

A bolometer is a solid state detector working as a pure calorimeter. In a simplified sketch, it is a device consisting of an absorber linked to a thermal sensor, and connected to a heat bath through a weak thermal link (fig. 2.3). When a particle interacts with the absorber material, the deposited energy is converted into phonons, and the temperature variation experienced by the absorber is measured by the thermal sensor. As it will be shown later in this paragraph, the amplitudes of such thermal variations are extremely small, thus operating the bolometers at cryogenic temperatures is necessary in order to get a measurable signal.

Bolometers are very sensitive to temperature drifts, since these can affect their thermal capacity and modify their response to the same amount of deposited energy. Keeping a stable detector response over time is a crucial aspect for any experiment: an effective solution to this purpose is to include an additional component periodically injecting a fixed amount of energy to the system. In CUORE, each crystal was equipped with a 2.3×2.4×0.5 mm^3 silicon heater able to fire pulses similar to particle induced events, whose rate and amplitude can be adjusted depending on the experimental needs. This allows to measure the gain of each detector and correct the effects of thermal instabilities during offline analysis, specifically during the *stabilization* sequence, that will be described in the next chapter.

Finally, the thermal connection to the heat bath is needed to maintain the bolometer working temperature.

One of the main advantages of a bolometric detector is its excellent intrinsic energy resolution, which is primarily determined by the thermodynamic energy fluctuations in the absorber due to the heat flow through the connection with the thermal bath [60]. In case of thermal equilibrium, the average number of phonons N in the absorber can be expressed as

$$N = \frac{C(T)}{k_B} \tag{2.1}$$

being C(T) the heat capacity, and k_B the Boltzmann constant. Assuming that the number of exchanged phonons follows the Poisson statistics, and thus $\Delta N = \sqrt{N}$, the energy fluctuation of the detector is proportional to $\sqrt{N}$ times the energy of a single phonon $\epsilon = k_B T$:

$$\Delta E \propto \epsilon\sqrt{N} = \xi\sqrt{C(T)\, k_B T^2} \tag{2.2}$$

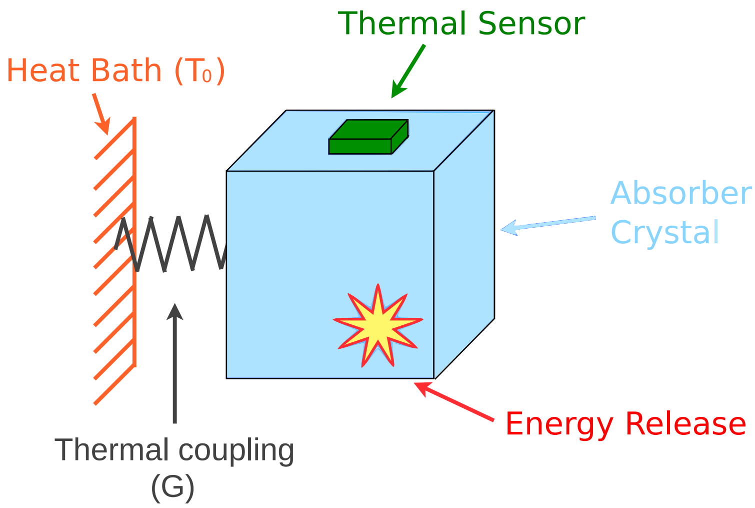

FIG. 2.3: Schematic description of a bolometer, like those used in CUORE.

where ξ is a dimensionless factor taking into account the characteristics of a real detector. From this expression it follows that the energy resolution of a bolometer can be of the order of few eV, provided that the temperature of the system is sufficiently low[26]. As an example, a 750 g TeO_2 bolometer operated at 10 mK, like those used in CUORE, is estimated to have an intrinsic energy resolution of 20-100 eV, despite the measured value is of few keV. Indeed, in real detectors such ideal energy resolution is actually never reached. Noise sources like the cryogenic apparatus, the electronics, the thermal and the Jonson noise represent some of the dominant contributions that can degrade the energy resolution. As a result, the resolution of a typical bolometer is of the order of few keV at 1 MeV, which is however excellent for double beta decay research. On the contrary, one of the main drawbacks of bolometric detectors is their slow response: this limits their application in the field of rare event search, were the expected signal rate is of the order of tens of mHz.

2.2.1 Absorber

In the simplified model described above, the amplitude of the temperature variation ΔT induced by an interacting particle can be expressed as:

$$\Delta T = \frac{\Delta E}{C} \tag{2.3}$$

where ΔE is the deposited energy and C is the heat capacity of the absorber. The released energy is converted into phonon excitations, that propagate at the speed of sound v_s through the absorber lattice and flow to the heat bath via the thermal conductance G, until the thermal equilibrium is eventually restored. The thermalization time τ_{phonon} is given by:

$$\tau_{phonon} \sim \frac{L}{v_s} \tag{2.4}$$

where L is the absorber size. In CUORE, $\tau_{\mathrm{phonon}} \sim 10\,\mu$s, being the crystals 5 cm side cubes and the speed of sound $\mathrm{v_s} \sim 4 \cdot 10^3$ m/s in TeO_2.

Assuming that ΔT is much smaller than the thermal bath temperature T_0, the heat capacity C and the conductance G can be considered constant during the development of a phonon signal. Then the temperature variation can be described as an exponential function of time:

$$\Delta T(t) = \frac{\Delta E}{C} e^{-\frac{t}{\tau}} \text{ , where } \tau = \frac{C}{G}\,. \tag{2.5}$$

From this expression, it is straightforward that a very small heat capacity is required to obtain a larger and measurable signal amplitude. Dielectric and diamagnetic materials, such as TeO_2, are often used to this purpose, as the main contribution to their heat capacity is given by the lattice, and the Debye law can be used to describe their thermal capacity at low temperatures:

$$C(T) = \beta \frac{m}{M} \left(\frac{T}{\Theta_D} \right)^3 \tag{2.6}$$

where $\beta = 1944$ $\mathrm{JK^{-1}mol^{-1}}$, m is the absorber mass, M is the molecular weight and Θ_D is the characteristic Debye temperature of the material. It is now clear that operating bolometric detectors at cryogenic temperatures is necessary to get a small heat capacity and therefore a higher signal amplitude. At room temperature, a thermal variation induced by 1 MeV particle would be of order $10^{-18} - 10^{-15}$ K, and would be impossible to detect; at 10 mK, the CUORE crystals heat capacity has been measured to be $\sim 10^{-9}$ J/K, so the same amount of deposited energy gives a temperature rise of ~ 0.1 mK.

2.2.2 Thermal sensor

Each CUORE crystal is equipped with a Neutron Transmutation Doped semiconductor thermistor (NTD), converting the temperature variations into a voltage signal. A semiconductor thermistor is a thermal sensor whose conductivity strictly depends on the number of available charge carriers. The gap between the valence band and the conduction band of this device is 1.14 eV for silicon and 0.67 eV for germanium, and since $k_B \cdot T \sim 0.025$ eV at room temperature, the number of available charge carriers is too low for the conduction to occur, especially at very low temperatures. An effective method to increase the number of conduction electrons consists of doping the semiconductor, namely introducing a calibrated quantity of impurities into the material in order to create new valence bands closer to the Fermi level. In this way the energy gap between the valence band and the conduction band is reduced, and even small thermal excitations can activate conduction electrons.

The concentration of doping impurities can significantly change the behaviour of a thermistor. If it is below a critical density, the conductivity drops to zero at low temperatures, while above this value the semiconductor starts performing as a metal (Metal-Insulator Transition region)[61]. Thermistors used in low temperature physics are doped below this regime, so that the charge carriers transport among different impurity sites is due to tunneling effect. The energy required for a tunnelling event (this is called *hop*) is provided by absorption or emission of a phonon. This is the Variable Range Hopping (VRH) regime, and the resistance of the thermistor is characterized by a steep dependence of temperature:

$$R(T) = R_0 \, e^{\left(\frac{T_0}{T}\right)^{\lambda}} \tag{2.7}$$

where R_0 depends both on the doping concentration and on the thermistor geometry, and T_0 is only determined by the doping level. The value of the λ parameter depends on the behavior of the density of states near the Fermi level[62]: provided that such density of states does not vanish, λ assumes the value $1/4$ according to the Mott's law. It can be shown that in presence of Coulomb interaction, the density of localized states is reduced close to the Fermi level, and the conduction in VRH regime at sufficiently low temperature is such that λ assumes the value $1/2$. Typical values for CUORE NTDs are $R_0 \sim 0.9{-}1.2\,\Omega$, $T_0 \sim 3-4\,K$ and $\lambda \simeq 0.5$.

The CUORE NTD thermistors (2.4) are ultra-pure germanium wafers doped in the VRH regime through irradiation with a thermal neutron flux[63], which induces nuclear reactions creating impurities of gallium, arsenic and selenium atoms uniformly distributed in the germanium lattice. The arsenic and selenium atoms are created as donor impurities, while the gallium atoms are acceptor impurities: p- and n- dopants concentration levels are similar, thus a compensated germanium semiconductor is obtained. The final doping concentration depends on the exposure time to the neutron flux, hence a very precise knowledge of this parameter is crucial in order to obtain the desired concentration level. Each CUORE NTD is glued to a crystal surface and is biased with a constant current, thus its resistance is measured from the voltage difference at its edges. Golden wires are bonded to the gold pads of each thermistor to connect it to the bias circuit. The signal is

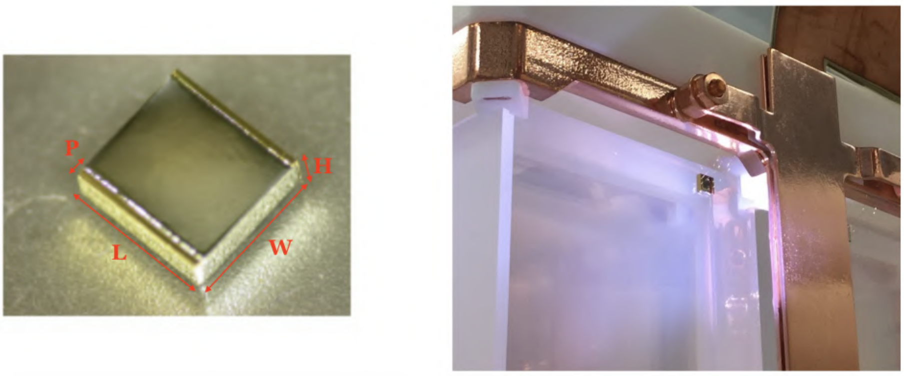

FIG. 2.4: Pictures of a CUORE NTD. Right: typical dimensions are P = 0.2 mm, L = 3.0 mm, W = 2.9 mm, H = 0.9 mm. Left: NTD glued on a CUORE crystal, the golden wires to the biasing circuit are also visible.

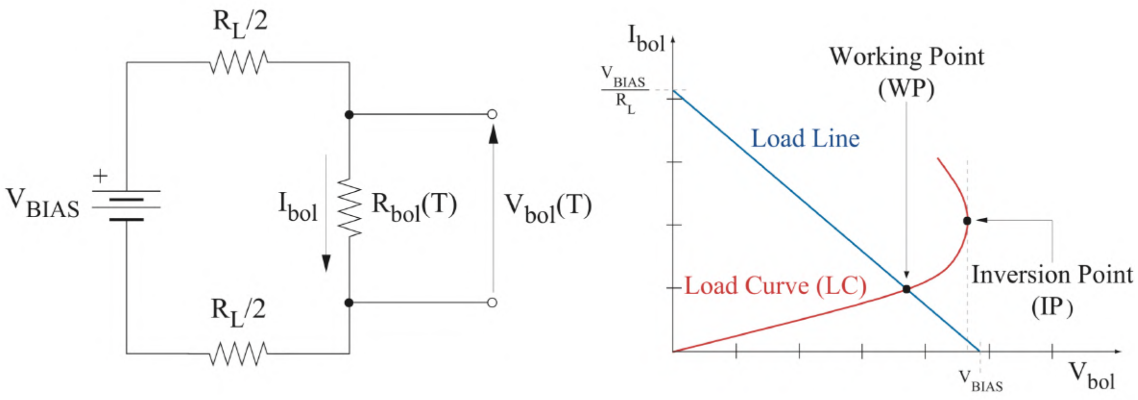

FIG. 2.5: Left: a scheme of the circuit biasing the CUORE NTD thermistors. Right: I_B vs V_{BOL} plot. The load curve, the load line, the inversion point and the working point are shown.

then read out by the front-end boards located at room temperature outside the cryostat.

2.3 Detector operation: load curves and working points

As mentioned in section 2.2.2, in order to measure the NTD resistance variation induced by the energy deposition of a particle in the absorber, the thermistor has to be biased with a constant current. The circuit used in CUORE to bias the NTDs is represented in figure 2.5 - left: a voltage V_{BIAS} is produced by a generator closed on two load resistors $R_{L/2}$ in series with the NTD thermistor, whose resistance is referred to as R_{bol}. If a load resistance much larger than R_{bol} is chosen ($R_L \gg R_{bol}$), then the circuit is biased with an approximately constant current I_{bol} and the voltage at the edges of the thermistor is proportional to its resistance:

$$V_{bol}(T) = I_{bol} \cdot R_{bol}(T) \tag{2.8}$$

The current flowing through the thermal sensor generates a power dissipation given by $P = R_{bol} \cdot I_{bol}^2$, producing Joule heating in the NTD thermistor and thus a decrease in its resistance. This effect is known as *electro-thermal feedback*. The temperature T_{bol} of the NTD is then expressed as:

$$T_{bol} = T_0 + \frac{P}{K} \tag{2.9}$$

where T_0 is the base temperature, and K is the thermal conductance between the NTD sensor and the heat sink. The effect of the electro-thermal feedback on the relation between V_{bol} and I_{bol} is that a non-ohmic behavior is induced. The I_{bol}-V_{bol} curve is called *load* *curve*, and it is represented in figure 2.5 - right. To effectively describe this system, it is now useful to introduce the static resistance R^s_{bol} at each point, as simply the ratio of V_{bol} and I_{bol}, and the dynamic resistance R^d_{bol}, as the inverse of the derivative of the load curve:

$$R^s_{bol} = \frac{V_{bol}}{I_{bol}} \qquad R^d_{bol} = \frac{dV_{bol}}{dI_{bol}} \tag{2.10}$$

From the load curve plot (fig. 2.5 - right), it can be observed that as the current increases, the voltage increases linearly at first, and in this regime R^s_{bol} is constant. Then, V_{bol} starts to deviate from the linear behavior due to the electro-thermal feedback, and the slope of the curve grows until the so-called Inversion Point (IP) is approached, where $R^d_{bol} = 0$. Once the IP is passed, R^d_{bol} becomes negative and the voltage V_{bol} decreases. In static conditions, namely when there are no particle energy depositions in the absorber, the thermal and electric parameters of the NTD are described by a single point along its load curve. This is the *working point* of the thermistor, and it is defined as the intersection between its load curve and the load line of equation $V_{bol} = V_{BIAS} - I_{bol} \cdot R_L$.

A working point must be chosen for each thermal sensor: in general, this means setting its operating voltage V_{bol}. The choice of the NTDs optimal working points is crucial, since this directly affects their response to energy releases into the respective crystal. In CUORE, a dedicated procedure to acquire the NTDs load curves and to evaluate the optimal working points is performed. This consists of a data acquisition in which the amplitude of a pulse at fixed energy is evaluated as different values of the bias current are set. For each bias voltage, the signal-to-noise ratio (SNR) of the pulse is analyzed: the optimal working point is a compromise among a high SNR and a stable response, the latter obtained remaining below the Inversion Point of the load curve.

2.4 The CUORE bolometers

The CUORE detector array consists of 988 cubic TeO_2 crystals of 5 cm side and 750 g weight each. The crystals are arranged in 19 modular structures that are referred to as *towers*. Each tower is made of 52 bolometers organized in 13 floors of 4 crystals. The mechanical support structure is made of a low radioactive copper (NOSV Cu), which is characterized by a high thermal conductivity and is connected to the heath bath: the crystals are thermally and mechanically linked to it through Teflon or PoliTetraFluoroEthilene (PTFE) clamps, that keep the bolometers position on the copper frame and also act as weak thermal coupling (Fig. 2.6).

The CUORE TeO_2 crystals have the advantage of acting both as detectors and as sources of ^{130}Te $0\nu\beta\beta$ decay. Two main reasons led to the choice of this isotope for the CUORE project. The first is its high natural isotopic abundance of 34.167% [37], which allows the realization of crystals with natural Te only, thus avoiding expensive isotopic enrichment procedures that may also introduce radioactive contamination. The other favorable characteristic of ^{130}Te is its Q_{value} of (2527.518 ± 0.013) keV [64] [65] [66], which

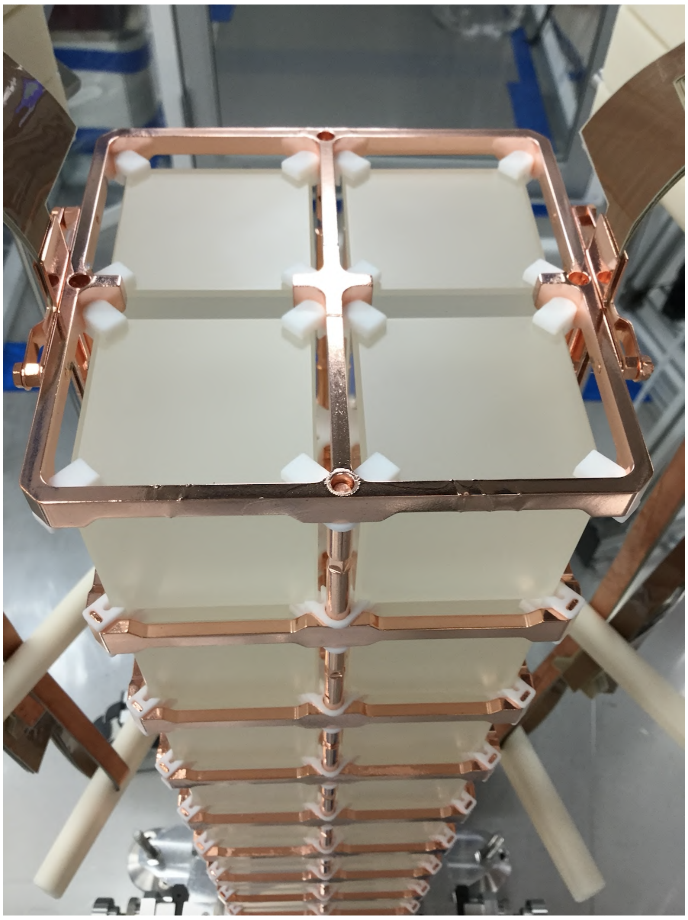

FIG. 2.6: A close view of a CUORE tower. The copper support structure and the PTFE clamps holding the crystal are well visible.

lies into a low natural background window of the energy spectrum, in particular between the most prominent γ line of ^{208}Tl at 2615 keV and its Compton edge.

Tellurium Dioxide (TeO_2) was selected as the most suitable material for the crystals production. It is dielectric and diamagnetic, and its relatively high Debye temperature $T_D = (232 \pm 7)$ K [67] is responsible for a low heat capacity (eq. 2.6), that is crucial to obtain a high signal amplitude and a good energy resolution at cryogenic temperatures, as shown in section 2.2.1. Another advantageous characteristic of TeO_2 is its mechanical behaviour at low temperatures: its thermal expansion coefficient is very close to the one of copper, making such crystals particularly suitable to be held by a copper structure without being excessively stressed during the cooldown [26]. In addition, TeO_2 crystals provide an abundant quantity of double beta decay emitter, being the Tellurium mass about the 80% of the TeO_2 compound. The strict selection of products and procedures adopted for the TeO_2 powder production and the crystal growth provide an excellent level of radiopurity for these bolometers, well below the limits requested for their usage in CUORE [68].

In order to minimize the risk of external contamination of the ultra-radiopure materials accurately selected for CUORE, the towers were assembled and stored in the protected environment of a Clean Room according to the strategy previously validated by CUORE-0

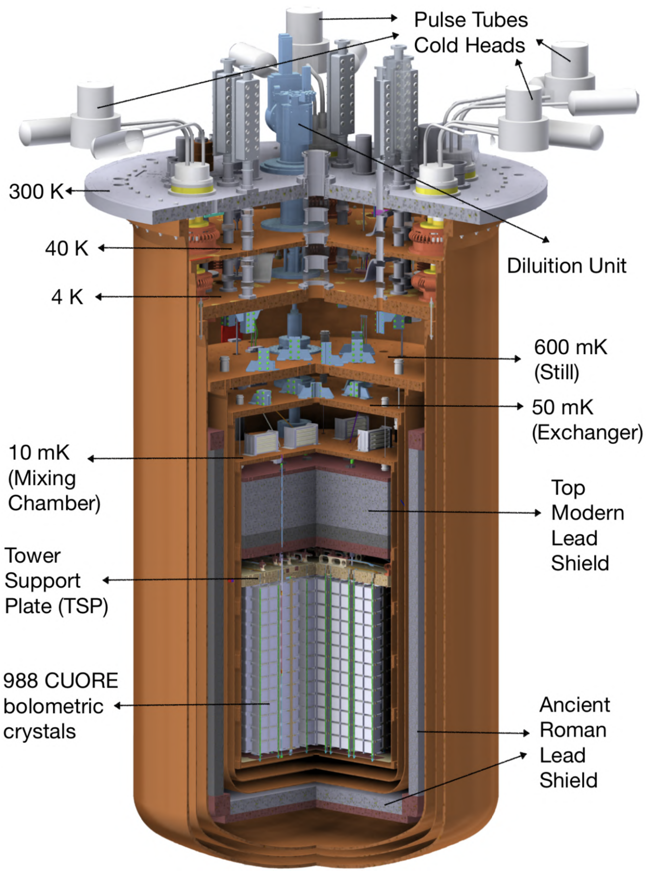

FIG. 2.7: Scheme of the CUORE cryostat, showing the different thermal stages, the lead shieldings, the cooling devices and the detectors.

[69]. In this framework, abatement systems for the radon contamination in air have a crucial role, since its decay products generate critical contributions to the measured background, as it will discussed in chapter 4. To reduce this effect, the assembled towers were kept under nitrogen atmosphere until their installation inside the cryostat, that took place in the same environment. During this phase, the Clean Room was flushed with Rn-free air [70] while the level of radon contamination was constantly monitored, and the people in charge of this operation were not allowed to exit the Clean Room until the installation of a single tower was completed.

2.5 The CUORE cryostat

The CUORE cryostat is hosted at the first floor of the CUORE hut in Hall A at the LNGS underground facility, into one of the Clean Rooms just mentioned. This large cryogen-free dilution cryostat was custom built to house the CUORE bolometers and to reach and maintain their operational temperature of ∼10 mK for years. Such infrastructure was designed with the aim of minimizing the vibrational noise and the environmental radioactivity: these are indeed fundamental conditions for the achievement of the low background level needed to accomplish the CUORE sensitivity goal.

The CUORE cryostat (fig. 2.7) is comprised of 6 coaxial copper vessels thermalized to decreasing temperatures, from the outer at 300 K to the innermost at $\sim$ 10 mK (Mixing Chamber), housing the crystals. Between these two stages, intermediate ones at 40 K, 4 K, 600 mK (Still) and 50 mK (Exchanger) respectively are present. According to the strict radio-purity criteria for the materials choice, these plates and vessels are made of Oxigen-Free Electrolytic copper (OFE) produced by Aurubis, with a purity of 99.99%. The 300 K plate is the only exception, since it is made of stainless steel because of its better performances at room temperature in terms of vacuum tightness and mechanical support. The inner vessel at 10 mK and its plate were realized with a different copper alloy, the Electronic Tough Pitch (ETP1, or NOSV Cu). This material was chosen because of its high thermal conductivity at cryogenic temperatures, and for its low content of hydrogen: the latter property is needed to minimize the dissipation of heat due to the transition of ortho-hydrogen to para-hydrogen, occurring at low temperatures [71] [72].

Two separated vacuum volumes are the main responsible for keeping the detectors thermal insulation: the Outer Vacuum Chamber (OVC) and the Inner Vacuum Chamber (IVC). The OVC is the 5.9 m^3 volume contained in the 300 K vessel till the 4 K plate and is vacuum tight with a minimum pressure lower than 10^{-6} mbar, while the IVC is the volume inside the 4 K vessel, also containing the CUORE towers. The IVC measures 3.4 m^3 and its minimum pressure is less than 10^{-8} mbar [73]. To further strenghten the thermal insulation, the 40 K and 4 K shields are respectively wrapped with one and three coatings of multi-layer aluminized mylar with low thermal conductivity.

The bolometers are protected from the external natural radioactivity and from the cryostat residual contamination by two lead shields, both situated in the IVC. A 5562 kg 6 cm thick lateral and bottom shielding of Ancient Roman lead thermalized to 4 K embraces the cryostat between the 4 K and the 600 mK vessels. There is a very interesting history behind this lead: it was recovered in 1988 from a Roman shipwreck that sank around 80-50 B.C. off the coast of Sardinia, while transporting 120 lead ingots. Thanks to a special agreement between the INFN and the Italian Cultural Heritage Ministry, 30 of these ingots were transferred to LNGS and earmarked for low background experiments [74]. Indeed, this ancient lead spent about 2000 years underwater at a depth of 28 m, so it is depleted in ^{210}Pb, which has an half life of 22.5 years. Moreover, the sea protected it from cosmogenic activation due to cosmic rays. The resulting ultra-low radioactivity level of this lead makes it particularly suitable to be used as shielding for low background experiments like CUORE [75]. Another 30 cm thick shield of 2745 kg made of modern lead is placed just below the 10 mK plate, to protect the CUORE detectors from the radioactivity coming from the top.

2.5.1 The cryostat support and external structure

Mechanical vibrations on the CUORE bolometers can have very critical consequences on the experimental performances. Indeed, these can give rise to undesired heat loads, which can dissipate power to the coldest stages preventing a stable operation at the base temperature; moreover, the propagation of vibrations to the crystals would introduce a

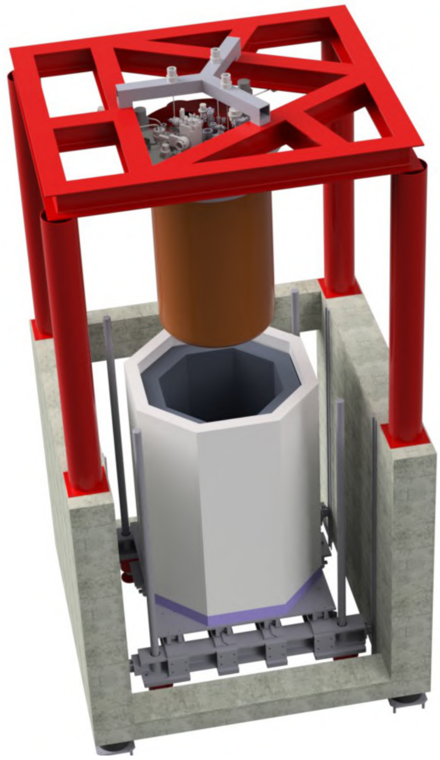

FIG. 2.8: Scheme of the CUORE external support structure.

noise source disrupting the energy resolution of the detectors, with negative consequences on the experimental sensitivity. In addition, LNGS is located in a seismic region of Italy, therefore particular attention must be paid to minimize the effect of earthquakes on the detectors. For all these reasons, a support structure able to suppress the sources of mechanical vibrations is a crucial requirement for CUORE.

The towers holding the crystals are connected to the cryostat through the Tower Support Plate (TSP), located few cm below the top lead shield. This is a multi-stage system that should provide a detector mechanical decoupling: it consists of three stainless steel detector suspension bars (DS), thermalized at each cold stage. The DS mechanically link the TSP to an external structure called *Y-beam*; the parts closer to the crystals were realized with an ultra-pure copper rod, in order to keep the low radioactive background. The Y-beam structure (the grey "Y"-shaped structure on the top of figure 2.8) is positioned at room temperature at the 2nd floor of the CUORE hut, inside a Faraday room hosting the front-end electronics and the external plumbing to operate the cryostat as well. The cryostat is suspended from the Main Support Plate (MSP), the red structure in figure 2.8; to decouple the detectors from the cryostat, the Y-beam is anchored to the MSP by means of three mechanical insulators with the Minus-K technology. This technology consists of arranging a set of elastic constants in a particular configuration, so that the resulting system acts like a soft spring when subjected to small displacements, in spite of the heavy load it supports. This allows to effectively suppress the vibrations propagation from the cryostat to the bolometers, with a cut-off frequency of about 0.5 Hz. The MSP is sustained by four sand-filled columns fixed to a concrete structure at the ground floor of the CUORE hut. This structure is decoupled from the ground thanks to four seismic elastometers, which dissipate the vibrations induced by earthquakes and any activity taking place at the underground LNGS.

As additional protection from environmental natural radioactivity, another 25 cm thick lead shielding surrounds the cryostat at room temperature. To effectively shield neutrons, this is covered by a 20 cm thick polyethilene layer with boric acid panels. The whole structure is situated on a movable platform, so that it can be raised to cover the cryostat during the data taking, while it can be removed if required by hardware activities.

2.5.2 The multistage cooldown

In 2016, the CUORE cryostat managed to cool about 1 ton of material down to ∼7 mK, successfully accomplishing an unprecedented technological challenge and marking a milestone in low temperature experimental physics [73]. The cooldown takes place by exploiting different techniques. The OVC cooling from room temperature to 4 K is performed by means of 4 Pulse Tubes (PTs): the working principle of these dry refrigerators will be described in detail in section 2.5.3. A fifth PT is kept as spare. A custom designed auxiliary sub-system named *Fast Cooling System* (FCS) was employed with the aim of reducing the cooling time: this apparatus uses a closed cycle forcing the circulation of cold ^{4}He gas inside the IVC, and it is able to pre-cool the inner part of the cryostat down to 50 K. When this temperature is reached, the FCS can be switched off and the refrigeration process to 4 K continues with the PTs only. Thanks to this system, the required time to get from room temperature to 4 K is reduced to ∼3 weeks. The cooldown from 4 K to the base temperature of 10 mK is performed through a continuous-cycle ^{3}He/^{4}He Diluition Refrigerator (DR). A detailed description of its operation will be given in section 2.5.4.

2.5.3 Pulse Tube Refrigerators

A Pulse Tube is a cryocooler device whose cooling power is provided by periodic pressure oscillations of ^{4}He gas. A scheme of a PT showing the parts involved in the operational cycle is shown in figure 2.9-left. The pressure waves are generated by a rotary valve that is alternatively connected to the high pressure and low pressure side of a compressor at a frequency of 0.7 revolutions per second, corresponding to a complete cycle at 1.4 Hz. From the rotary valve the Helium gas flows through a regenerator, a porous material with high thermal capacity that absorbs the heat from the gas when it flows from left to right, and stores it for a short time. The regenerator is followed by a thin walled tube (this is the *Pulse Tube*) with heat exchangers at both the ends: the cooling is produced when gas expansions occur into this tube. The helium then flows again in the opposite direction through the regenerator, that releases the stored heat to the gas. Finally, it flows back to the compressor at room temperature, and the cycle can start again.

In CUORE, the five compressors are located at the ground floor of the hut: each PT

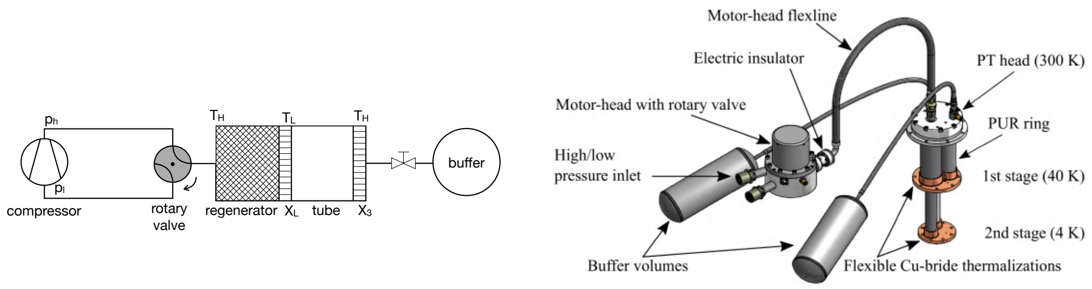

FIG. 2.9: Left: scheme of the internal parts of a PT [76]. Right: rendering figure of a CUORE PT.

is connected to its compressor through a pair of flex lines corresponding to the low and high pressure side. In order to reduce the vibrations generated by the compressors, the flex lines enter a sandbox filled with non-hygroscopic quartz powder and are then driven to the second floor, where the PTs are located. Here, the motor-heads of the PTs housing the rotary valves are visible on the top of the 300 K plate of the cryostat. CUORE uses five custom adapted two-stages pulse tubes PT415-RM by Cryomech, with a cooling power of 1.2 W at 4.2 K and 32 W at 45 K each. A representation of a CUORE pulse tube is shown in figure 2.9-right.

Several advantages are gathered by using these type of cryocoolers: the most important one is that since they do not operate with cryogen liquids, the cryostat does not need periodic refills and thus the duty cycle of the experiment is increased. Another advantage of these dry refrigerators is that they have no moving parts at the low temperature stages: this allows to reduce the vibrations transmitted to the inner part of the cryostat. However, the pressure waves produced by the compressed He flowing through the rotary valve generate a vibrational noise that propagates into the cryostat and reaches the detectors. In CUORE, different passive solutions are adopted to absorb and dissipate these vibrations: mechanical decouplers such as special soft o-rings and a polyurethane ring (PUR) are positioned on the critical parts of the system, all the flex lines and rotating valves are suspended upon the cryostat top plate in a way that any contact with the surrounding system is avoided. Moreover, a considerable reduction of the PT noise was obtained by replacing the Cryomech stepper devices driving the motor of the rotary valves with low-noise stepper devices, which will be referred to as *Linear Drives* (LD)[77]. These are commercial micro-stepping drives allowing to control of the rotary valve position: the rotation of the valve is smoothed dividing the 360° angle into 25600 possible positions, allowing to drive the rotary valve with a precision of 0.014°.

In spite of all these adopted precautions, a non-negligible amount of vibrational noise from the PTs is still injected into the cryostat. In order to further suppress it, a dedicated active noise cancellation technique was developed: in the next section a description of this technique will be given.

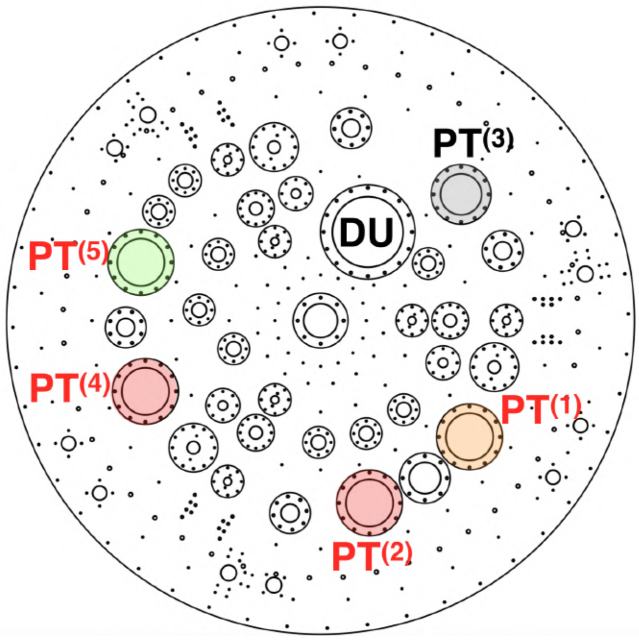

FIG. 2.10: A sketch of the 300 K plate seen from top view. The asymmetric positions of the five pulse tubes in the cryostat are shown. Taken from [77].

The Pulse Tube Phase Scan

As previously mentioned in section 2.5.3, the use of pulse tubes brings several advantages with respect of having a liquid He bath, but has also the downside that the gas pulsation and the valve rotation introduce mechanical vibrations at 1.4 Hz and related harmonics inside the experimental apparatus. This effect is significant in CUORE, since the combination of several PTs simultaneously operating at the same 1.4 Hz frequency can disrupt the detector performance.

An active noise cancellation technique is carried out in order to reduce such downside effect [77][78][1]. The relative phases of the 4 active PTs are evaluated by computing the phase shifts of three of them with respect to the fourth one, taken as reference. The detector noise level shows a dependence on the PT relative phases: the noise reduction technique consists of controlling them in order to find a configuration of the phase differences that gives rise to a destructive interference of the PTs pulsations thus minimizing their noise contribution. A dedicated stabilization algorithm is then capable to maintain the identified minimum configuration, therefore the noise level is kept stable in time. The CUORE system is complex and asymmetric (fig. 2.10), hence the optimal configuration can be obtained only empirically, by scanning a large number of possible phase configurations. In CUORE, this procedure is called *Pulse Tubes phases scan* (PT scan), and dedicated data acquisitions are periodically carried out.

When a PT scan has to be performed, the relative phases are manually set to an initial

[1]Parts of this paragraph are based on ref.[78] (Dompè V. et al., "The CUORE Pulse Tubes Noise Cancellation Technique").

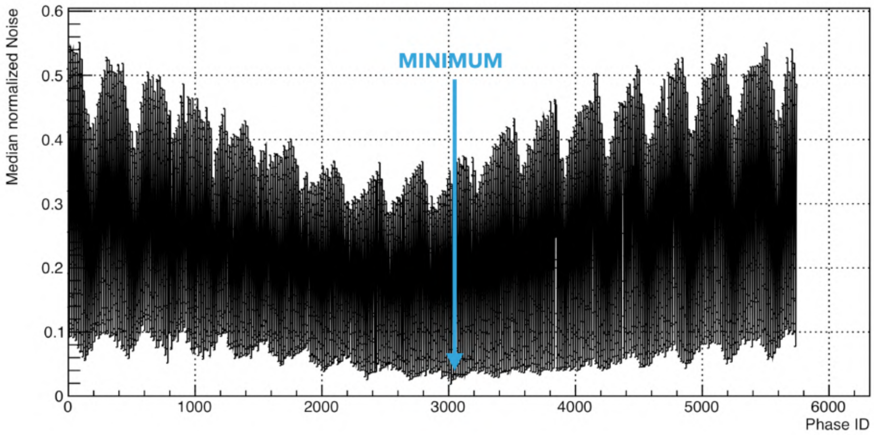

FIG. 2.11: Median normalized noise distribution as a function of the phase configurations: the minimum corresponds to the configuration the maximizes the noise cancellation for the whole CUORE detector [78].

configuration, and the final one is also indicated. A dedicated software controlling the LDs starts driving the phases to the next configuration, until the final one is reached after all the intermediate configurations have been explored with a selected discretization level (*step*). Each phase configuration is kept in order to acquire 4-5 noise waveforms, each one 10 s long.

The acquired data are analyzed in order to determine the configuration that minimizes the whole detector noise. The contribution of the first 10 harmonics of 1.4 Hz to the noise power spectrum (NPS) of each bolometer is then evaluated: this is done by summing over the 10 NPS harmonics amplitudes and weighting each frequency by the corresponding value of the signal power spectrum in frequency domain for each single detector. More than 90% of the signal power in CUORE is due to frequencies below 3 Hz: weighting for the signal power spectrum allows to optimize the algorithm in such a way that the 1.4 Hz and 2.8 Hz harmonics are strongly suppressed with respect to higher noise harmonics. A normalization procedure is then applied to the PT noise contribution, with the aim of comparing all the bolometers regardless of their absolute noise, the latter being defined as the noise distribution mediated over all the phase configurations. Finally, the median over all the bolometers is performed in order to extract the typical normalized response to a certain configuration for the whole detector (fig. 2.11): the minimum of the obtained distribution represents the minimum noise configuration.

Before accepting this as the optimal configuration of the PT relative phases, an additional aspect should be considered. The PT vibrations do not have the same effect on all the CUORE bolometers, since this depends on several aspects, e.g. on their position with respect to the PTs. Usually, the majority of the phase configurations minimize the noise only for a fraction of the of bolometers, and this would result in a non-optimal configuration for the overall detector. In order not to be biased by bolometers that are weakly affected by the PT vibrations, it is important to select which ones should be included in

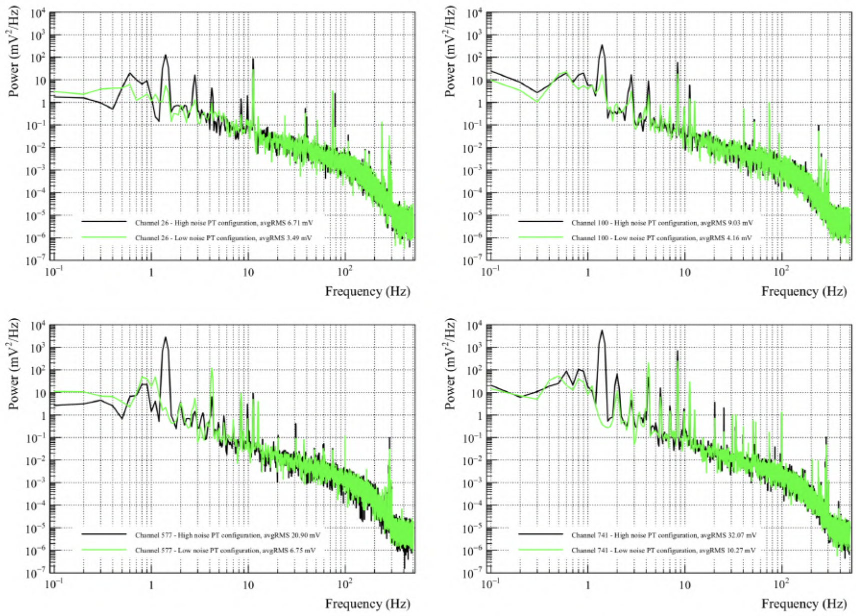

FIG. 2.12: Average NPS of few CUORE single detectors at a high (black line) and a low (green line) noise PT phase configuration. In the two top plots, the low-noise configuration minimizes the overall detector noise, while in the bottom plots a configuration optimizing the single detector noise is represented [78].

the optimization process: to this purpose, the number of detectors with low noise level is evaluated for each phase configuration. The minimum noise configuration that should be chosen is a compromise between the one that optimizes the noise for the largest possible amount of detectors, and the one with lowest possible noise level.

Figure 2.12 shows the NPS of few CUORE bolometers before and after a low noise configuration of the PT phases is set. In CUORE, a complete phase scan of the whole parameter space is performed roughly once a year, unless hardware activities that can affect the minimum configuration are performed. Every month, a quick scan around the current minimum is done in order to monitor the stability of the noise level.

2.5.4 Diluition Refrigerator

The base temperature of 10 mK is reached by means of a continuous-cycle DRS-CF3000 Diluition Refrigerator, custom adapted for CUORE by Leiden Cryogenics with a nominal cooling power of 3 μW at 13 mK (2 mW at 120 mK)[73].

The working principle of this type of refrigerator is based on a specific property of the ^{3}He-^{4}He mixture at low temperatures [79]. Since the ^{3}He atoms follow the Fermi statistics, their kinetic energy is increased as their number density increases, thus the effective binding energy is reduced. At a ^{3}He concentration of 6.5% in the mixture and as T$\rightarrow$0, this effective binding energy vanishes, therefore no more ^{3}He atoms can be dissolved in ^{4}He. Above this concentration and below the temperature of 0.87 K, it is energetically more convenient for the ^{3}He-^{4}He mixture to separate into two different phases with different ^{3}He concentrations. One is the heavier *dilute phase*, mainly composed by ^{4}He atoms, and the other is the

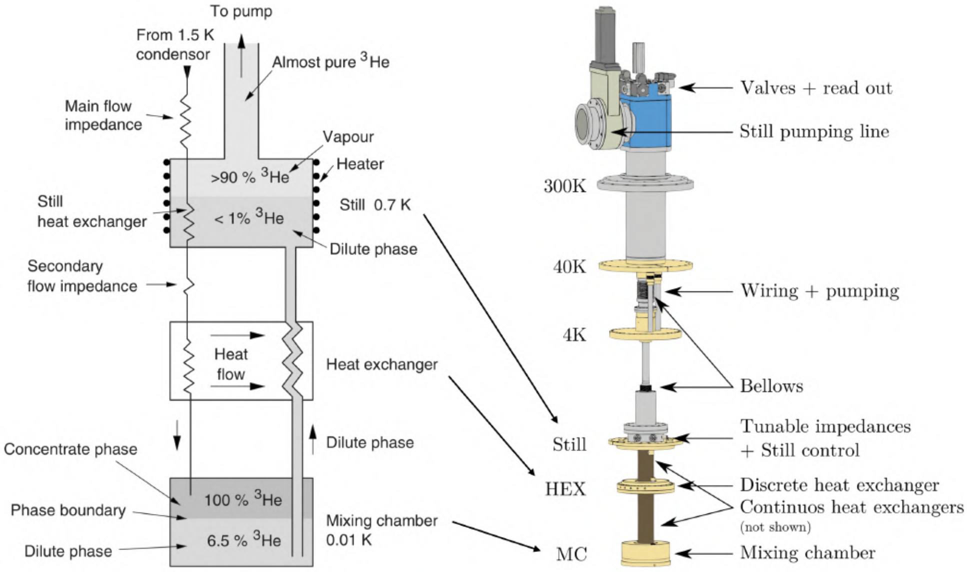

FIG. 2.13: Scheme of the working principle of a DR. The position of the different parts are shown in the rendering figure of the CUORE DR.

concentrated phase, which is rich in ^{3}He. The concentrated phase is characterized by a higher entropy with respect to the diluted one.

The cooling power of a DR is produced in the mixing chamber (MC) when ^{3}He atoms are forced to pass from the concentrated to the diluted phase. The heat needed for this endothermic process to occur for 1 mol of ^{3}He is given by

$$\Delta Q = T\Delta S = aT^2 \tag{2.11}$$

being $a = -84$ J K^{-2}. The heat is absorbed from the environment, thus producing cooling. In order to exploit this mechanism to generate cooling power continuously, it is necessary to keep removing ^{3}He atoms from the diluted phase, and re-introduce them in the cycle into the concentrated phase.

A scheme of the circuit allowing this operation is shown in figure 2.13. The two phases of ^{3}He-^{4}He mixture lie in the mixing chamber, the lighter concentrated one floating on the top of the heavier. The cooling power is produced at the phase boundary. The ^{3}He atoms are removed from the diluted phase by pumping the Still, that is directly connected to the MC below the phase boundary through a small pipe (see fig. 2.13-right). The Still chamber is at a higher temperature, around 0.7 K: since the ^{3}He vapour pressure is significantly higher with respect to ^{4}He at temperatures above 0.6 K, pumping the Still mostly evaporates ^{3}He atoms, although the ^{3}He concentration here is less than 1%. The removed ^{3}He is driven out of the cryostat and cleaned into liquid nitrogen traps; then it is re-introduced into the cryostat. Before reaching the MC, the ^{3}He flows through heat exchangers that cool it before entering the MC again in the concentrated phase. The cycle can now start again. On its way to the Still, the cold ^{3}He extracted from the dilute phase passes through the heat exchagers and cools the incoming ^{3}He to the MC.

Chapter 3

CUORE Data Taking and Processing

In the previous chapter, the working principle of a CUORE bolometer was described. It is now clear that a particle energy deposition into a crystal induces a resistance variation on the NTD thermistor; this is biased with a nearly constant current, thus such resistance variation is measured by acquiring the voltage difference at the edges of the NTD. The following chapter will be devoted to the discussion of the various steps that will lead the raw acquired signals to the high level analysis.

3.1 The Data Acquisition system

The Data Acquisition system (DAQ) has the important roles of digitizing, triggering and storing on disks the data coming from the NTDs. Before being digitized, the voltage signals are amplified by low noise gain amplifier front-ends and passed through 6 poles anti-aliasing Bessel filters. The software dedicated to the data acquisition system is named `Apollo`. This software has been specifically developed for CUORE in C++ programming language, and has the role of running parallel processes on various computers that constitute the CUORE DAQ. The CUORE DAQ system consists of 6 chassis hosting 64 digitizer boards, that sample the incoming data at a frequency of 1 kHz[80]. An optical link connects each board to a computer, where the digital samples are acquired and the process dedicated to the on-line triggering is run. These two operations are performed by parallel `Apollo` processes named *DataReader*. Three types of trigger can be fired to distinguish among different kinds of events: the *signal trigger* is intended to identify physics pulses, the *pulser trigger* flags the energy depositions produced by the silicon heaters and the *noise trigger* is a random trigger aimed at acquiring windows free from signal and pulser events, for the baseline stability monitoring and to compute the noise power spectrum. The flags applied in the three cases are named *IsSignal*, *IsPulser* and *IsNoise* respectively, and can be selected or rejected at different steps of the analysis chain. When a trigger fires, a waveform consisting of a 10 s time window is extracted, the first 3 s preceding the trigger flag (pre-trigger) and the remaing 7 s following the trigger (post-trigger) (fig. 3.1): this represents a CUORE event. The trigger algorithms available in CUORE for the identification of physics pulses

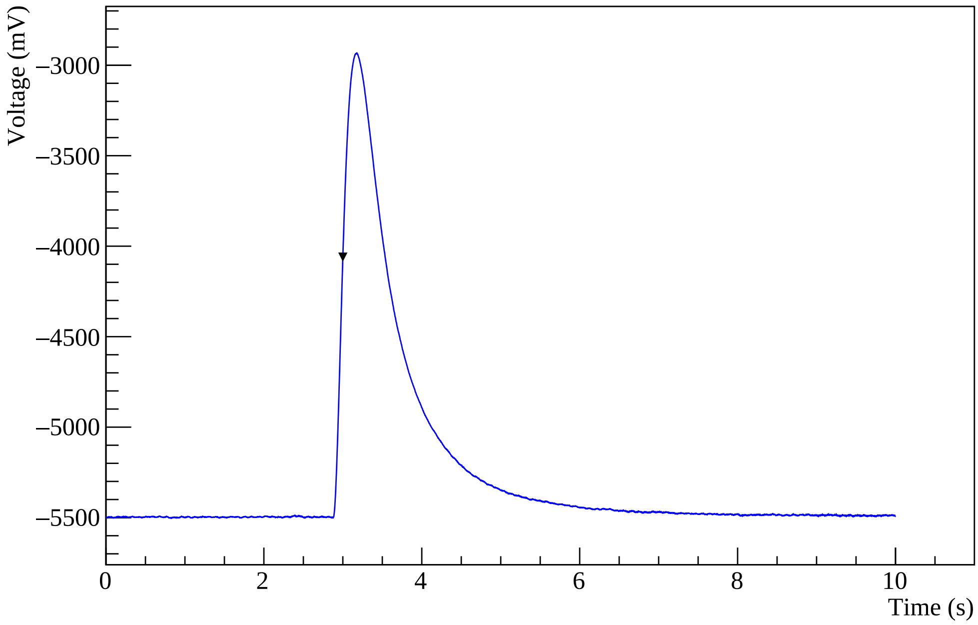

FIG. 3.1: Example of a CUORE signal event.

will be described in the next section 3.2.

The data are then copied from each DataReader to a shared memory accessed by a single computer running an `Apollo` process named *EventBuilder*, that takes care of the event construction and saves the triggered waveforms into files, the *Raw Data*, stored on disks. In addition to the Raw Data, the DataReader process also saves on disks the entire data waveforms without any applied trigger. These are written in ROOT format files named Raw Data Continuous Flow (RDCF). This files are used for offline analysis, and in particular they allow to perform offline triggering with different trigger algorithms. Information like the bolometers characteristic parameters and position, electronics mapping and trigger configurations are stored into a PostgreSQL database. A schematic representation of the DAQ is shown in figure 3.2.

Detailed discussions on the front-end electronics and the data acquisition system developed for CUORE can be found in [81][82].

3.2 Derivative and Optimum Trigger algorithms

Two distinct software trigger algorithms are used in CUORE to distinguish the signal particle pulses. The first one is the *Derivative Trigger* (DT). This trigger operates on the pulse rise time and fires when the baseline slope remains above threshold for a certain number of samples, namely for a minimum amount of time (*debounce*). The trigger threshold is set for each detector individually, depending on its noise level and working point. The DT is controlled by other three important parameters: the minimum time occurring between two consecutive triggers (*dead time*), the time interval during which the derivative is

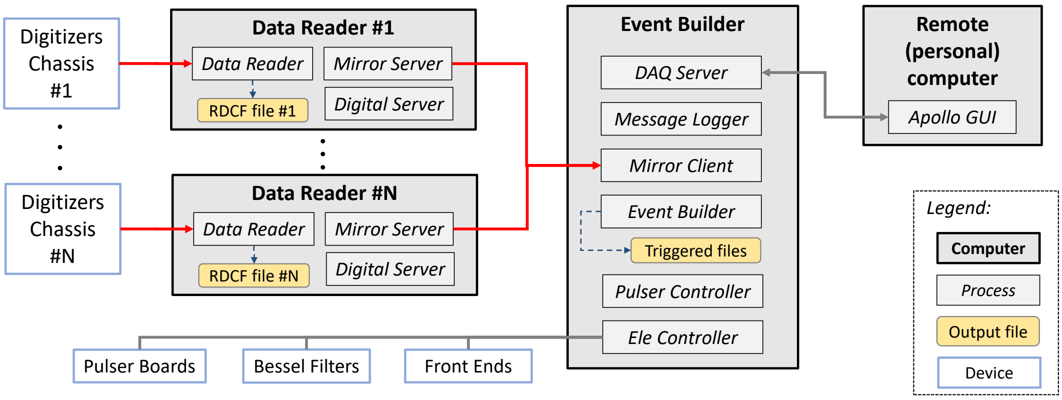

FIG. 3.2: Scheme of the CUORE data acquisition system. Details on the `Apollo` processes not mentioned in this work can be found in [82]. This figure is taken from the same reference.

evaluated (*average*) and the amount of time spent over threshold (*time-over-threshold*)[82]. The derivative trigger is used during the data acquisition and for the online data processing, whose goal is to provide a prompt feedback on the quality of the just acquired data (sec. 3.4.2): the reason for this choice is that the DT implementation and configuration in `Apollo` are straightforward, and it allows to achieve reasonably low thresholds of tens of keV. However, this trigger is inefficient in identifying small amplitude signals and hard pile up events, namely consecutive pulses occurring within a time window shorter than the trigger dead time.

The second trigger algorithm implemented in CUORE is called *Optimum Trigger* (OT). This is a threshold trigger applied on waveforms previously filtered with an optimum filter, with a transfer function given by [83][84] [1]:

$$H(\omega_k) = h\frac{S^*(\omega_k)}{N(\omega_k)}e^{j\omega_k t_M} \tag{3.1}$$

being $S(\omega_k)$ the Discrete Fourier Transform of the reference response function, $N(\omega_k)$ the detector noise power spectrum and t_M the time corresponding to the signal maximum. The implementation of this algorithm is more demanding with respect to the DT, since it requires a previous knowledge of the signal template and the noise power spectra, and much higher computing resources are needed. For this reason, it was decided in CUORE to apply OT offline on filtered RDCF waveforms, where the filter is constructed with the average pulse template and noise power spectrum computed during dedicated sequences of the first steps of the online data production, as described in sec. 3.4.2. The filtered data are characterized by a higher signal-to-noise ratio and reduced noise fluctuation. Using this algorithm is particularly advantageous since it allows to lower the energy threshold. Indeed, the low energy region of the CUORE spectrum is strongly affected by non-physical noise contributions, e.g. from electronic disturbances and mechanical vibrations; the information

[1]Parts of this paragraph are based on ref.[84] (Dompè V. et al., "Perspectives of lowering CUORE thresholds with Optimum Trigger").

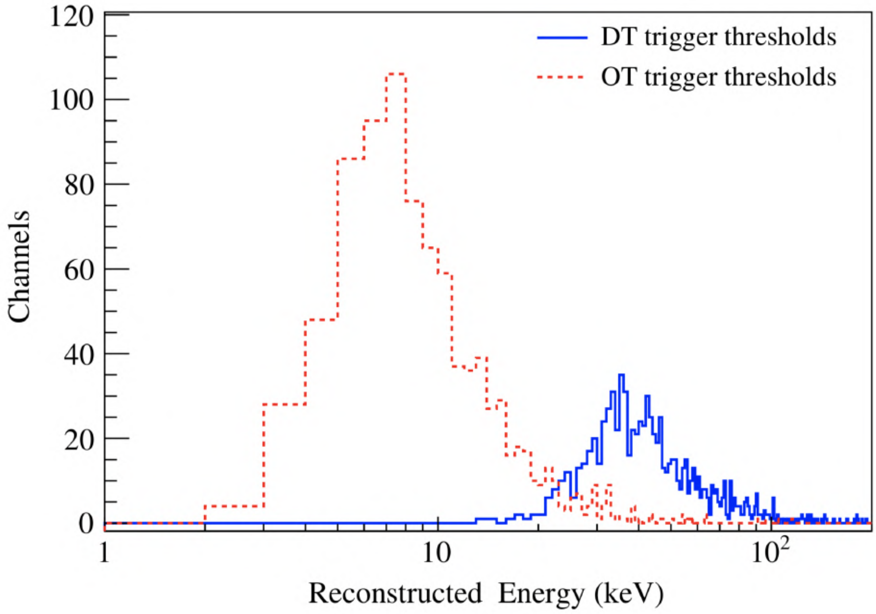

FIG. 3.3: Comparison between DT and OT energy threshold distributions at 90% trigger efficiency. Taken from [45].

on the signal pulse shape carried by the filter described in eq. 3.1 allows to distinguish between physical and non-physical pulses because of their different pulse shape. In this manner, the noise at low energies due to non-physical events is suppressed, and a detection energy threshold lowered by a factor 2-10 with respect to the Derivative Trigger is achieved (fig. 3.3) [45]. This opens to CUORE the possibility of studying low energy rare events such as WIMP direct detection and annual modulation signal, solar axions and supernova neutrinos.

3.3 CUORE data taking

The CUORE data collection is organized in *runs*, that are time intervals of data acquisitions in turn grouped into longer ones of ∼40-60 days called *datasets*. Different types of runs are performed depending on what the acquired data will be used for:

- *Test runs* are made when some optimization procedure is ongoing. Few examples are working point measurements (sec. 2.3), Pulse Tubes phase scan (sec. 2.5.3), hardware underground activities such as ordinary maintenance or specific cryostat interventions. Collecting data during these operations is crucial to constantly monitor the cryogenic parameters, to keep track of them and to perform the analysis dedicated to the specific optimization. The duration of a Test run is variable, it can last from few hours to one day depending on the time required for the ongoing activity;
- *Calibration runs* consist of data acquisitions of one day each in presence of radioactive sources facing the detectors. These data are used to convert the CUORE amplitude

spectrum in units of energy during the processing chain. More details on how this procedure is performed will be given in section 3.4.2;

- *Physics runs* are performed to collect the data addressed for physics analysis, such as the $0\nu\beta\beta$ decay search, the $2\nu\beta\beta$ decay half-life measurement and other rare processes studies. When the background data taking is ongoing, the detectors are not exposed to any radioactive source, and any type of underground activity in the CUORE hut is forbidden. A single background run usually lasts one day.

A typical CUORE dataset consists of an *initial calibration*, namely a set of 4 to 5 days of calibration runs performed at the beginning of each dataset, then ~30 days of background runs dedicated to a continuous physics data acquisition are made, and finally a new set of 4-5 days calibration runs are acquired for the *final calibration*. The final calibration of a dataset usually corresponds to the initial calibration for the following one. Test runs are performed during a dataset when required: for example, a short Pulse Tube phase scan is made at the end of each dataset to monitor the minimum noise configuration of the PTs, while working point measurements are performed weekly to monitor the stability of the NTD resistances over time.

3.4 Data monitoring and processing

During the acquisition of a dataset, it is crucial to constantly monitor the quality of the collected data. This includes checking the parameters related to the voltage signal coming from the bolometers as well as the status of the cryogenic system while the run is ongoing; an overview on this activity will be given in section 3.4.1. Every time a run is concluded, it undergoes a preliminary data processing, so that a more precise prompt feedback on the data quality is provided within one day from the run end. This allows to identify possible issues that could not be spotted during the real-time data monitoring. Such online processing will be described in sec. 3.4.2. Once the acquisition of an entire dataset is concluded, the Optimum Trigger is applied on the RDCF data waveforms and a full reprocess is performed. This consists of repeating the online processing with improved input parameters and then performing the higher level ones to the final data format used for the $0\nu\beta\beta$ decay search. Section 3.4.3 will go through the reprocess analysis chain.

3.4.1 Data quality real-time monitoring

The real-time monitoring during a run data taking is performed with the CUORE Online Run Control (CORC). This web interface allows to check data quality basic parameters computed and evaluated during the run, such as the baseline average, the baseline RMS, the average noise, signal and heater pulser rates, the heater pulser status. Besides the parameters related to the detector voltage signals, also the cryogenic system status is constantly monitored with CORC. Few examples of crucial parameters to check during the data taking are the temperature of the Mixing Chamber, which is in thermal contact with the TSP and thus with the bolometers, the Still and mixture flow pressures to monitor the Diluition Unit behavior, the Pulse Tube relative phases, the seismometers. Checking the seismometers is useful to identify seismic and external antropogenic events, such as activities occurring in the underground labs that can produce undesired vibrations propagating to the detectors.

The time intervals during which some misbehaving effect is observed for one or multiple bolometers are flagged as *Bad Intervals*. This information is stored in the database, thus all the events contained in these periods can be identified and excluded from the analysis. Examples of the most common reasons to set a Bad Interval are the presence of baseline instabilities due to external activities inducing vibrations, to electrical issues e.g. jumps in the grounding, the occurring of an earthquake. An earthquake produces a clearly recognizable effect, namely a sudden hike on all the detectors baseline that decreases back to its previous level in ~10-15 minutes. To confirm the hypothesis that a signal with this behavior is due to an earthquake, two cross-checks can be made: one is looking at the seismometers output, that in case of an earthquake will show a jump at the corresponding time, and the other is accessing the earthquakes list published on the Istituto Nazionale di Geofisica e Vulcanologia (INGV) website.

3.4.2 Online processing

The official CUORE data processing is performed with `Diana`, the data reconstruction and analysis software developed by the Collaboration. `Diana` is a C++ based software supporting ROOT packages. The code is organized in *modules*, each module looping over the single events, and for each event it executes a series of tasks such as reading the data, computing quantities, applying filters, writing the output. A group of modules forms a *sequence*: it typically starts with a *Reader* module aimed at reading the input ROOT files, then a coherent list of tasks contained in the present modules and filters are executed, and finally a *Writer* module is in charge to write the output variables of the sequence into the input data files or in new ones.

The day-by-day collected runs are subject to the first data processing steps, whose goal is to reconstruct the CUORE energy spectrum in calibration and in background conditions starting from the raw data acquired by `Apollo`. The triggered waveforms $v_i(t)$ of the i-th bolometer in the time domain is modeled as the sum of two terms[85]:

$$v_i(t) = B_i \cdot s_i(t) + n_i(t) \tag{3.2}$$

where B_i is the signal response amplitude, $s_i(t)$ is the detector response function and $n_i(t)$ represents a randomly distributed noise term. The amplitude of the signal can be well approximated by the product of the bolometric gain $G_i(T)$ depending on the working temperature, and a term $A_i(E)$ depending on the energy released in the bolometer:

$$B_i = G_i(T) \cdot A_i(E) \tag{3.3}$$

Starting from the triggered waveform, the first level data processing extracts the energy spectrum going through the following steps:

- preprocess;
- evaluation of the pulse amplitude;
- thermal gain stabilization;
- energy calibration.

Preprocess

The *Preprocess* is the first sequence of the analysis chain run by `Diana`. The raw data files are taken as input and the first basic quantities related to each bolometer signal amplitude, noise level and pile up identification are evaluated. The most relevant ones that will be often used during the whole analysis chain are the baseline and the pile up parameters.

The baseline parameters are evaluated from the first 2.25 s of the triggered waveform, in order to register the information on the detector condition just before a particle interaction. The *Baseline* parameter corresponds to the voltage signal of the NTD in mV, and gives an indication on the bolometer working temperature at a fixed offset. The *BaselineSlope* and *BaselineRMS* parameters are both computed with a linear regression fit on the considered events of the pre-trigger, and correspond to the slope of the linear function and to the RMS deviation of the data from the best fit respectively.

The two relevant parameters for the identification of pile up events are the *SingleTrigger* and the *NumberOfPulses*: the first is a boolean flag which is set to 1 when only one trigger is fired in the event window, while the latter returns the number of peaks in the window, evaluated by counting a peak whenever the waveform derivative exceeds a threshold.

The ROOT files produced as output of the Preprocess sequence are used as input data for the following steps of the analysis procedure.

Pulse amplitude evaluation

The *Amplitude* sequence is dedicated to the evaluation of the signal amplitude B_i expressed in eq. 3.3. The aim is to maximize the signal-to-noise ratio. A frequency-based digital Optimum Filter (OF) designed to this purpose is applied on the data at this step. This filter acts on the whole event waveform and extracts the amplitude estimation for each pulse, weighting the Fourier components of the signal and exploiting the noise power spectrum to reduce the impact of the noisy frequencies. The transfer function of the OF in eq. 3.1 can be re-written according to the waveform expression in 3.2, thus the filtered pulse in the frequency domain for the i-th bolometer is given by:

$$V_i^{OF}(\omega) \propto e^{i\omega t_M} \frac{S_i^*(\omega)}{N_i(\omega)} V_i(\omega) \tag{3.4}$$

being $V_i(\omega)$ and $S_i(\omega)$ the Fourier transforms of the non-filtered signal $v_i(t)$ and the detector response function $s_i(t)$ respectively, while $N_i(\omega)$ is the detector noise power spectrum. The detector response function and the noise power spectrum are computed prior to the OF by two sequences, i.e. the *Average Pulse* (AP) and the *Average Noise Power Spectrum* (ANPS). The AP is evaluated from calibration data to take advantage of the higher trigger rate ($\sim$100 mHz): for each bolometer, many signal pulses are selected and their waveforms as in eq. 3.2 are normalized and averaged together, so that the noise term cancels out. The ANPS is instead extracted from background data: the $<$10 mHz trigger rate is suitable to get waveforms containing clean noise events, with no components from pulses tails. Indeed, their presence in noise samples would introduce signal frequencies in the average noise power spectrum, and these would be filtered by the OF with a consequent worsening of the signal-to-noise ratio. To avoid this, only samples with a BaselineSlope below a certain threshold are selected. These waveforms are then Fourier transformed and averaged together.

Thermal gain stabilization

As mentioned in sec. 2.2, small drifts in the bolometers operating temperature are responsible for variations in their gain $G_i(T)$. As a consequence, the reconstructed amplitudes corresponding to the same energy depositions can be different, and this would spoil the energy resolution. In order to compensate this effect, two parallel thermal stabilization techniques are used in CUORE: the *heaterTGS* and the *calibrationTGS* stabilizations[85]. During the online data production only the *heaterTGS* stabilization is performed to provide a faster feedback on the data quality, but also the *calibrationTGS* technique, applied at the moment of the full reprocessing, will be described here for the sake of completeness.

The *heaterTGS* stabilization exploits the pulses fired during each run by the heaters glued on the bolometers: as the energy of these pulses is fixed, any variation in their reconstructed amplitude is attributed to a change in the bolometric gain. As previously mentioned, the baseline parameter is a proxy for the detector temperature right before the pulse is measured; thus the gain $G_i(b)$ as a function of the baseline can be extracted for each bolometer-run through a linear regression of the measured heater pulses amplitudes versus the baseline value (fig. 3.4-a). The gain dependence on the baseline can be assumed as linear for small temperature variations. The extracted coefficients for $G_i(b)$ are then used to correct the detector response, and the stabilized amplitude (fig. 3.4-b) is obtained as:

$$B_i^{\mathrm{stab}} = A_0 \cdot \frac{B_i}{G_i(b)} \tag{3.5}$$

where A_0 is generally set at a value corresponding approximately to the measured energy, and B_i is the observed (non-corrected) detector response as appearing in eq. 3.3.

Some detectors have non-functioning heaters, therefore this method cannot be applied. These bolometers can be however stabilized during the reprocessing with an independent technique: the *calibrationTGS* stabilization. This is similar to the *heaterTGS* one, but in

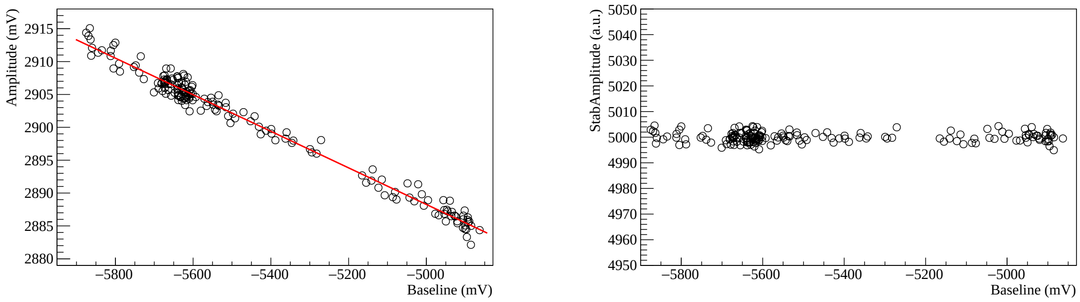

(a) (b)

FIG. 3.4: Example of the heater pulser events amplitude distribution as a function of the baseline for a single bolometer before (a) and after (b) the stabilization heaterTGS algorithm is applied.

this case the 2615 keV γ events from ^{208}Tl in initial and final calibration runs are used as reference. Since these data are ~30 days far in time from each other, the gain dependence on the baseline is evaluated with a second order polynomial function to account for possible non linearities over a longer time period. In order to produce valid coefficients for the entire dataset, working point measurements are performed weekly for a careful monitoring of the voltage offset, to further correct the amplitude for NTD resistance variations.

Energy calibration

At this step of the data processing, the data from calibration runs are used to convert the stabilized amplitude from the previous step in units of energy. To this purpose, during calibration runs the bolometers are exposed to radioactive sources of ^{232}Th and ^{60}Co: for each detector, the stabilized amplitudes of four γ lines, namely the 511 keV e^+ annihilation peak, the 1173 keV and 1333 keV lines from ^{60}Co and the 2615 keV γ from ^{208}Tl are evaluated in order to extract the calibration function aimed at mapping the amplitude in energy. A fit with a Crystal Ball function [86] plus a linear background is performed on each γ peak to estimate their positions in units of stabilized amplitude. These are then fitted with a second order polynomial energy vs amplitude calibration function:

$$E = a \cdot A_{\text{stab}} + b \cdot A^2_{\text{stab}} \tag{3.6}$$

and the calibration coefficients a and b are extracted for each bolometer-dataset. These coefficients are applied to the stabilized amplitude both in calibration and in background data, and the energy spectrum for a given bolometer-dataset pair is obtained. An example of calibration spectrum is shown in figure 3.5.

An additional sequence is run in the online data production after the spectrum calibration: the *Blinding* sequence. This is aimed at masking any possible signal at the $Q_{\beta\beta}$ peak of ^{130}Te $0\nu\beta\beta$ decay. A brief description of the blinding algorithm adopted in CUORE will be given at the end of sec. 3.4.3: indeed, during the full reprocessing, this sequence represents the very last step of the data production chain, but during the online data processing

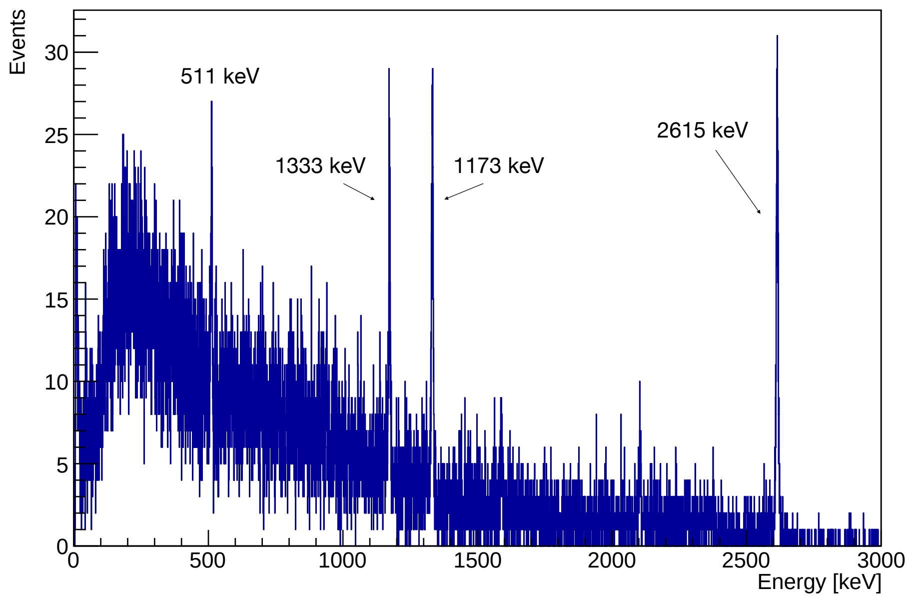

FIG. 3.5: Example of a CUORE calibration spectrum for a single bolometer. The four gamma lines used to by the calibration algorithm to reconstruct the energy variable are shown.

it is necessary to look at the background spectrum in order to provide a feedback on the data quality. Before doing this, applying a blinding procedure is compulsory to avoid any possible bias during the future analysis steps.

3.4.3 Offline reprocessing

When the acquisition of an entire dataset is concluded, the AP and ANPS templates obtained from the online processing are used to build the Optimum Trigger (OT) algorithm that is applied offline on the continuous RDCF data waveforms. After the retriggering, the dataset is reprocessed from the beginning: in addition to the just described *Preprocess*, *Amplitude*, *Stabilization heaterTGS*, *Stabilization calibTGS* and *Calibration* sequences, the processing goes through higher level analysis steps to the finalized data used for the analysis of ^{130}Te $0\nu\beta\beta$ decay and other physics processes. In this section, the remaining steps of the data processing will be described:

- coincidences;
- pulse shape analysis;
- blinding.

Coincidences

In CUORE, different particle interactions can induce a signal into one or more crystals. For example, the $0\nu\beta\beta$ decay produces two electrons whose energies are expected to be

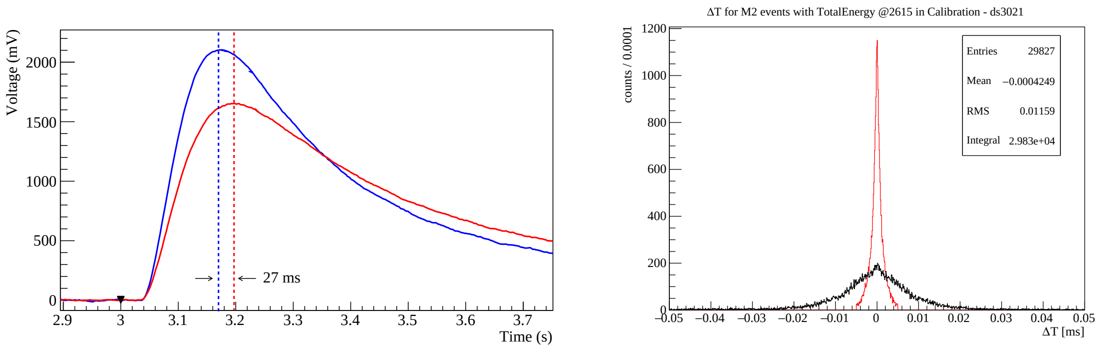

(a) (b)

FIG. 3.6: (a) Pulses from two different detectors of the same tower are represented by the blue and the red lines. The intrinsic difference of their pulse shape is responsible for a misalignment of the positions of the maximum amplitudes (dotted lines), whose difference corresponds to a 27 ms jitter. (b) Time differences distributions of multiplicity 2 events before (black line) and after (red line) the jitter corrections.

fully absorbed into a single detector[2], while a 2615 keV γ undergoing Compton scattering can produce energy releases into two crystals within a short time interval, summing up to 2615 keV. The granularity of the CUORE detector allows to perform a coincidence study, to determine if signals detected within a short time and spatial distance can be attributed to the same interaction. In this case, these are referred to as *coincident signals*, and they are attributed a *multiplicity*. The multiplicity can be defined as the number of crystals simultaneously involved in an interaction. Two or more crystals involved in the same interaction form a *multiplet*.

Studying the coincidences is advantageous to different purposes. First of all, it allows to perform background discrimination for the $0\nu\beta\beta$ decay search: in fact, all the events with multiplicity > 1 are identified as background and rejected in this analysis. In addition, from the coincidence study it is possible to obtain information on the position of the background sources in the detector; a more detailed discussion on this topic will be given in chap. 4.

Two or more events in time coincidence must be reconstructed within a defined time window. To evaluate this time window, it is necessary to consider that simultaneous events in different crystals can exhibit a time delay due to their different intrinsic pulse shapes. Indeed, the rise time of a pulse can differ up to tens of ms from crystal to crystal, depending on its features. As a consequence, each pair of bolometers is characterized by a typical time delay even between two simultaneous events: this time delay is referred to as *jitter*. An example of this effect is shown in figure 3.6-a.

The first step for the time coincidences calculation in CUORE consists of evaluating the jitters between all the crystals pairs. This can be done by studying the various detectors responses to simultaneous events. The Compton scattering of the 2615 keV ^{208}Tl line in

[2] The $0\nu\beta\beta$ decay containment efficiency is evaluated by Monte Carlo simulations: it results to be 88.35% for ^{130}Te[45] and 97.59% for ^{128}Te (this work). Details on how this calculation is performed can be found in sec. 6.1.

calibration runs is chosen as a sample of simultaneous events, thus multiplicity 2 events whose energies add up at 2615 keV are selected. This algorithm for the jitters computation is run for single towers and a wide time window of 100 ms is used, so that enough statistics is included but at the same time the accidental coincidences given by events occurring in pairs of far crystals are excluded. A reference bolometer is taken for each tower, and the jitter of each crystal with respect to the reference one in the same tower is measured. The jitters among crystals belonging to different towers are then evaluated by measuring the time difference between the trigger flag and the time corresponding to the maximum of the filtered pulse for heater pulsers events in the reference crystals of the 19 towers. At this point, the jitter of all the CUORE detectors can be computed by combining those of the bolometers in the same tower and those of the reference crystals of different towers. Using the jitters to correct the time differences between simultaneous events in different crystals allows to significantly reduce the coincidence window: figure 3.6-b shows that the width of time difference distribution of multiplicity 2 events before and after the jitter correction is reduced from 100 ms to 10 ms. The possibility to choose a narrower time window is crucial to reduce the rate of accidental random coincidences and hence to improve the event selection efficiency. The final step of the `Diana` coincidence sequences is to identify all the events occurring within the coincidence window, assign them a multiplicity and store this information, together with the total energy given by the sum of the coincident events energies.

The possibility to include also a geometrical cut in the coincidences calculation has been recently implemented in CUORE. This provides a further rejection of accidental coincidences, excluding all the cases in which bolometers located far from each other randomly trigger within the coincidence window. A typical value of a radial cut in CUORE is 150 mm.

Pulse Shape Analysis

The CUORE full calorimetric approach does not allow to distinguish among physical pulses due to α or β/γ interactions. The aim of the Pulse Shape Analysis (PSA) algorithm is then to identify and discriminate among pulses due to particle energy depositions and other non-physical signals that can fire the trigger as well, such as noise spikes, abrupt disturbances of the baseline or pile up events. Six pulse shape parameters are evaluated and combined to extract the analysis cut to reject these events:

- *RiseTime* - time interval taken by the pulse to pass from the 10% to the 90% of its total amplitude. Baseline spikes due to electronic noise can be distinguished from their shorter rise time with respect to physical pulses, while a larger value usually identifies pile-up events;

- *DecayTime* - time interval that the pulse takes to pass from the 90% to the 30% of its total amplitude. As for the rise time, electronic spikes are characterized by a significantly shorter decay time compared to that of thermal pulses, while pile-up events again can show a larger value if a pulse appears on the tail of another;

- *BaselineSlope* - slope resulting from the best linear fit of the first 2.25 s pre-trigger events (see Preprocess step). A baseline slope significantly deviating from 0 typically indicates a pulse occurred on the tail of a previous one that is out of the event window, resulting in a misreconstruction of the pulse amplitude;

- *OFDelay* - time interval between the beginning of the event window and the OF filtered pulse maximum amplitude. As described in the Coincidences processing step, each bolometer is characterized by a *jitter* that makes the OFDelay different for each detector, but if an event shows a value strongly deviating from the average, it means that the pulse amplitude is misreconstructed;

- *Test Variable Left (TVL) and Test Variable Right (TVR)* - sum of the squared differeces, computed sample by sample, between the filtered pulse and the AP template, on the left and on the right of the OF filtered pulse maximum respectively. These parameters give an indication on how much the pulse shape differs from that of the AP.

A slight dependence on energy is observed for all the shape parameters, together with a widening of their distributions at low energies due to the larger contribution of noise events. This energy dependence can be evaluated on a reference sample of particle pulses. Multiplicity 2 events are selected to this purpose, since it has been verified that the number of accidental coincidences due to non-physical events is negligible. From this data sample, the distributions of the median and the median absolute deviation (MAD) of each parameter as functions of energy are extracted from fits with phenomenological functions, since no model able to describe the shape of these distributions is currently available. Different distributions are also extracted for each detector, in each dataset. Once these distributions are obtained, it is possible to define the normalized pulse shape parameters P_i^{norm} as:

$$P_i^{\mathrm{norm}} = \frac{P_i - f_{\mathrm{median}}(E)}{f_{\mathrm{MAD}}(E)} \tag{3.7}$$

where P_i is any of the six pulse shape parameters for the i-th event, while $f_{\mathrm{median}}(E)$ and $f_{\mathrm{MAD}}(E)$ are the best fit phenomenological functions for the considered parameter. For normalized parameters the energy dependence is eliminated, hence energy-independent cuts can be set. The cut establishing which events pass the PSA and thus will be used for the analysis of the $0\nu\beta\beta$ decay and other processes must take into account all the six pulse shape parameters and the possible correlations among them. To identify and reject the outliers corresponding to deformed and non-physical pulses in the parameters normalized distributions, the Mahalanobis distance M_{dist} is evaluated for each event. If an event is considered as a point $\vec{x}$ in the 6-dimensional space of the PSA parameters, the Mahalanobis distance is defined as its distance from the 6-dimensional parameters distribution[87][88]:

$$M_{\text{dist}} = \sqrt{(\vec{x} - \vec{\mu})\Sigma^{-1}(\vec{x} - \vec{\mu})^T} \tag{3.8}$$

where $\vec{\mu}$ is the mean of the distribution and Σ is the variance-covariance matrix accounting for the parameters correlations. A cut on M_{dist} is finally applied to select the data that will be used for the physics analysis.

Blinding

The final step of the reprocessing chain consists of running the *Blinding* sequence. This is aimed at hiding any possible signal or background fluctuation in the physics spectrum at the ROI of ^{130}Te $0\nu\beta\beta$ decay, so that no bias can be introduced during the following analysis optimization procedures. The blinding technique adopted by CUORE consists of a data salting: an unknown fraction up to 40% of randomly selected events whose energy is reconstructed in a ± 10 keV window around the 2615 keV peak from ^{208}Tl is shifted by -87 keV, thus around the $Q_{\beta\beta}$. The same fraction of events which reconstructed energy is in the $Q_{\beta\beta}$ window is shifted by $+87$ keV, towards the 2615 keV line. The effect of this procedure is that a fake peak at the $Q_{\beta\beta}$ energy is produced in the spectrum; the true energy of each event is encrypted and stored. The unblinding keys are guarded by the spokesperson, and only until the collaboration agrees for it at the end of the analysis and fit finalization the unblinding is performed.

Chapter 4

The CUORE Background Model

One of the fundamental aspects for an experiment searching for rare events consists of identifying, locating and evaluating the intensity of the sources that contribute to the observed spectrum. Indeed, several phenomena besides $0\nu\beta\beta$ decay can originate events in the region of interest, and their understanding is crucial to reach the CUORE designed background level of less than 10^{-2} counts/keV/kg/y. As discussed in sec. 2.1, the CUORE predecessors demonstrated that the major contribution to the ROI was due to the residual radioactive contamination of the detector and the cryostat components. In particular, the following dominant background sources were identified [89]:

- traces of long-lived nuclei such as ^{40}K, ^{238}U, ^{232}Th in the materials facing the detectors, i.e. the cryostat copper shields and the holder structures;
- residual contamination of ^{238}U and ^{232}Th on crystals bulk and surface;
- ^{210}Pb implanted on surfaces from environmental ^{222}Rn;
- contamination of nuclei produced by cosmogenic activation of tellurium and copper, e.g. ^{60}Co.

^{238}U and ^{232}Th give rise to decay chains, whose elements contribute to the measured spectrum with a continuum distribution as well as with several α, β and γ lines. The effect of the residual presence of radon in environment was also revealed: ^{220}Rn and ^{222}Rn gas can easily diffuse through the detector components and decay through α-emitting chains. In particular, the decay chain of ^{222}Rn produces the long-lived ^{210}Pb, which remains on the materials surfaces and gives rise to additional contributions to the background, one of the most critical being the α decay of ^{210}Po. The presence of cosmogenic ^{60}Co can produce a different contribution to the ROI depending on its location. If this is present in the crystal bulk, the simultaneous absorption of the β energy together with the sum of the two emitted γ rays (2505 keV) can introduce critical contributions to the $Q_{\beta\beta}$. It was verified in CUORE that only a negligible quantity of ^{60}Co is present in the crystals, and that this does not represent a critical background source. The ^{60}Co contamination located in the copper structures can produce at most a peak in the ROI at 2505 keV due to the sum of the two γ rays. A contribution from environmental neutrons and γ rays from cosmic ray muons is also expected, although their fluxes are considerably reduced at the CUORE experimental site thanks to the Gran Sasso mountain rock coverage (see chap. 2).

In light of this past experience, CUORE was realized according to stringent radioactivity constraints to reduce the background contribution[57] with respect to its predecessors: strict production and handling protocols, special cleaning procedures and validation criteria were adopted during the detector construction to minimize the contamination level (sec. 2.4, 2.5). Prior to their selection, all the materials destined for the CUORE realization were subjected to a wide and meticulous screening campaign, during which dedicated measurements on bulk and surface contamination were performed by means of the most sensitive available techniques such as α and γ spectroscopy, inductively coupled plasma mass spectrometry (ICPMS), neutron activation analysis (NAA), TeO_2 detector spectrometry [89]. As a result, the CUORE materials were selected according to their contamination level, fulfilling a radiopurity requirement up to few nBq/cm^2 for the surfaces of the parts closer to the crystals.

The data obtained from previous experiments are used to evaluate the CUORE background budget, together with the results of the CUORE-0 background analysis[90]. Indeed, CUORE-0 consists of one of the CUORE towers and the only difference is therefore the hosting cryostat, thus it is possible to exploit the information obtained by CUORE-0 on the common contamination activities. The reconstruction of the CUORE background budget is performed by means of a detailed Monte Carlo (MC) simulation, which includes information on the geometry of the experimental setup, the known radioactive contaminants, the radiation interactions with the different CUORE materials, the detector response and other instrumental effects such as the resolution and the thresholds. Section 4.1 is dedicated to the description of the MC simulation tools. The precise activity of the background sources contributing to the spectrum is then evaluated through a Bayesian fit of the measured data based on MC simulations. This approach is illustrated in section 4.2.

As it will be shown in sec. 4.2, the background model (BM) constructed with this approach provides a very good description of the CUORE spectrum. Nevertheless, including new inputs from studies performed by direct observation of the acquired data would improve the present background model and would help in achieving more precise and correct interpretation of the measured spectrum. The BM is fundamental not only for the search of $0\nu\beta\beta$ decay of ^{130}Te, but also for rare event studies requiring a spectral fit, such as the precise measurement of the ^{130}Te $2\nu\beta\beta$ decay half life (sec. 5.2), the search for a possible CPT violation signature in $2\nu\beta\beta$ decay, the Majoron emission search, and other rare transitions analysis like the double beta decay of ^{128}Te (chap. 6), of ^{120}Te and to the excited state of ^{130}Te. During my PhD activity, I took part to the CUORE Background Model working group, including few people, dedicated to the detailed study of the CUORE measured spectrum with the aim of improving the present background model. In this framework, I was responsible for the study of the alpha region of the spectrum. The outcome of this work is illustrated in section 4.3.

4.1 Monte Carlo simulations of the background sources

The Monte Carlo (MC) simulation codes developed to evaluate the effect of the CUORE background contamination are based on the GEANT4 package[91]. The production of a simulated spectrum takes place in two steps. The first one is performed by the `qshields` tool, which is devoted to the evaluation of the effects of the background sources on the detector. This proceeds through the proper generation of particles produced by radioactive decays and their propagation through the experimental setup, until eventually reaching the detector elements. The full CUORE geometry, from the bolometers to the outer radiation shields, is included. The output of `qshields` does not include the signal formation and the data acquisition and analysis details. It is therefore different from the CUORE data, since no experimental parameters such as the energy resolution, the trigger dead time, the pile-up window, etc. are included. In particular, no coincidences are associated to the simulated events, thus simultaneous energy releases in the same bolometer are not added together (e.g. the two electrons emitted in a $2\nu\beta\beta$ decay are treated as separate particles). Hence a second tool, `g4cuore`, is run to process the simulations obtained by `qshields` with the aim of applying the detector response parameters and the coincidences. As a result, the output of `g4cuore` is thus close to the real CUORE data after the whole processing chain is completed. In the following sections 4.1.1 and 4.1.2, the operation of `qshields` and `g4cuore` will be described.

4.1.1 MC simulations with `qshields`

The `qshields` tool is used for the MC simulation of the CUORE setup geometry and of primary and secondary particles propagating through it[89]. This GEANT4-based software written in C++ programming language allows to account for the CUORE geometry in detail: its simulation includes the 988 TeO_2 crystals, their copper supporting structure, the PTFE holders, the wire trays, the NTD thermal sensors, the silicon heaters, the calibration source guiding tubes, the various thermal copper shields, the internal and external Roman and modern lead shields, the cryostat flanges, rods and cables, the external polyethylene shield. The CUORE model as implemented in the MC simulation is shown in fig. 4.1.

Any element of the experimental setup can act as an independent source of bulk or surface contamination, whose geometrical distribution into the material can be specified: in CUORE, bulk impurities are uniformly distributed into the various setup elements, while different profiles can be selected to model the depth profile of the surface contamination. All the particles and decays of interest can be generated with `qshields`, as well as their energy and location within the experimental setup:

- independent particles: γ rays, electrons, α particles and related nuclear recoil, heavy ions, neutrons, muons and many others can be generated either with a monochromatic

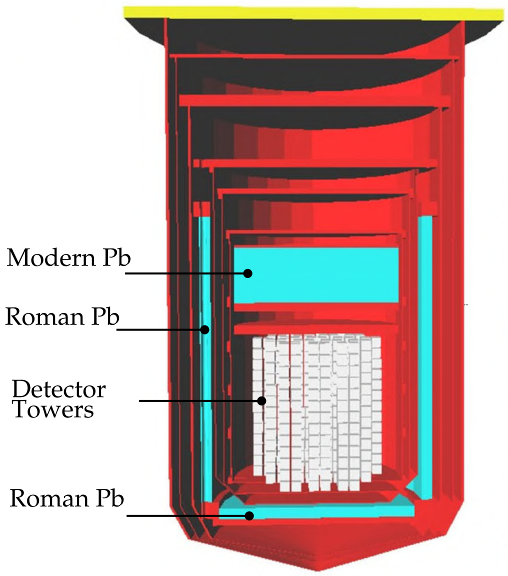

FIG. 4.1: A 3-D representation of the CUORE apparatus as implemented in the CUORE Monte Carlo simulations. Taken from [89].

or a specific continuous energy distribution;

- single nuclear decay: an atom (A,Z) can be selected as a radioactive source, and in this case the particles produced in the decay are generated and propagated across the detector as well;
- decay chains: to correctly simulate the subsequent transitions of a radioactive chain in secular equilibrium, e.g. the natural radioactivity, an ad-hoc database (*G4RadioactiveDecay*) is used: this allows to concatenate the single decays of the daughter nuclei accounting for each of their half lives. The possibility of accounting for breaking points of secular equilibrium in the chain is also implemented;
- double beta and exotic decays: the possibility to generate the double beta decay with or without emission of neutrinos, to the excited states, with or without emission of Majorons is also implemented. The spectral shape of the two emitted electrons sum energy in the 2ν mode can be modeled according to results available in literature[92][93]; alternatively, more detailed numerical calculations from [27][34] can be used.

The particle generation and propagation through the various materials can occur according to several processes and models: these are included into physics lists, that are part of the simulation code. A compromise between the precision and the required computing time is necessary: an efficient choice usually consists of selecting a physics list where only processes relevant for the given energy range or the particle nature are considered. Several physics lists are available in literature for high and low energy physics. In CUORE, the *Livermore* Physics List is employed to describe the electromagnetic interactions such as the propagation of electrons and photons: this was extensively tested at the interesting energy range within CUORE-0 and other applications, and its precision resulted to be suitable for the scope of the CUORE background reconstruction. The *QGSP_BERT_HP* Physics List is instead used to account for adronic interactions such as neutrons propagation in the detector, while the muons contribution is accounted for by the *G4MuIonization*, *G4MuBremsstrahlung*, and *G4MuPairProduction* lists.

The primary and secondary particles are propagated through a step tracking, where the size of the step depends on the particle type, its carried energy and the involved material. A production optimization cut is implemented for different CUORE volumes to further improve the simulation performance: the production cut is set at 1 cm and 1 mm for lead and copper parts, respectively. After propagating across the detector, the generated particles are detected by the TeO_2 crystals. The resulting deposited energy and time of interaction are saved and stored in the `qshields` output files.

4.1.2 Processing the MC simulation with `g4cuore`

The output files produced by `qshields` do not include the information related to the detector operation details (e.g. time development and energy response), nor the event coincidences and other parameters computed during the data analysis chain, thus they cannot be compared with the real CUORE data. The MC simulations are then processed with `g4cuore`, an additional tool that folds all the detector-specific quantities as well as the ones resulting from the data analysis steps, so that the experimental data format is reproduced. The most relevant parameters include:

- **trigger threshold**: as mentioned in sec. 3.2, the trigger thresholds of the CUORE bolometers are individually set according to their response and noise level. To account for this in `g4cuore`, the possibility of passing a file including the experimental thresholds of each detector is implemented. Alternatively, a step function or an Error Function can be used as threshold functions for all the bolometers if selected by the user;

- **integration window**: the energies of events occurring in the same detector within this window are summed up and considered as a single event;

- **pile-up parameters**: a symmetric or asymmetric time window around the event interaction time can be specified to identify pile-up events;

- **trigger dead time**: the dead time corresponding to the derivative trigger is accounted for. For a given event, each other event occurring in the same detector within the dead time is ignored, and the first one is flagged as a pile-up;

- **coincidences**: the time and spatial cuts used in the corresponding sequence of the data processing can be set to calculate the coincidences accordingly, and a multiplicity parameter is then assigned to each event;

- **energy resolution**: in order to account for the detector response in energy, a smearing gaussian is applied to each energy release. From the study of the CUORE detector response function, an energy dependence of the resolution is observed and is modeled with a parabolic function (details on this topic will be discussed in sec. 5.1.2). The possibility of applying an energy dependent resolution is implemented in `g4cuore` accordingly;

- **PSA efficiency**: the curve describing the energy dependence of the PSA cut efficiency as evaluated from the experimental data (sec. 5.1.1) can be taken into account passing a specific file to `g4cuore`;

- **excluded bolometers**: the detectors failing some sequence of the CUORE data processing are excluded from the final analysis. These are then listed into a file, which can be passed to `g4cuore` to exclude them from the final simulation output as well;

- **quenching factor**: it has been observed in CUORE and its predecessors[94][95] that the energy deposited by α particles is reconstructed at a slightly higher value with respect to the nominal one. `g4cuore` accounts for this effect and corrects the energy of the α particles multiplying it by a *quenching factor*. A detailed discussion on this topic is reported in sec. 4.3, since the evaluation of the quenching factor in CUORE is part of this PhD thesis work.

While the physics processes remain unchanged and thus there is no need for often re-running the MC simulations, the outcome of the data processing can change after optimization procedures, and `g4cuore` should be re-run accordingly. The advantage of employing two separate tools for the particle generation and propagation and for their processing is that the latter part can be quickly run with different settings every time it is needed, avoiding to always execute the much more time and CPU consuming simulations with `qshields`.

4.2 The CUORE Background Model construction

The contribution of each simulated radioactive source to the CUORE measured spectrum can be disentangled and quantified through the reconstruction of a proper Background Model. To accomplish this goal, besides the response of each detector, also the granularity of the CUORE detector is exploited to study the event topology by means of the coincidences evaluation. Three energy spectra are then considered: the multiplicity 1 (M1) spectrum accounting for single-hit events only, the multiplicity 2 (M2) spectrum including just double-site energy releases, and the multiplicity 2 sum (M2sum) spectrum, which is constructed by summing the single energies of events belonging to the same M2 multiplet. Higher multiplicities are not considered for the BM construction, since the fraction of β and γ radiation at M$\geq$3 is small and does not provide new meaningful information[96], and the α contribution becomes negligible at M>2. As it will be discussed in sec. 5.1.1, MC simulations show that the energy deposition due to double beta decay of ^{130}Te is fully contained by a single bolometer $\sim$88% of the cases, while the majority of the background interactions involve two or more crystals. Indeed, the study of M2 and M2sum spectra is useful for a better understanding of the background: it will be shown in section 4.3 that these signatures allow to distinguish between bulk and surface contamination.

For both the simulated and the experimental spectra, a binning with variable size is chosen[90]: counts corresponding to the same γ or α peak are added to the same bin, and bins counting less than 30 events are unified with the neighbouring ones. This choice allows to reduce the effect of statistical fluctuations and to avoid systematic uncertainties related to the non-gaussian shape of the peaks due to the detector response (see sec. 5.1.2), and to our ignorance about alpha line shape details (see sec. 4.3.1).

In CUORE, `qshields` and `g4cuore` are used to simulate 62 background contributions[96]: these were identified as a result of the previous knowledge from the CUORE predecessors, from previous measurements and from the study of the contributions to the CUORE energy spectrum, which provided information on the sources position in the experimental apparatus. The number 62 does not refer to the same number of contamination: different simulations can refer to the same source but in different locations. For each source, a known number N_{MC} of primary interactions are generated. The Background Model (BM) is a Bayesian fit simultaneously performed on the M1, M2 and M2sum spectra of the experimental data with a linear combination of the 62 simulations (an introduction to the Bayesian statistics is given in appendix A, while a full and exhaustive treatise can be found in [97]). For each generated source j, a normalization factor N_j is extracted from the fit, and is used to scale the corresponding MC spectrum to reconstruct its contribution to the experimental data. Indeed, N_j relates the number $\langle C_i^{\text{meas}} \rangle$ of expected counts in the i-th bin of the observed spectrum to the number $\langle C_i^{\text{MC}} \rangle$ of expected counts in the i-th bin of the simulated spectrum through the following expression:

$$\langle C_{i,\alpha}^{\text{meas}} \rangle = \sum_j N_j \langle C_{ij,\alpha}^{\text{MC}} \rangle \tag{4.1}$$

where α = M1, M2, M2sum and j runs over the number of simulated sources.

As it will be illustrated later in this section, the activity of the contaminants and the half life of processes are extracted from the N_j coefficients. In particular, one of the simulations included in the Background Model is the $2\nu\beta\beta$ decay of ^{130}Te, and from this fit CUORE was able to obtain what is today the most precise measurement of its half life. This important achievement will be shown in chapter 5, which is dedicated to the discussion of the latest CUORE results.

The software used for the combined Bayesian fit is Just Another Gibbs Sampler (JAGS) [98]. This tool performs a Markov Chain Monte Carlo (MCMC) to sample from the joint posterior of the parameters, which is proportional to the product of the Likelihood and prior functions according to the Bayes Theorem. An overview of the MCMC method in

Bayesian analysis can be found in app. A.1. The Likelihood function of the fit model is given by the product of Poissonian probabilities of observing C_i^{meas} and C_i^{MC} counts in the i-th bin of the measured and the simulated spectra respectively, while expecting $\langle C_i^{\text{meas}}\rangle$ and $\langle C_i^{\text{MC}}\rangle$:

$$\mathcal{L} = \prod_{i,\alpha} \text{Pois}(C_{i,\alpha}^{\text{meas}}|\langle C_{i,\alpha}^{\text{meas}}\rangle) \prod_{j} \text{Pois}(C_{ij,\alpha}^{\text{MC}}|\langle C_{ij,\alpha}^{\text{MC}}\rangle) \tag{4.2}$$

where the same notation of eq. 4.1 is used. The expected number of counts $\langle C_{ij,\alpha}^{\text{MC}}\rangle$ of the simulated spectra is implemented in the model as an additional free parameter for each bin i, source j and multiplicity spectrum α, assuming that the number of counts $C_{ij,\alpha}^{\text{MC}}$ is distributed according to a Poissonian with mean value $\langle C_{ij,\alpha}^{\text{MC}}\rangle$. These are then estimated from the fit of the simulations on the data, together with the normalization coefficients N_j.

Being the N_j and the $\langle C_{ij,\alpha}^{\text{MC}}\rangle$ independent variables, the prior probability of this model is given by the product of the priors of all the simulated background sources. For what concerns the normalization coefficients, when activity measurements are available, a Gaussian prior with mean equal to the measured value and width given by the associated uncertainty is used. In particular, for the cosmic muons, a Gaussian prior can be extracted from the information provided by the M>5 spectra, where their contribution is dominant. For all the other sources no measurements are available, thus uniform PDFs from 0 to a value higher than the maximum activity compatible with the CUORE data are chosen as priors, in order to prevent from any bias. Uniform non-informative priors are also adopted for the $\langle C_{ij,\alpha}^{\text{MC}}\rangle$ parameters.

The fit result is obtained by extracting the estimators of the normalization coefficients N_j from the respective marginalized posterior distributions. In case of undetermined contamination, i.e. of measurements compatible with 0, a 90% upper limit can be computed, otherwise the source activity and its statistical uncertainty is calculated. Given a background source j, the number of decays N_{meas} observed from the measured data is related to the number of simulated decays N_{MC} through the normalization coefficient N_j, similarly to the 4.1:

$$N_{\text{meas}} = N_j \cdot N_{MC} \tag{4.3}$$

If the finite detection efficiency $\epsilon < 1$ is considered, the number of observed decays is given by $N_{\text{meas}} = N_{\text{decays}} \cdot \epsilon$, being N_{decays} the actual number of nuclear disintegrations occurred during the measurement live time Δt. It is then possible to obtain the activity A_j of the j-th source, in units of Bq, as a function of the parameter N_j extracted from the fit and the (known) number of simulated decays N_{MC}:

$$A_j = -\frac{dN(t)}{dt} = \frac{N_{\text{decays}}}{\Delta t} = \frac{N_j \cdot N_{MC}}{\epsilon \cdot \Delta t} \tag{4.4}$$

where $N(t)$ is the exponential decay law, and the approximation that the experimental time scale is much shorter than the process lifetime ($\Delta t \ll \tau$) is considered. The half life is then computed by inverting the following relation:

$$N_{decays} = \frac{N_j \cdot N_{MC}}{\epsilon} \approx N_{nuclei} \frac{ln2}{T_{1/2}} \Delta t \tag{4.5}$$

where N_{nuclei} is the number of nuclei of the source j at the beginning of the measurement (t=0).

The BM fit for the three used spectra M1, M2 and M2sum is shown in fig. 4.2: the contributions from the various sources are reconstructed with a global reduced chi square of χ^2/d.o.f. = 681/365 = 1.87. The three plots show that the fit provides a faithful reconstruction of the measured spectrum in the γ region, especially between 1-2 MeV. However, minor disagreements between the data and the simulations are visible: these are likely ascribed to some inaccuracy in the model related to the sources location and distribution in the various parts of the detector. In addition, it can be noticed that the α region of the spectrum is not included in the BM fit, which is performed over the range 350 keV - 2.8 MeV. The reason for this is that, as it will be discussed in the next section, the reconstruction of the α region is complicated by several issues, like the non-ideal behavior of the detector response and the surface contamination profile modelling, which is particularly challenging[89].

These aspects of the Background Model can be improved with a more accurate study of the CUORE measured data. The α region disagreements can be reduced with a more detailed knowledge on the identified background sources, such as their positions in the detector as well as other important information like the determination of possible breaking points in the radioactive chains. The results of this analysis would provide new inputs to the BM: the fit quality would be improved, and a more precise interpretation of the measured data could be obtained.

During my PhD activity, I took part to the CUORE Background Model working group, a team of few people aimed at this task. In this framework, my personal contribution was focused on the study of the α region of the energy spectrum: the following sections are dedicated to the description of this work.

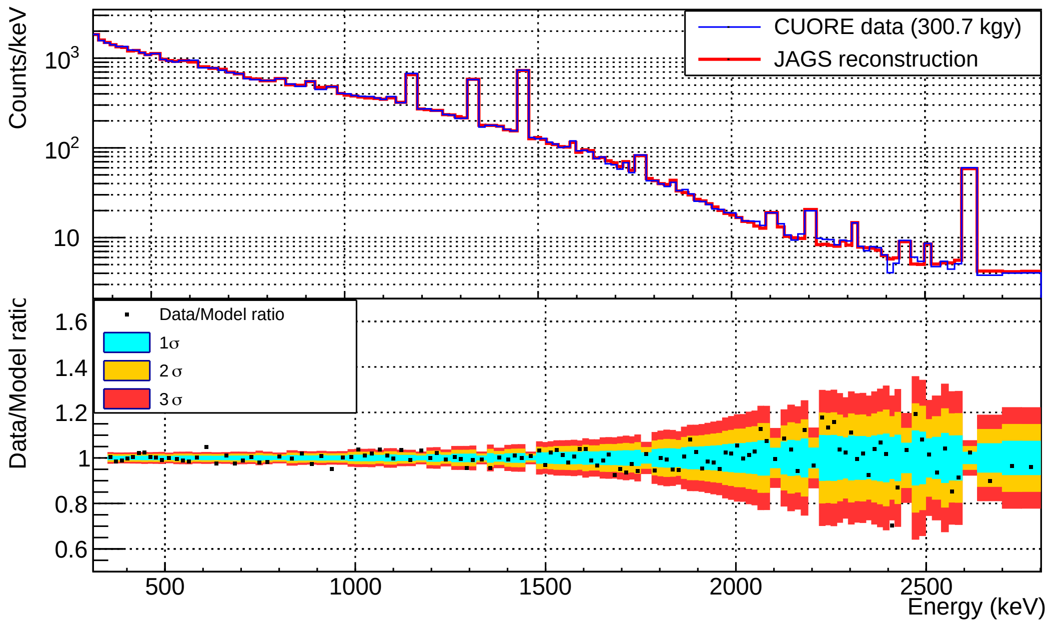
CUORE data (300.7 kgy)
JAGS reconstruction
Counts/keV
10^3
10^2
10
Data/Model ratio
1σ
2σ
3σ
Data/Model ratic
1.6
1.4
1.2
1
0.8
0.6
500
1000
1500
2000
2500
Energy (keV)

(a)

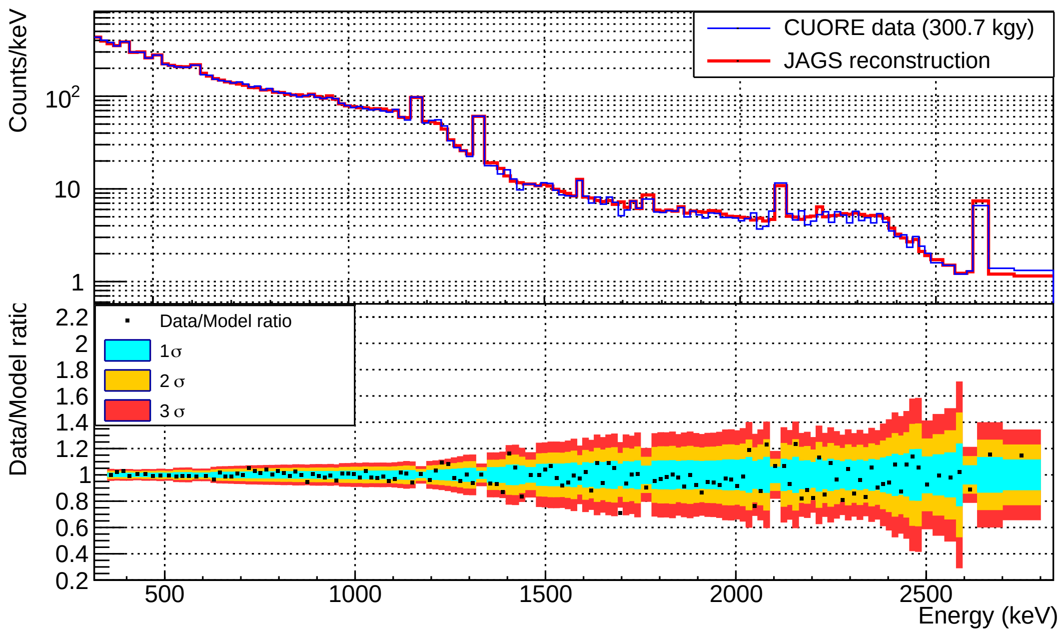
CUORE data (300.7 kgy)
JAGS reconstruction
Counts/keV
10^2
10
1
Data/Model ratio
1σ
2σ
3σ
Data/Model ratic
2.2
2
1.8
1.6
1.4
1.2
1
0.8
0.6
0.4
0.2
500
1000
1500
2000
2500
Energy (keV)

(b)

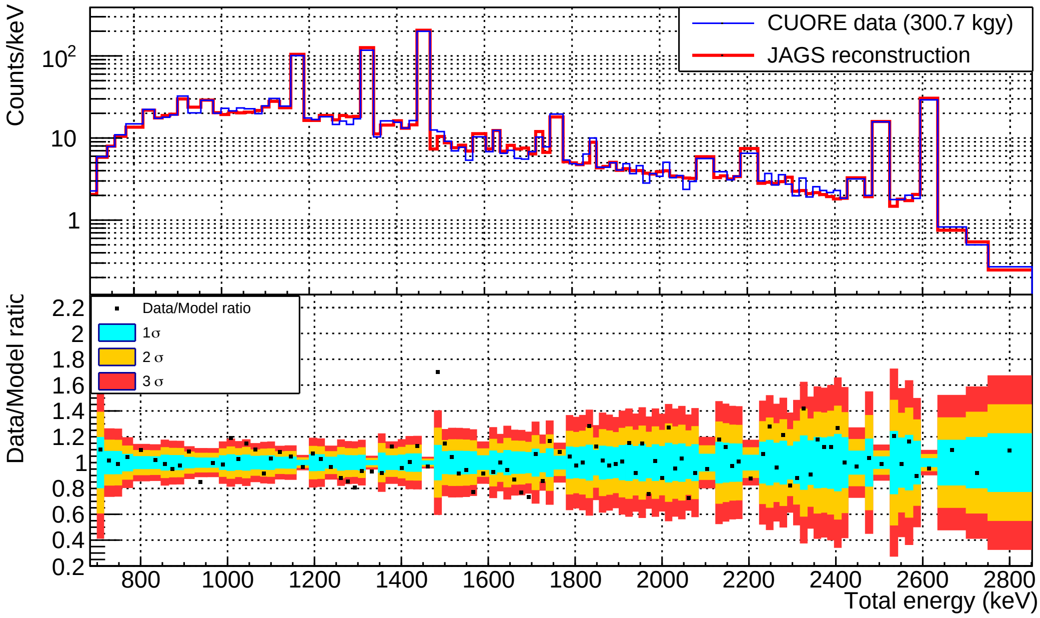

(c)

FIG. 4.2: Results of Background Model fit: (a) refers to M1 events, (b) to M2 events, (c) to M2sum. At the top of each figure, the blue line represents the measured data, while the red one is the BM reconstructed spectrum. At the bottom of each figure, the residuals with 1σ, 2σ and 3σ error bars are shown. The point with $>3\sigma$ residual in (c) refers to the bin contiguous to that of the γ peak from ^{40}K: a possible explanation to this is that it might contain counts due to the ^{40}K decay as an effect of the detector response function, and thus it should be merged with the previous bin. Figure taken from [96].

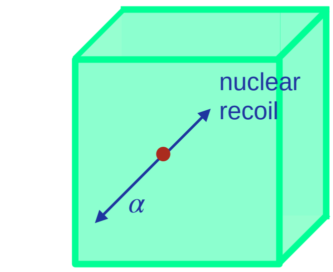

(a) Bulk contaminant. M1: $E_{meas} = Q_{value}$

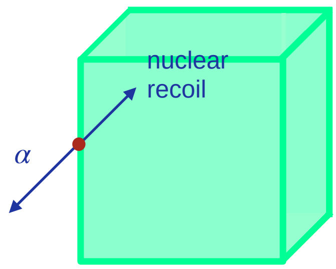

(b) Surface contaminant. M1: $E_{meas} = E_{recoil}$

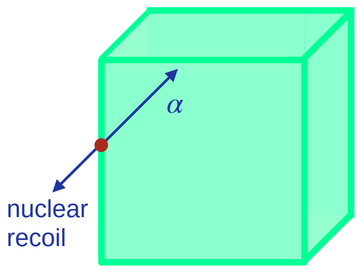

(c) Surface contaminant. M1: $E_{meas} = E_{\alpha}$

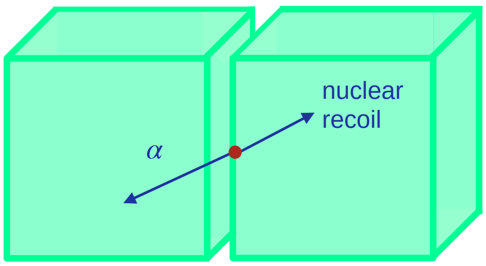

(d) Surface contaminant.
M2 single energy: $E^{(1)}_{meas} = E_{\alpha}$, $E^{(2)}_{meas} = E_{recoil}$
M2 total energy: $E_{meas} = Q_{value}$

FIG. 4.3: A schematic representation of the signatures originated by crystals contamination. (a) The source is located in the detector bulk, and a peak corresponding to the Q_{value} shows up in M1 spectrum. (b)-(c)-(d) The source is located on the crystal surface: when the escaping particle is not absorbed by another detector, M1 events are produced and a peak at E_{recoil} (b) or at E_{α} (c) is generated. When the escaping particle is detected by a neighbouring crystal, M2 events are originated (d), resulting in two peaks corresponding to E_{recoil} and E_{α} in M2 single energy spectrum and a peak at Q_{value} in M2sum spectrum.

4.3 Alpha region of the CUORE spectrum

The energy spectrum above the ^{208}Tl γ line at 2615 keV is referred to as α *region* , since it is mainly populated by alpha decay events. Just as it was observed in CUORE-0[90], the main responsible for the measured α lines in CUORE are the isotopes belonging to the naturally occurring radioactive chains of ^{232}Th and ^{238}U, and the ^{190}Pt present in the crystal bulk due to a contamination occurred during their growth process.

Alpha particles propagating through matter travel a very short distance (a 5 MeV α has a range of 10 μm in copper), hence their contribution to the spectrum can be observed only if the emitting isotope is located into/on the crystals or in their immediate proximity, e.g. on the surfaces of the copper inner shielding, the copper tower structures and the PTFE holders. The study of the event coincidences in CUORE is particularly useful to determine the contaminant location in the detector: indeed, bulk or surface contamination are characterized by different signatures in terms of deposited energy and event multiplicity. In this respect, it is worth to remind that the Q_{value} of an alpha decay is determined by the energy E_{α} of the emitted alpha particle plus ~70-150 keV carried by the recoiling nucleus (E_{recoil}). These two contributions can be partially or fully deposited into the same crystal, into a neighbouring crystal or only one of the two can be detected, depending on the contamination position. The possible resulting scenarios are then described in the following:

- **Crystal bulk** - if the contaminant is located in the bulk of the crystal, both the energy of the emitted α and that carried by the recoiling nucleus are fully absorbed by the same bolometer (fig. 4.3-a). This originates a peak centered at $Q_{value} = E_\alpha + E_{recoil}$ in the M1 spectrum, and the peak shape is expected to differ from a Gaussian distribution only consequently to the detector response function;

- **Crystal surface** - when the emitting isotope is positioned on the crystal surface, three different scenarios can arise. In case of external detectors facing the inner parts of the cryostat, the α might escape the crystal and be absorbed by the copper shield. In this situation, only the recoil energy is deposited in the detector (fig. 4.3-b), and a peak centered at E_{recoil} appears in the M1 spectrum. If the contamination is very close to the crystal surface, with a depth of few nm, it can happen that the recoiling nucleus escapes the crystal and only the α particle is absorbed (fig. 4.3-c), giving rise to a peak centered at E_α in the M1 spectrum. When the escaping particle is instead absorbed by a neighbouring crystal, the two coincident energy depositions of E_α and E_{recoil} (fig. 4.3-d) generate a M2 event whose total energy corresponds to the decay Q value: depending on the depth, this scenario is characterized by two peaks centered at the energies of the alpha and recoil respectively in the M2 single energy spectrum, and a single peak at the Q_{value} in the M2sum spectrum. The peak shape in case of surface contamination is very sensitive to the contamination depth: this determines the amount of energy that the escaping particle deposits in the crystal where the source is located before leaving it, and this causes a low or high energy tail for α and recoil peaks becoming more pronounced as the contamination is deeper. A further description of this effect is given in section 4.3.1;

- **Holder surface** - if the contamination is located on the surface of the copper close to the detectors or of the PTFE holders, only the particle escaping from the emitting material can reach a detector and produce a M1 event, and can deposit an amount of energy at most equal to E_α. Again, in this situation the depth of the contaminant plays a crucial role on the shape of the distribution contributing to the spectrum: the information corresponding to the energy deposited into the passive material is lost, thus a low depth contamination generates a peak characterized by a low energy tail, while a deep one can originate a continuous contribution with no distinguishable structures (degraded alphas). The latter case represents a particularly critical source of background, since a sizable fraction of this events reaches the ^{130}Te $0\nu\beta\beta$ ROI and cannot be rejected in case of calorimetric detectors only.

In light of these considerations, information on the sources position can be gathered by observing their contributions to the M1, M2 and M2sum superimposed spectra of the

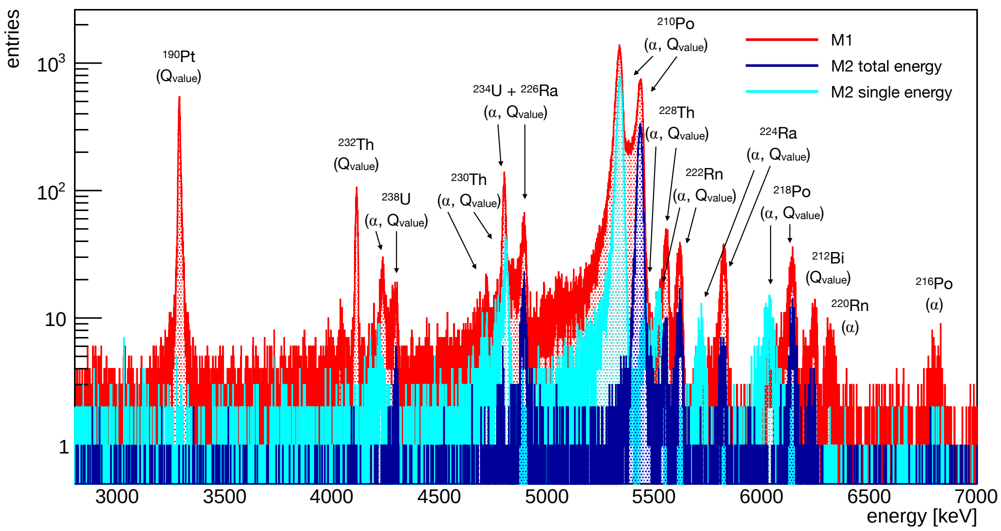

FIG. 4.4: CUORE α region in multiplicity 1 (red), multiplicity 2 single energy (cyan) and multiplicity 2 total energy (blue) spectra. The study of the α and Q_{value} lines contributing to these spectra allows to distinguish among surface and bulk contaminants. The identified radioactive sources are indicated.

CUORE α region (figure 4.4). The activities of the identified contaminants will be discussed in section 4.3.2.

^{190}Pt

Among the naturally occurring platinum isotopes, the long-lived ^{190}Pt has a low abundance of 0.01%. This nucleus decays to its ground state with an half life of 6.5×10^{11} y by emitting an α particle at 3180 keV, and the Q_{value} of this process is 3249 keV. Its presence is revealed in CUORE by the unique Q_{value} line showing up in M1 spectrum: the fact that this is the only visible contribution and that no presence of the α peak is observed even in M2 clearly indicates that this contaminant is located in the crystals bulk. The presence of ^{190}Pt in TeO_2 crystals was already observed in CUORE predecessors[99][94], and it is likely due to a contamination occurred during the crystals growth process, which takes place in platinum crucibles.

^{238}U chain

Contributions from several α lines emitted in the ^{238}U radioactive chain are visible in CUORE. For ^{238}U, the 4198 keV α peak appears both in M1 and in M2 single energy spectra, and the 4270 keV Q_{value} line is present in M1 and in M2sum: this indicates the presence of this contamination both in the crystals bulk and on their surface, and possibly on the holders surfaces as well. Coherently with this, all the other α emitters of the chain that will be mentioned in the following reveal their presence on surfaces and crystals bulk with both α and Q_{value} lines in M1 and M2. ^{234}U and ^{226}Ra lines are present, but their individual contributions cannot be easily distinguished since they are very close in energy: the two nuclei emit an α at 4774.6 keV and 4784.3 keV respectively, with Q_{value} at 4858.5 keV and 4870.6 keV. ^{230}Th 4687 keV single α and 4770 keV Q_{value} peaks are detected as well. ^{222}Rn α contribution at 5489.5 keV is partially covered by the ^{228}Th 5520.12 keV Q_{value} line in M1, but it is instead well distinguishable in M2 single energy spectrum; the respective Q_{value} at 5590.3 keV is also visible. The spectra also show the contributions by the 6002.35 keV α and the 6114.68 keV Q_{value} peaks from ^{218}Po. Finally, the most prominent lines dominating the three M1, M2 and M2sum spectra are the 5305.38 keV α and the 5407.46 keV Q_{value} peaks due to ^{210}Po decay, which can be due to a ^{210}Pb or to a ^{210}Po out of equilibrium contamination. Both hypotheses are possible. It will be shown in sec. 4.3.2 that the activity of this source is considerably higher than that of the other mentioned nuclei of ^{238}U chain. It is worth to notice that the higher statistics available for this contaminant allows to appreciate the different shape of the α peak in M1 and M2 single energy: both are characterized by the low energy tail typical of surface contamination, but the first one is more pronounced than the second. The reason is that the single α contribution in M1 is dominated by holders surface contamination, and the enhanced low energy tail suggests that this sources are located at a larger depth with respect to those on the crystal surface.

^{232}Th chain

Signals due to ^{232}Th contamination and elements belonging to its decay chain are also present in the CUORE α spectra. This time, only lines from few isotopes belonging to the chain are visible: the main reason is that the remaining ones are characterized by very short half lives of few seconds or fractions of seconds, and this causes pile-up events that are rejected by the PSA cuts performed during the data processing.

The ^{232}Th nucleus only generates the 4082.8 keV Q_{value} peak in the M1 spectrum. This signature implies that the dominant contribution from this source comes from the TeO_2 crystals bulk, while a negligible amount must be present on the crystals and holders surfaces, since no signals from the 4012.3 keV α are detected in M1 and M2. On the contrary, a surface contribution is visible for both ^{228}Th and ^{224}Ra: the respective 5423.15 keV and 5685.37 keV α lines are present in the M1 and M2 single energy spectra, as well as the two 5520.12 keV and 5788.87 keV Q_{value} peaks in M1 and M2sum. The presence of these lines suggests that a breaking point of the chain is likely after ^{232}Th decay. The situation is similar for ^{212}Bi: the 6207.14 keV Q_{value} line in M1 points at a dominant contribution from crystals bulk contamination, but also a minor surface activity is indicated by the presence of the same Q_{value} peak in M2sum spectrum. Its 6050.78 keV α line is not appreciated in M1 nor in M2. However, the ^{212}Bi branching ratio to α decay is only 35.9%, thus a lower contribution to the spectra was expected. ^{220}Rn and ^{216}Po are characterized by half lives of 55.6 s and 145 ms respectively: the majority of events from their α decays are rejected by PSA cuts, since they are too close in time and hence produce pile-up. Nevertheless, a non-negligible fraction of these events populate the M1 spectrum with the 6288.08 keV and the 6778.3 keV α lines from ^{220}Rn and ^{216}Po respectively. This can be explained with the fact that the majority of the rejected pile-up events originates from crystal surface contamination, where the α particles emitted by ^{216}Po and ^{220}Rn are absorbed by the same crystal; this is not the case for sources located on the holders surface, where the two alphas, emitted in different directions, can be detected by different crystals.

4.3.1 Quenching factor

Past studies on TeO_2 crystals reported a discrepancy between the detector response to α particles and to electrons of the same energy[100][101][102][94]. In particular, it was observed that an α energy release gives rise to a signal amplitude that is slightly higher than expected from calibration with γ lines; as a result, the reconstructed α peaks position in the spectrum is shifted towards higher energies with respect to the nominal value. The same effect is visible in CUORE as well (fig. 4.5).

Dedicated measurements[102] demonstrated that this phenomenon is not to be ascribed to a miscalibration effect. Indeed, this is also observed on the ^{147}Sm α line at 2310 keV, which is included in the energy region where the γ calibration is interpolated; thus, its origin is attributed to a different behavior of the detector when different particles release their energy. A detailed understanding of the detector response to all the interacting particle types is crucial for a better interpretation of the observed data and for the development of background rejection techniques. The just mentioned effect induced by α particles has not been fully explained yet; in this section, the positions in energy of the main α lines contributing to the observed spectrum will be studied, with the aim of quantifying this phenomenon in CUORE and to include the appropriate correction in the MC simulations.

As already explained in sec. 3.4.2, a multi-gamma source is used in CUORE to perform the energy calibration. This type of source allows to measure the so-called *electron-equivalent energy*: for a particle generating a signal, this corresponds to the amplitude of the pulse produced by an electron depositing a given amount of energy. In order to quantify the observed shift, a quantity called *Quenching Factor* (QF) is then defined as the ratio between the measured electron-equivalent energy $\mathrm{E_{meas}}$, and the nominal energy $\mathrm{E_{nom}}$ with which the α particle is emitted:

$$\mathrm{QF} = \frac{\mathrm{E_{meas}}}{\mathrm{E_{nom}}} \tag{4.6}$$

The QF in thermal detectors should result close to unity, since all the deposited energy is expected to be converted into heat.

One of the main complications of the QF study regards the precise determination of $\mathrm{E_{meas}}$, or, in other words, of the peak position in energy. As mentioned in the previous section, this is particularly difficult in case of surface contamination due to the lack of a reliable model to describe the peak shape, which is affected by the unknown contamination depth profile. To estimate the α lines positions in this work, the peaks were found to be fitted reasonably well with a combination of two *Crystal Ball* functions, from which the

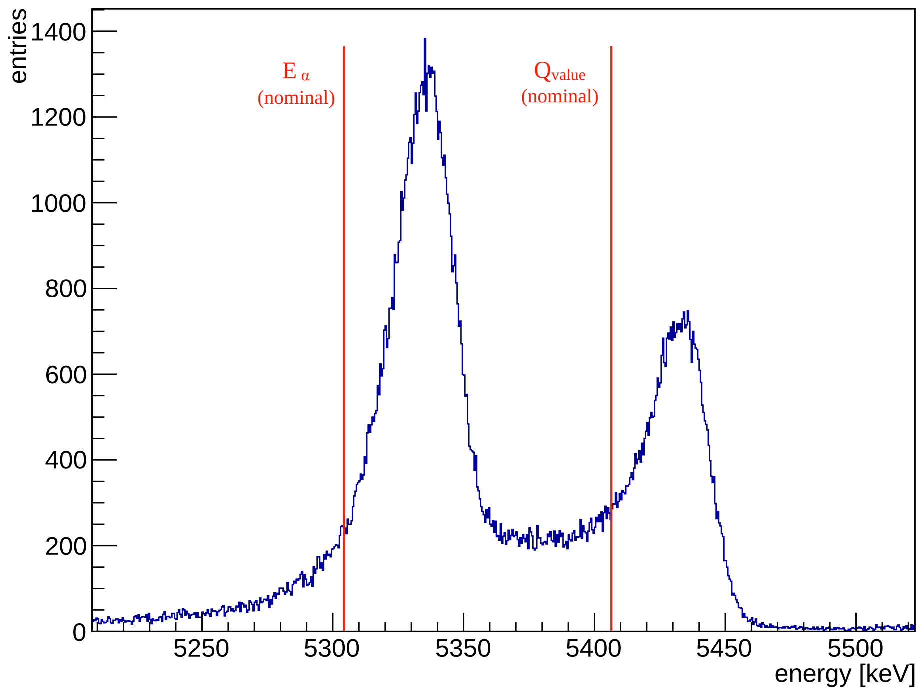

FIG. 4.5: Single α and Q_{value} lines due to ^{210}Po in M1 + M2 single energy spectrum for all the CUORE bolometers. The two peaks are expected to be centered at their nominal values of 5304 keV and 5407 keV respectively, while a $\sim$ 1% shift towards higher energies is observed.

E_{meas} parameter was extracted as follows. The Crystal Ball function [86] is often used to describe processes characterized by a defective measurement of the deposited energy, thus it can be suitable to model the surface effect of an α particle depositing a fraction of its energy before being detected. This function consists of a Gauss distribution characterized by a mean $\bar{x}$ and a standard deviation σ with a n power law tail smoothly joined to the gaussian at $\bar{x} - \alpha\sigma$, being n and α tail shape parameters:

$$f(x;\alpha,n,\bar{x},\sigma) = \begin{cases} e^{-\frac{(x-\bar{x})^2}{2\sigma^2}}, & \text{for } x > \bar{x} - \alpha\sigma \\ A \cdot \left(B - \frac{x-\bar{x}}{\sigma}\right)^{-n}, & \text{for } x \leq \bar{x} - \alpha\sigma \end{cases} \tag{4.7}$$

where $A = \left(\frac{n}{|\alpha|}\right)^n \cdot e^{-\frac{|\alpha|^2}{2}}$ and $B = \frac{n}{|\alpha|} - |\alpha|$. The sign of the α parameter determines if the tail is on the left ($\alpha > 0$) or on the right ($\alpha < 0$) of the gaussian mean. At first, the α lines were fitted with a single Crystal Ball: the fit resulted to well model the low-energy tail, but the gaussian shape was not properly describing the right side of the peak. The presence of a less pronounced high-energy tail can be explained by two distinct contributions. In case of Q_{value} peaks, the tail is due to the intrinsic CUORE non-gaussian detector response function, which will be discussed in sec. 5.1.2. For single α peaks this effect is combined with a second one: if the surface contaminant has very small depth ($\leq$ few nm) and the α particle is emitted towards the bulk, the detector can record its full energy plus a fraction of the recoiling nucleus escaping the crystal. Due to the shorter travel distance of recoiling

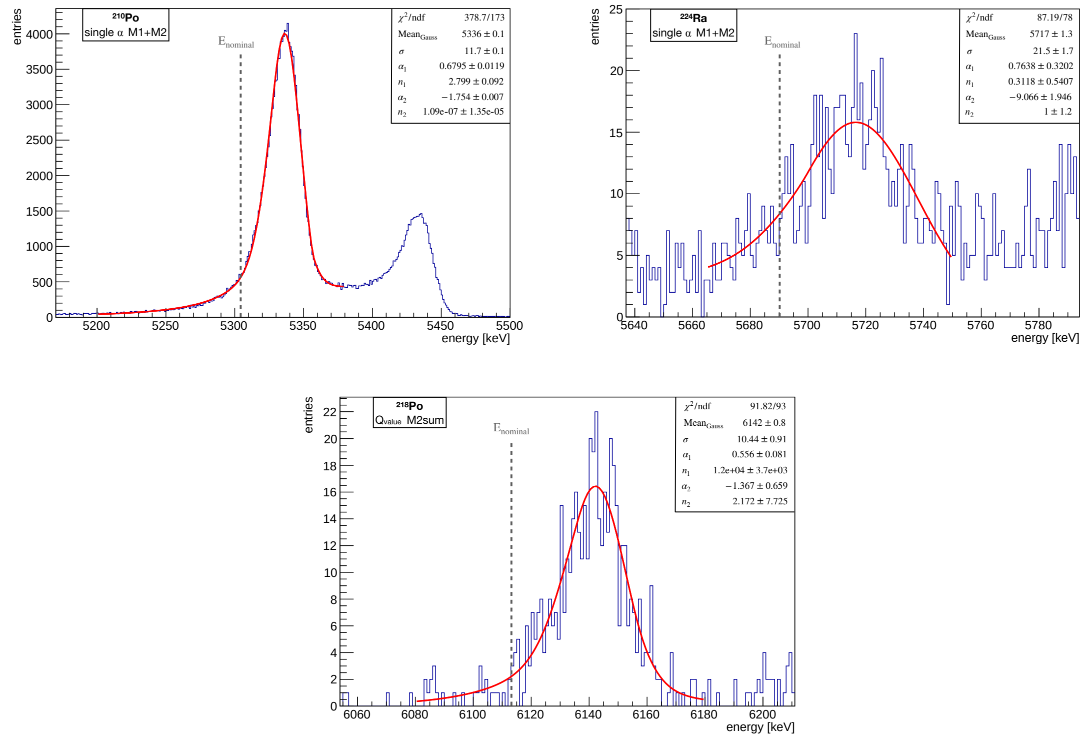

FIG. 4.6: Few examples of double Crystal Ball fits: ^{210}Po (top-left) and ^{224}Ra (top-right) single α peaks in M1+M2 spectrum, and ^{218}Po Q_{value} line in M2sum spectrum.

nuclei, this happens less frequently than an α escape, and this would explain why the right tail is less pronounced than the left one.

In light of these observations, the sum of two Crystal Ball functions sharing the gaussian parameters was chosen to fit the α and the Q_{value} lines, in order to account for both the left and the right peak tails. This model represents however an approximation, since a higher level of precision in the tails shape description is not required for the scope of this analysis. The peaks characterized by a low statistics and a poor resolution were not included in this study. The ^{190}Pt line was also excluded, since some anomalies related to its position and shape were observed in CUORE-0[94]. From the fit of each line, the gaussian mean was extracted and taken as the estimator of the peak position E_{meas}. The fits on few lines are shown in fig. 4.6 as examples, while the obtained values are summarized in table 4.7, together with the nominal energy of each peak.

The extracted values of E_{meas} were then used to compute the QF for each analyzed line according to eq. 4.6. The distribution of the obtained QFs as a function of the nominal energy is shown in the plot of fig. 4.8. The error bars are obtained from propagation of the uncertainties on E_{nom} and E_{meas}.

Results discussion

The CUORE-0 experiment reported a value of $\sim$1.007 for the α QF in TeO_2 crystals[94], and no temperature or energy dependence were observed. The results obtained in this work

Element	E_{nom} [keV]	E_{meas} [keV]
^{230}Th (Q_{value})	4770.0± 1.5	**4794.45 ± 0.84**
^{210}Po (Q_{value})	5407.46± 0.07	**5431.87 ± 0.12**
^{228}Th (Q_{value})	5520.12±0.22	**5547.96 ± 0.89**
^{222}Rn (Q_{value})	5590.3±0.3	**5616.71 ± 0.56**
^{224}Ra (Q_{value})	5788.87±0.15	**5818.7 ± 1.2**
^{218}Po (Q_{value})	6114.68±0.09	**6142.19 ± 0.76**
^{210}Po (single α)	5304.38± 0.07	**5336.32 ± 0.06**
^{224}Ra (single α)	5685.37±0.15	**5716.6 ± 1.3**
^{218}Po (single α)	6002.35± 0.09	**6031.9 ± 1.1**

TABLE 4.7: Summary of the peaks position E_{meas} extracted from the double Crystal Ball fits. The expected nominal values are also shown as reported in ref. [103].

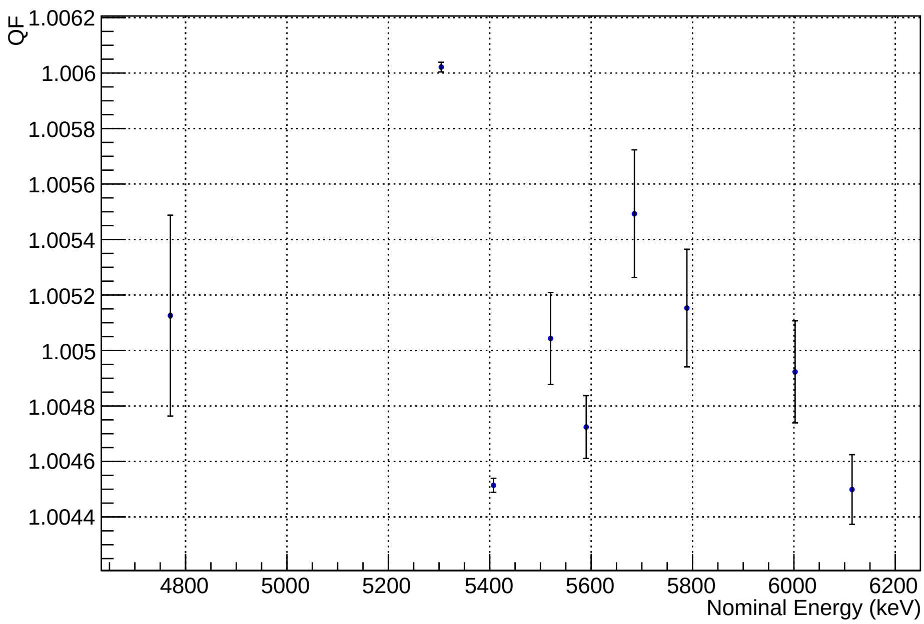

FIG. 4.8: Quenching factor as a function of the nominal energy. The QF is evaluated for each of the fitted peaks as the ratio between the extracted E_{meas} and its E_{nom}.

for CUORE point at a slightly lower value, around 1.005. However, this number is affected by several sources of uncertainty whose effects have not been quantified yet. The first that is worth to be mentioned regards the fit model and choice of the peak position estimator E_{meas}. In this study, the mean of the gaussian was taken, but another possible choice could be the distribution mode, which does not necessarily coincide with the mean. Indeed, it has been shown that the shape of the α lines is deformed due to several combined effects, and the resulting distribution is asymmetrical. A significant help towards an improvement of the fit model and in the identification of the optimal estimator would come from MC simulations of α particles in different positions and at different depths. These would provide information on the peak shape in the various scenarios, and a study on the most correct choice of the estimator could be performed for each case.

Another source of uncertainty on the peak position and shape is given by the function adopted in the calibration procedure. Indeed, the multi-gamma source used in CUORE provides a reliable calibration in the γ region, but since the highest included line is the 2615 keV γ from ^{208}Tl, the α spectrum is calibrated by extrapolation. A significant variation of the peak shape and a slight drift of its position were observed in CUORE-0 as consequences of different choices of calibration functions[104]. As already mentioned, the α quenching is not to be ascribed at miscalibration effects, but quantifying the uncertainty introduced by this systematic will be crucial to better estimate the QF.

In spite of the mentioned uncertainties, a slightly different QF in CUORE and CUORE-0 is not to be excluded. Indeed, although the same intrinsic detector response is expected as TeO_2 crystals were operated in both the experiments, different non-linearity effects can play a role. Indeed, it was observed that these non-linearities are dominated by the thermal sensor and its biasing circuit[105]: not only the NTDs bias settings were different in CUORE-0 and CUORE, but they are custom optimized for each single detector (see sec. 2.3). In addition, since the pulse shape parameters of rise and decay time result to be affected by these non-linearities, the efficiency of the PSA cut becomes lower at this energy range.

The value of the α QF currently adopted in the CUORE Background Model corresponds to the CUORE-0 measurement of 1.007. The present work indicates that a slightly smaller value could be more appropriate for CUORE; the study of the mentioned uncertainties will help in the interpretation of this result, and will likely point at the optimal QF to be included in the CUORE Background Model.

4.3.2 Secular equilibrium and break points

The evaluation of the α peaks intensity represents an effective way to constrain the activity of the isotopes belonging to the ^{232}Th and ^{238}U radioactive chains. This information is crucial for the detection of possible secular equilibrium breaking points: this represents another important information to be included in the CUORE Background Model, since it could improve both the γ and the α region reconstructions.

As described in the previous paragraph, the function adopted to fit the α lines represents an approximated model, whose purpose was the estimate of the peak position. To determine the counts contributing to each α line, a more precise model is needed to effectively disentangle the peak counts from the background. Since no reliable models are currently available, the study of the activities was performed by integrating the peaks with the method described in the following.

The time dependence of the α decay rates is evaluated over a period of 2 years: 6 datasets of variable duration, from a minimum of 24 to a maximum of 47 days, are included in this study. For each dataset, the α decay rate $\tilde{N}_{peak}$ contributing to a given peak was estimated according to this procedure:

- the peak integral N_{peak} is evaluated over an energy interval ΔE_{peak}, including the tails;

- a flat region close to the peak is chosen to estimate the background contribution to be subtracted from N_{peak}. If no structures are present at both the right and the left peak sides, the integrals N_R and N_L are computed over the energy ranges ΔE_R and ΔE_L, that are chosen as disjoint from ΔE_{peak}. The background contribution per keV is then calculated as the average between the two sides scaled by the respective integration window:
$$\bar{N}_{bkg/keV} = \frac{1}{2}\left(\frac{N_R}{\Delta E_R} + \frac{N_L}{\Delta E_L}\right) \tag{4.8}$$
If, on the contrary, a non-flat structure is present at one side of the peak, the background is evaluated on the other side only:
$$\bar{N}_{bkg/keV} = \frac{N_{R(L)}}{\Delta E_{R(L)}} \tag{4.9}$$
As an example, figure 4.9 shows the integration intervals chosen for the ^{218}Po α line in M1+M2 spectrum;

- the number of counts $\tilde{N}_{peak}$ due to the α decay is then estimated by subtracting from N_{peak} the background counts contributing to the energy window ΔE_{peak}:
$$\tilde{N}_{peak} = N_{peak} - \bar{N}_{bkg/keV} \cdot \Delta E_{peak} \tag{4.10}$$

- $\tilde{N}_{peak}$ is finally scaled by the analysis cuts efficiencies (see sec. 5.1.1) and the dataset exposure, so that the rate in units of counts/kg/day is obtained.

A Poisson uncertainty was associated to the number of counts N_{peak}, N_R and N_L evaluated by direct integration of the spectrum. These were then propagated to compute the error on $\tilde{N}_{peak}$.

For each dataset and for each studied line, $\tilde{N}_{peak}$ represents an estimate of the α decay rate evaluated from the number of counts occurred during the whole dataset; the low statistics prevents from this computation over shorter time periods. To evaluate the rate

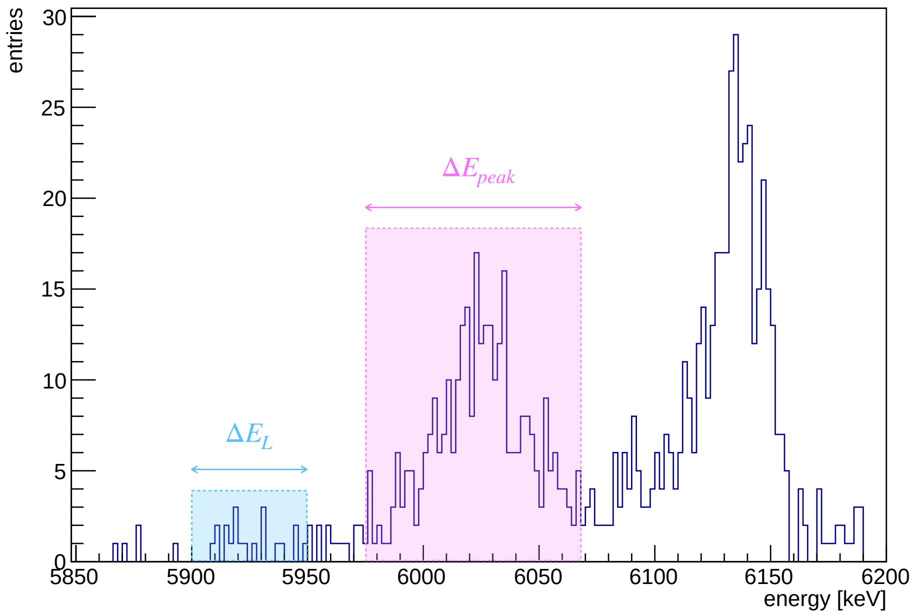

FIG. 4.9: Integration windows used to evaluate the ^{218}Po α decay counts. The background is computed over the energy range represented by the blue box, while the peak counts are obtained by integrating over the pink one. The presence of the Q_{value} prevents from evaluating the background contribution on the right side.

behavior in time for a given source, the $\tilde{N}_{peak}$ corresponding to each dataset should be associated to a time value. If the decay rate is constant over the dataset duration Δt_{ds}, any time within this period can be chosen. This is true when the decay half-life is much longer than this time interval ($T_{1/2} \gg \Delta t_{ds}$), and when the secular equilibrium condition is satisfied; as it will be shown in a while, one of these two conditions is always fulfilled for the nuclei considered in this analysis. The time at half of the dataset with an error bar corresponding to Δt_{ds} was then chosen. Such time value is computed with respect to the start time of the first dataset, taken as the reference t_0.

The described method was used to study the rate as a function of time for several nuclei, with the aim of detecting possible breaking points in the decay chains. The analysis was performed on single α lines in M1+M2 spectrum: the reason for this choice is that the coincidence efficiency in the α region of the spectrum is not determined with a reliable accuracy. The consequence of a coincidence inefficiency is that events can be assigned the wrong multiplicity, and this can happen for several reasons. For example, the existence of an energy threshold in the coincidence algorithm implies that whenever one of the two M2 events is below threshold, the other event is assigned M1. This can have critical consequences on the evaluation of the surface contamination rate, which is the subject of this study. In order to avoid possible bias related to this issue, the M1+M2 spectrum was considered.

The secular equilibrium study could not be performed for the isotopes belonging to the

^{232}Th chain since, as previously discussed, only few lines are visible. This contamination shows a minor surface contribution, such that not enough statistics is available for the evaluation of the α lines rate behavior in time. The activity of its bulk contribution could not be studied as well: among the few visible Q_{value} peaks, the counts due to the ^{228}Th line could not be estimated as it is indistinguishable from the ^{222}Rn single α, while the ^{212}Bi Q_{value} peak has a low intensity due to the 35.9% branching ratio, thus not enough statistics is available for evaluating its contribution over single datasets.

For the analysis of the ^{238}U chain secular equilibrium, the activities of ^{238}U, ^{230}Th, ^{218}Po, ^{210}Pb and ^{210}Po were determined from their rate distributions over 2 years (fig. 4.10). The α peaks of ^{234}U, ^{226}Ra and ^{222}Rn could not be included in this study: the contributions of the first two cannot be disentangled from the ^{230}Th Q_{value} line in M1, while the ^{222}Rn α peak is partially covered by the ^{228}Th Q_{value} in M1. For the long-lived nuclei ^{238}U and ^{230}Th a constant rate was expected: hence, a fit with a constant function was performed in both cases, and the obtained values were then scaled by the branching ratio of the respective α lines, namely 79% and 76.3%. The same fit was performed for ^{218}Po: this isotope is characterized by a short half-life of 3.1 minutes, therefore it is expected to contribute only as a product of the parent nuclei activity. Hence, its rate should be constant if the secular equilibrium holds. The ^{210}Po α line is the most intense of the spectrum: in addition to its production in the ^{238}U decay chain, a non-negligible quantity of this isotope is also generated as a consequence of the surface implantation of ^{210}Pb ($T_{1/2}$ = 22.3 y) due to the decay of environmental ^{222}Rn. ^{210}Po has an half-life of 138.4 days, thus its decay profile should be visible over the analyzed period: the rate obtained from the integrals of its α line was then fitted with the sum of two exponential functions describing the decay law of ^{210}Po and ^{210}Pb respectively, where the half-lives were fixed to their nominal values and the activities were the extracted parameters.

Results discussion

The activities extracted from the described fits are summarized in table 4.11. The activities of ^{230}Th, ^{238}U and ^{218}Po are very similar, suggesting that the secular equilibrium condition is fulfilled at least down to the ^{218}Po decay. As expected, the activities of ^{210}Pb and ^{210}Po are significantly higher with respect to the others, and clearly show two breaking points of the chain. It can be noticed that these two activities are also different from each other: ^{210}Po shows a factor $\sim$2 lower activity with respect to ^{210}Pb, suggesting that the secular equilibrium between the ^{210}Pb implanted on surfaces and its daughters has not been reinstated yet.

Small discrepancies are likely to be ascribed to an underestimation of the errors. In this analysis, indeed, the decay rate $\tilde{N}_{peak}$ was only assigned the uncertainty due to the propagation of the poissonian error on the counts obtained by integration, but other sources of uncertainty exist. A possible systematic can be introduced by the choice of the integration intervals used for the evaluation of the peak and background counts: the induced error can be estimated by repeating the study with different integration ranges. Another source of uncertainty is given, again, by possible miscalibration effects resulting from the extrapolation of the alpha energy region. This can bring critical consequences on the rate evaluation even if few detectors are affected by a few keV miscalibration, because a fraction of counts could fall out of the integration interval, and thus would be excluded from the counting rate evaluation. As discussed in the previous paragraph, quantifying the miscalibration contribution to the peak shift with respect to its nominal energy is very complicated, since the α quenching factor is not known with sufficient precision.

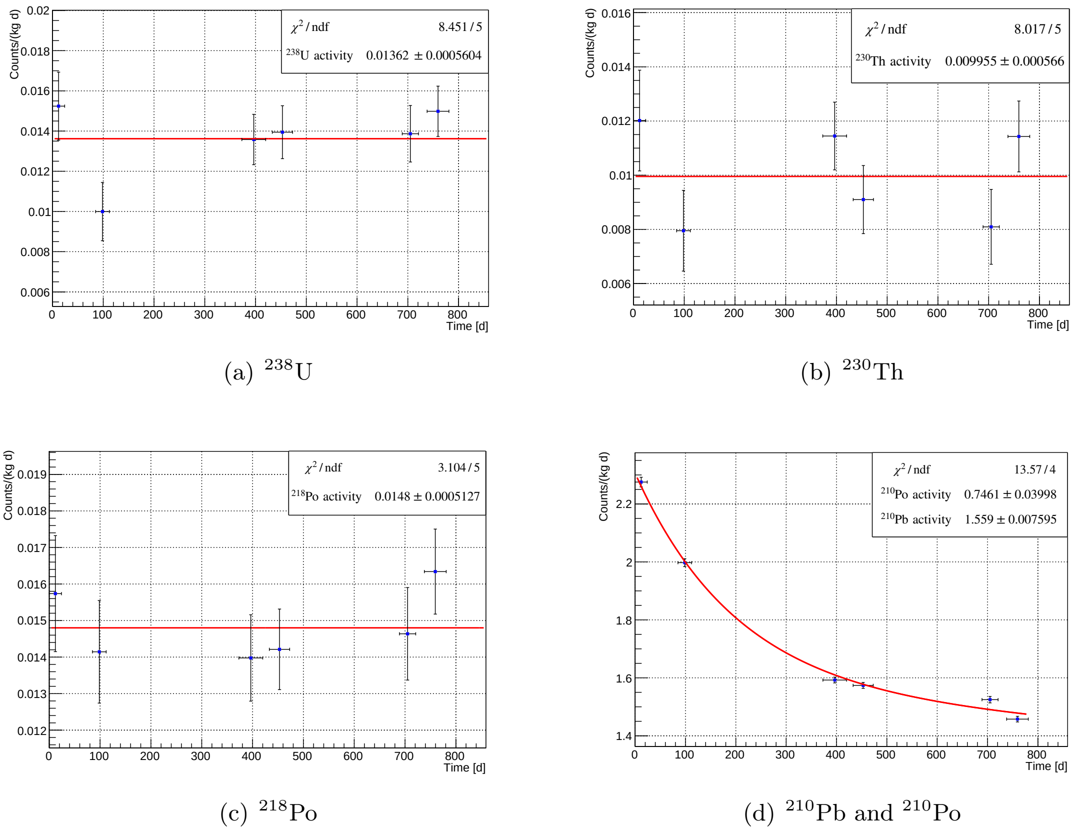

FIG. 4.10: Rate in units of counts/kg/day as a function of time for some isotopes of the ^{238}U decay chain. The ^{238}U (a), ^{230}Th (b) and ^{218}Po (c) fits were performed with a constant function, while the ^{210}Pb and ^{210}Po activities are extracted from a double exponential fit. The activities shown in the fit result boxes are not scaled by the respective decay branching ratios.

Element	Activity [10^{-2} counts/kg/day]
^{238}U	1.72 ± 0.08
^{230}Th	1.31 ± 0.08
^{218}Po	1.48 ± 0.05
^{210}Pb	155.9 ± 0.8
^{210}Po	74.6 ± 3.9

TABLE 4.11: Measured activities for some isotopes of the ^{238}U chain isotopes, properly scaled by the respective decay branching ratios. The ^{210}Pb and ^{210}Po represents two breaking points of the chain.

Chapter 5

CUORE results on ^{130}Te double beta decay

The CUORE experiment started its physics data collection in May 2017. After the first campaign, during which 2 two-months long datasets were acquired[106], the data taking was interrupted several times to perform technical runs and maintenance activities on the cryogenic system, with the aim of optimizing the operational conditions and thus improving the quality of the data. The main interventions performed in 2018 regarded a temperature scan, which led at decreasing the base temperature from 15 mK to 11.8 mK improving the signal-to-noise ratio, and an upgrade on the calibration system. In 2019, a major maintenance activity was carried out on the cryostat, to improve its stability conditions and to increase the experimental duty-cycle. These activities were concluded in March 2019, and since then a continuous and stable data taking is proceeding smoothly. Very recently, at the end of 2020, CUORE got to the milestone of 1000 kg·y of accumulated exposure.

The data collected until the end of July 2019 were used to extract the latest CUORE results, that will be presented in this chapter: section 5.1 is dedicated to the description of the main aspects of the ^{130}Te $0\nu\beta\beta$ decay search analysis and its outcome, while in section 5.2 the most precise measurement of the $2\nu\beta\beta$ decay half-life of ^{130}Te will be presented.

During the data taking of the last three datasets included in the analyses, which represent about one third of the total considered exposure, I was responsible for the online data production (sec. 3.4.2).

5.1 Search of $0\nu\beta\beta$ decay of ^{130}Te

The main goal of the CUORE experiment is the search of $0\nu\beta\beta$ decay in ^{130}Te. The result that will be presented in this section is extracted from the analysis of a TeO_2 exposure of 372.5 kg·y, corresponding to 103.6 kg·y of ^{130}Te exposure[45]. After the full reprocessing of the included datasets is completed as described in sec. 3.4.3, another step is needed before going through the $0\nu\beta\beta$ search statistical analysis. This regards the detector response characterization, which consists of computing the efficiencies (sec. 5.1.1) and extracting the detector response function (sec. 5.1.2). These information are then included in $0\nu\beta\beta$ decay search analysis (sec. 5.1.3).

5.1.1 Efficiencies

The signal efficiency computation includes several contributions that are individually evaluated. It is calculated as the product of the *containment efficiency* and the *total analysis efficiency*, which are extracted from the MC simulations and from the data respectively. The total analysis efficiency is in turn defined as the product of the *total reconstruction efficiency*, the *anti-coincidence efficiency* and the *PSA efficiency*. A brief description of each term is provided in the following.

- **Containment efficiency (ϵ_{MC})** - This is the only efficiency term extracted from MC simulations. It is defined as the probability that the energies of the two electrons emitted in a $0\nu\beta\beta$ decay are fully deposited into the same single crystal; in CUORE, this resulted to be $(88.345 \pm 0.085)\%$ for the $0\nu\beta\beta$ decay of ^{130}Te[85]. Details on its evaluation for the $0\nu\beta\beta$ decay of ^{128}Te will be given in sec. 6.1.

- **Total reconstruction efficiency** - It represents the probability that an event with a given energy is triggered, its energy is correctly reconstructed and it is not rejected as a pile-up event by the analysis cuts applied during the data processing. The PSA cut, which also contributes to the pile-up events identification and rejection, is not included in this calculation since its efficiency is evaluated separately. Heater events are used to compute the total reconstruction efficiency, taking advantage of the prior knowledge on number of injected pulses. This efficiency is given by the product of three factors, namely the *detection efficiency*, the *energy reconstruction efficiency* and the *pile-up rejection efficiency*.

- **Anti-coincidence efficiency** As just mentioned, the $0\nu\beta\beta$ decay of ^{130}Te is expected to produce single-site events with a probability of $\sim$88%, thus we choose to apply a multiplicity 1 cut to perform this analysis. The anti-coincidence efficiency refers to the probability that a single-hit event is correctly assigned to M1, or, in other words, the probability that a single-hit event is not assigned a wrong multiplicity due to a random accidental coincidence with an unrelated event. This efficiency is evaluated by selecting the signature of the ^{40}K decay via electron capture: it is indeed a suitable reference of M1 events, since it is followed by the emission of a γ line at 1460 keV that is not correlated to other events.

- **PSA efficiency** - This is the probability that events passing the base pile-up cuts also survive the PSA cut, i.e. that their M_{dist} (Mahalanobis distance, see sec. 3.4.3) is below threshold. The efficiency is calculated for multiplicity 1 and 2 separately: in the first case, M1 events with energies corresponding to fully absorbed γ rays are selected, while in the latter M2 events which energies sum at that of γ lines are taken. In the M2 case, events at different energies are sampled, and this is particularly useful to evaluate the efficiency dependence on energy. The PSA efficiency is then obtained by computing the average between the M1 and M2 efficiencies, and the difference between the two is treated in the analysis as a systematic.

The various efficiency terms are computed for each dataset. In table 5.1, the values obtained for the total analysis efficiency are summarized for each dataset.

Dataset	Total Analysis Efficiency [%]
3519	84.77 ± 0.51
3522	91.51 ± 0.39
3552	89.67 ± 0.35
3555	91.52 ± 0.34
3561	89.72 ± 0.85
3564	89.88 ± 0.46
3567	78.01 ± 0.53

TABLE 5.1: Total analysis efficiency values for each dataset included in the $0\nu\beta\beta$ decay search analysis.

5.1.2 Lineshape

It was already observed by the CUORE predecessors [107][108] that the TeO_2 bolometers exhibit a slightly non-gaussian response function. This effect is visible in CUORE as well: from the study of the 2615 keV ^{208}Tl peak, the detector response function was empirically modelled in CUORE as a combination of three gaussian distributions, characterized by the same width σ but different amplitudes and mean positions[109][110]. A primary Gaussian is taken as reference, and the amplitude and mean of the other two are defined with respect to this. The resulting function is referred to as *lineshape*, and is expressed as:

$$f(E|\mu,\sigma,A_L,A_R,m_L,m_R) = \frac{\mathcal{G}(E|\mu,\sigma) + A_L\cdot\mathcal{G}(E|m_L\cdot\mu,\sigma) + A_R\cdot\mathcal{G}(E|m_R\cdot\mu,\sigma)}{(1+A_L+A_R)} \tag{5.1}$$

where μ is the mean of the primary normalized gaussian distribution $\mathcal{G}(E|\mu,\sigma)$, while A_L, A_R and m_L, m_R are the amplitude and mean scale factors of the other two Gaussians. The six parameters $\mu, \sigma, A_L, A_R, m_L, m_R$ are extracted from a simultaneous fit of the 2615 keV γ line over all the detectors in a tower for each dataset; the fit is run on calibration data, where the high event rate provides enough statistics to perform the study on single detectors. In order to properly model the spectrum near the 2615 keV peak, other contributions are accounted for in the lineshape fit model (fig. 5.2):

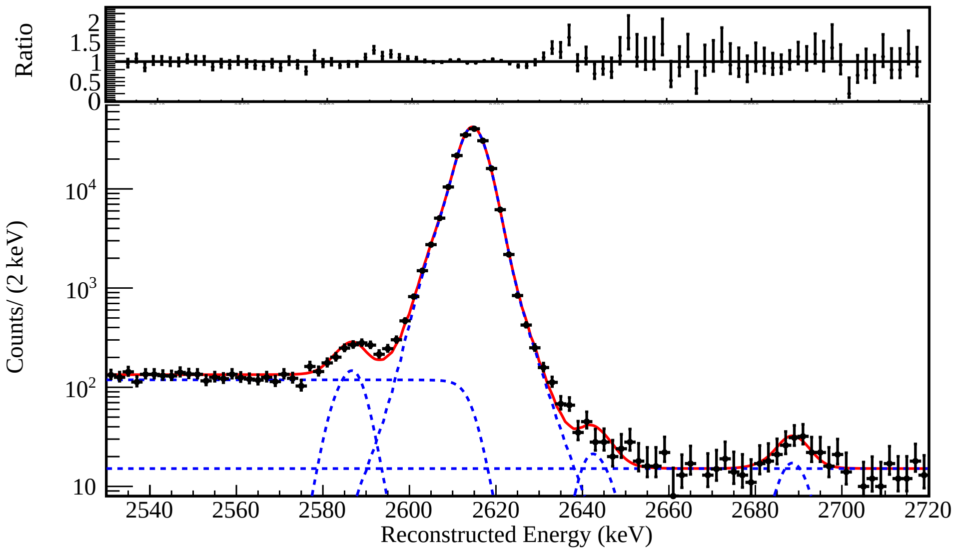

FIG. 5.2: Lineshape fit (red line) in calibration data for dataset 3522, summed over all the detectors. The blue dashed lines highlight the different contributions included in the fit model: the Compton shoulder, the flat background and, from left to right, the X-ray escape peak, the 2615 keV γ line from ^{208}Tl, the X-ray coincidence peak and the coincidence peak.

- X-ray escape peak: tellurium is characterized by multiple X-ray emissions, the most intense ones with energies of ~27-31 keV. A line ~30 keV below the photopeak is then expected;
- X-ray coincidence peak: the emission of the two γ lines at 2615 keV and 583 keV from ^{208}Tl decay can occur close in time; if the 2615 keV peak is simultaneously absorbed with an X-ray escaping from a neighbouring crystal, a line 30 keV above the photopeak is produced;
- Coincidence peak: in case of a simultaneous absorption by a crystal of the two γ lines at 2615 keV and 583 keV from ^{208}Tl, followed by a pair production with the consequent escape of a 511 keV annihilation γ, a peak at $2615 + 583 - 511 = 2687$ keV is generated;
- Compton shoulder: a continuum distribution due to the Compton scattering by 2615 keV γ rays contributes to the spectrum;
- Flat background: the contribution from degraded α particles in this region is approximated as flat background distribution.

As a result of this fit, a set of 6 parameters describing the detector response function for each bolometer-dataset pair is obtained, and important quantities such as the energy resolution in calibration can be evaluated. Due to the lack of statistics, it is not possible to extract the lineshape for each bolometer in physics data, thus the same parameters obtained from this fit are used. It was observed that, when the calibration lineshape is applied to

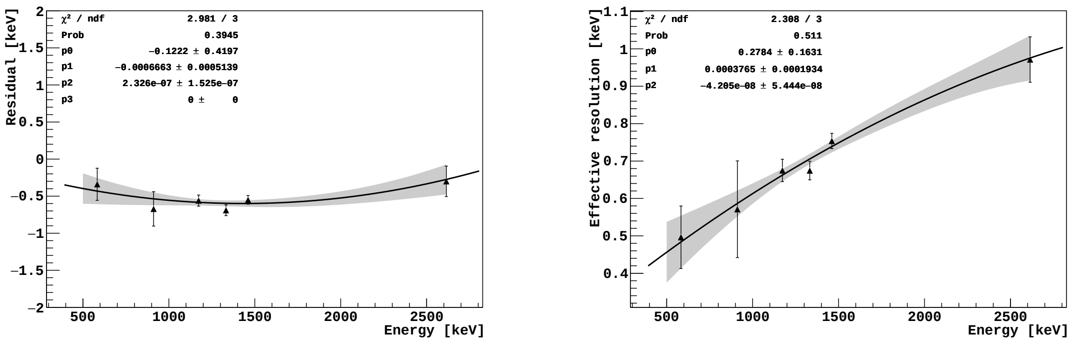

(a) (b)

FIG. 5.3: Energy reconstruction bias (a) and resolution scaling (b) as functions of energy for dataset 3564. A second order polynomial is used fit both these variables and to describe their dependence on energy.

physics data, the resolution exhibits an energy dependence, and a small bias is introduced in the energy reconstruction. In order to account for these two effects and to extract the correct resolution and energy reconstruction in physics data, the most prominent peaks of the physics spectrum are fitted for each dataset with the lineshape function of eq. 5.1, where the parameters extracted from the calibration fit are used and the Gaussian mean and width are modified the as follows:

$$\hat{\mu} = \mu_{\text{nom}} \cdot \left(\frac{\mu^{LS}_{\text{cali}}}{Q_{Tl}} \right) + \Delta\mu \qquad , \qquad \hat{\sigma} = \Delta\sigma \cdot \sigma^{LS}_{\text{cali}} \tag{5.2}$$

where μ_{nom} and Q_{Tl} are the nominal energies of the considered peak and of the ^{208}Tl line, μ^{LS}_{cali} and $\sigma^{LS}_{\text{cali}}$ are the best fit values obtained from the 2615 keV line fit in calibration, while $\Delta\mu$ and $\Delta\sigma$ are the free parameters, called *bias* and *scaling*. The bias $\Delta\mu$ represents the difference between the nominal peak position and its reconstructed energy, while the scaling $\Delta\sigma$ is a factor describing the resolution variation in energy. As a result of repeating this fit for several peaks, the parameters $\Delta\mu$ and $\Delta\sigma$ are extracted at different energies. A fit with a second order polynomial function is then performed on both the bias and the scaling values as functions of the energy (fig. 5.3); the extracted parameters are then used to extrapolate the bias and the scaling needed to correct the resolution and the reconstructed position at a the desired energy. The resolution in FWHM and the reconstruction bias at the Q$_{\beta\beta}$ of ^{130}Te $0\nu\beta\beta$ decay are summarized in table 5.4 for each dataset included in the analysis.

5.1.3 $0\nu\beta\beta$ decay results

The CUORE statistical analysis for the search of the $0\nu\beta\beta$ decay consists of an unbinned Bayesian fit over a wide region around the Q$_{\beta\beta}$, i.e. the region of interest (ROI), simultaneously performed for each detector-dataset. As it was previously mentioned, this process is expected to produce single-hit events ~88% of the times, thus the energy spec-

Dataset	FWHM at $Q_{\beta\beta}$ [keV]	Bias at $Q_{\beta\beta}$ [keV]
3519	6.05 ± 1.12	0.06 ± 0.21
3522	7.63 ± 1.16	-0.13 ± 0.21
3552	7.22 ± 0.87	-0.65 ± 0.15
3555	7.60 ± 0.92	-0.35 ± 0.16
3561	6.30 ± 1.58	-0.56 ± 0.26
3564	7.61 ± 1.01	-0.32 ± 0.18
3567	6.46 ± 0.87	-0.36 ± 0.15

TABLE 5.4: Energy resolution in FWHM and reconstruction bias obtained at the ^{130}Te $0\nu\beta\beta$ decay $Q_{\beta\beta}$.

trum for this analysis is constructed by selecting M1 events only, with energies included in the ROI. It is essential that the background structures contributing to this region are precisely identified and constrained, in order to avoid systematic effects on the reconstruction of the $0\nu\beta\beta$ decay rate, which is the parameter of interest of this statistical analysis. The CUORE ROI, corresponding to the energy range [2490, 2575] keV[1](fig. 5.5-(a)), is populated by a sum peak at 2505.7 keV due to the simultaneous absorption of 1173 keV and 1332 keV γ lines from ^{60}Co, plus a continuous flat distribution, which 90% of the events is estimated from the BM to be due to degraded alphas, while the remaining 10% are generated from Compton scattering by γ rays at 2615 keV. These contributions, together with the hypothesized $0\nu\beta\beta$ peak, are included in the fit model defined by the unbinned likelihood, which general form is expressed as in eq. B.4 and is reported here for convenience:

$$\mathscr{L}_U = \frac{\mu^n e^{-\mu}}{n!} \prod_i f(x_i) \tag{5.3}$$

It is shown in sec. B that this expression of the unbinned extended maximum likelihood can be obtained from the binned likelihood in the limit of small bin size. The $f(x_i)$ represent the probability density functions describing the data for the i-th sample; in this analysis, a $f(x_i)$ is defined for each detector-dataset pair. Both the $0\nu\beta\beta$ and the ^{60}Co sum peaks are modelled according to the lineshape function of eq. 5.1.

The fit is performed with the Bayesian Analysis Toolkit (BAT) software, whose approach will be described in sec. 6.3. The parameters of this model that are extracted from the Bayesian fit are the $0\nu\beta\beta$ decay rate $\Gamma^{0\nu}$, which is the only parameter of interest and is assumed to be not dataset dependent, a background index (BI) for each dataset in units of counts/keV/kg/y, the ^{60}Co decay rate Γ^{Co}, which is also taken as a unique parameter - provided that an exponential factor accounting for its decay is considered for each dataset -, and its position in energy μ^{Co}, that is left free to vary. All these parameters with exception of $\Gamma^{0\nu}$ represent nuisance parameters of the fit. As it will be further described in this paragraph, other parameters are later included as nuisance with the aim of studying their systematic effects. A non-informative flat prior is chosen for all the parameters.

[1]Details on the choice of this energy range as ROI can be found in [45].

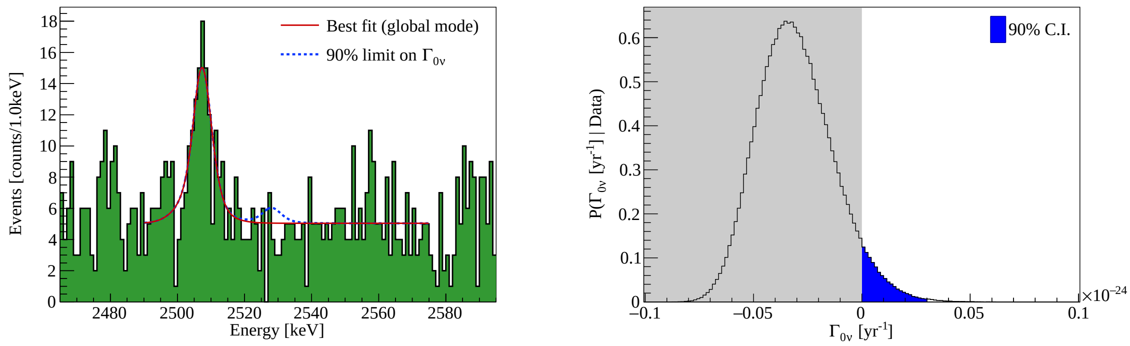

(a) (b)

FIG. 5.5: (a) CUORE energy spectrum at the ^{130}Te $0\nu\beta\beta$ decay ROI. The red line refers to the best fit curve, while in the dashed blue one represents the decay rate $\Gamma^{0\nu}$ is fixed at the 90% C.I. limit. (b) Posterior distribution of the parameter of interest $\Gamma^{0\nu}$. The blue area refers to the 90% C.I. region. Taken from [45].

No evidence of $0\nu\beta\beta$ decay is observed from the fit results. From the posterior distribution obtained for the rate $\Gamma^{0\nu}$ shown in fig. 5.5-(b), a 90% C.I. limit on the $0\nu\beta\beta$ decay of ^{130}Te can be set:

$$T^{0\nu}_{1/2} > 3.2 \times 10^{25}\ y \quad \text{(90\% C.I.)} \tag{5.4}$$

This result represents the most stringent limit on the half life of ^{130}Te $0\nu\beta\beta$ decay. When the fit is repeated without including the $0\nu\beta\beta$ peak signal component (i.e., the background-only fit), an average background index of $(1.38 \pm 0.07) \times 10^{-2}$ counts/keV/kg/y in the ROI is extracted. The background estimation is dominated by the energy regions of the ROI far from the $Q_{\beta\beta}$, therefore the BI can also be obtained from the fit model including the signal peak. We choose to repeat the fit with the background-only model because a fit with an additional component - even if this is compatible with 0 - can in principle introduce uncertainties in the background estimation. This choice ensures to avoid this possibility.

The global modes of the BI and of the ^{60}Co parameters obtained from the background-only fit are then used to generate 10^4 MC simulations of the CUORE data in the ROI, which are referred to as *toyMC* simulations. These simulations are divided in the 7 datasets taking into account the corresponding real exposure. A fit with the signal-plus-background model is then performed on each of the 10^4 toy MC, and a 90% C.I. limit on the $0\nu\beta\beta$ decay half life is extracted from each fit. The distribution of the 90% C.I. limits is then constructed; the median of such distribution is referred to as *exclusion sensitivity*. This procedure will be described in sec. 6.4.2. An exclusion sensitivity of 1.7×10^{25} y is extracted in CUORE for the studied process. From a comparison between this value and the 90% C.I. limit from the fit on data, a 3% probability of getting a more stringent limit rather than in eq. 5.4 is obtained.

In the assumption that the $0\nu\beta\beta$ decay is mediated by the exchange of a light Majorana neutrino, these results allow to set a limit on the effective Majorana neutrino mass $m_{\beta\beta}$

of 75-350 meV, according to eq. 1.19. This result is gathered by taking the phase space factor from ref.[111]. As illustrated in sec. 1.4.1, the reason why an interval is obtained for $m_{\beta\beta}$ is ascribed to the uncertainty on the nuclear matrix elements calculations.

The study of the systematic effects is performed by implementing additional nuisance parameters in the fit. Indeed, a probabilistic approach according to the Bayesian statistics can be applied on all the parameters that can affect the result on the quantity of interest[112]. The investigated systematics affect the global mode of the $\Gamma^{0\nu}$ posterior of 0.04% at most. The dominant systematic uncertainty resulted to be the error on the PSA efficiency, while minor systematic effects of 0.01-0.02% are induced by the energy resolution scaling factor and bias, the analysis and containment efficiencies, the position in energy of the $Q_{\beta\beta}$ and the natural isotopic abundance of ^{130}Te. A description of the priors chosen for the nuisance parameters in the study of the systematic uncertainties can be found in [45][112]; this will not be discussed in the following as this is out of the scope of this work.

5.2 Measurement of ^{130}Te $2\nu\beta\beta$ decay half life

The $2\nu\beta\beta$ is the double beta decay mode admitted by the Standard Model. As already explained in sec. 1.4, the two neutrinos emitted in this process carry a fraction of the transition energy and escape the detector without being absorbed; as a consequence, the energy spectrum resulting from the detection of the two emitted electrons form a continuous distribution from 0 to $Q_{\beta\beta}$. This decay represents a background for the $0\nu\beta\beta$ decay search, as its events can be smeared into the ROI due to the detector energy resolution broadening the spectrum. Studies of the $2\nu\beta\beta$ decay spectral shape and precise measurements of its half life are interesting since these provide essential inputs to test nuclear models [113][114].

The contribution of $2\nu\beta\beta$ decay of ^{130}Te to the CUORE spectrum can be disentangled from the other background sources through the BM fit described in sec. 4.2. Thanks to this analysis technique, CUORE was recently able to obtain the most precise half life measurement for this decay, with an exposure of 300.7 kg·y[96]. With respect to the data used for the $0\nu\beta\beta$ decay search, two datasets were excluded from this analysis, since several bolometers not well-performing and with calibration issues were identified, after a long campaign of data quality study performed on the whole energy spectrum. These issues, however, were found to produce no effects in the ^{130}Te $0\nu\beta\beta$ ROI, and thus could be included in that analysis.

The BM fit is performed in the energy range 350 keV - 2.8 MeV. This region of the CUORE spectrum results to be dominated by the continuous distribution due to the $2\nu\beta\beta$ decay of ^{130}Te: in particular, it is responsible for more than 50% of the events detected in the M1 spectrum between 900 keV - 2 MeV. In order to prevent from any bias, the $2\nu\beta\beta$ normalization factor resulting from the fit is kept blinded during the fit optimization procedures and the cuts tuning: in this way, the half life is expressed as a non-physical term, and its value cannot be compared to past measurements.

In order to evaluate the stability of the result, possible sources of systematic error were studied. These are summarized in the following:

- $2\nu\beta\beta$ spectral shape - two slightly different models were tested in the fit: the Single State Dominance (SSD), used as default in this analysis, and the Higher State Dominance (HSD)[113][115];

- Energy threshold - the fit was repeated with different energy ranges, varying the lower bound between 300 keV - 800 keV;

- Geometrical effects - the sources are generated as uniformly distributed in all the materials. Possible uncertainties due to this approximation were evaluated by repeating the fit on subsets of data, where the detector is split in two parts in different ways: the division in based on crystal number (even, odd, last digit 0-4, 5-9), on floor number (even, odd, first and second half) and on tower number (even, odd, first and second half);

- ^{90}Sr - the effect of the possible presence of this long-lived contamination in the crystals due to radioactive fallout was evaluated by performing the fit with and without including it in the list of the simulated sources;

- Time stability - the fit was repeated on each of the datasets included in the analysis, separately;

- Generated background sources - the reference fit is performed with 62 simulated background sources, but some contributions could not be clearly evaluated due to an insufficient statistics. The fit was then repeated after removing the sources whose contribution is compatible with 0.

In addition, the fit was tested with a uniform binning of 10 keV, 20 keV and 30 keV, and no variations were observed in the resulting value of the $2\nu\beta\beta$ decay half life. The dominant contribution to the systematic uncertainty among the investigated possibilities turned out to be the spectral shape model, which introduces an error of 1.3%. This uncertainty can be reduced with theoretical input or with further increased accumulated statistics. All the obtained systematic errors are combined in quadrature, and the resulting uncertainty is associated to the $2\nu\beta\beta$ decay half life measurement.

After the normalization factor unblinding is performed, the ^{130}Te $2\nu\beta\beta$ decay half life is extracted according to eq. 4.5, where the number N_{nuclei} of $\beta\beta$ emitters at t=0 is obtained from 1.22:

$$T_{1/2} = ln2 \cdot \eta \cdot \frac{N_a}{m_{mol}} \frac{M \Delta t}{N_{\text{decays}}} = ln2 \cdot \eta \cdot \frac{N_a}{m_{mol}} \frac{M}{A_{2\nu\beta\beta}} \tag{5.5}$$

where η is the natural abundance of the considered isotope, N_a is the Avogadro number, m_{mol} is the molar mass of TeO_2, M is the total TeO_2 mass and $A_{2\nu\beta\beta}$ is the extracted activity for the process. The obtained measurement is:

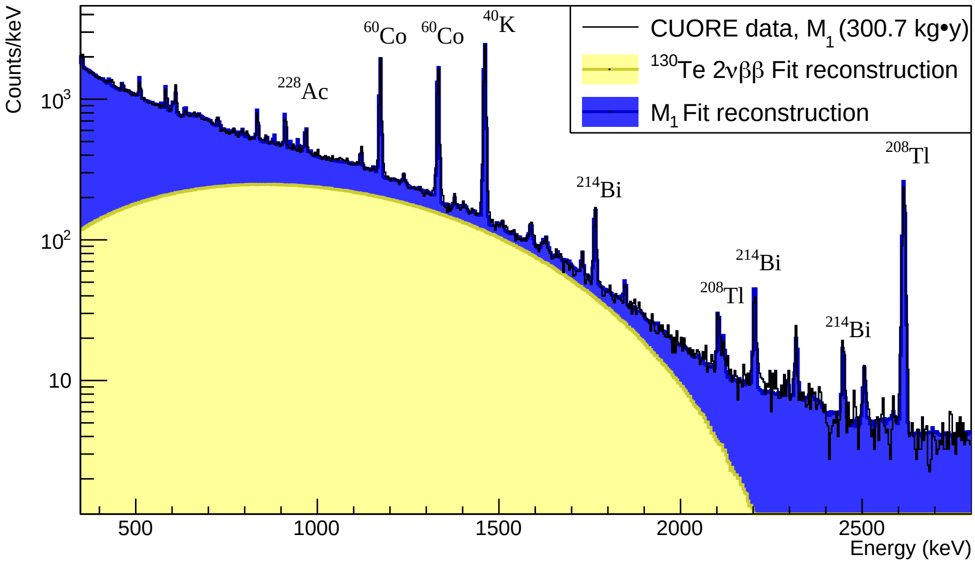

FIG. 5.6: Comparison between the M1 spectrum of measured data (black line) and the BM reconstruction (blue - filled). The yellow distribution represents the ^{130}Te $2\nu\beta\beta$ decay contribution as reconstructed by the BM fit. Taken from [96].

$$T_{1/2}^{2\nu} = 7.71^{+0.08}_{-0.06}(\text{stat.})^{+0.12}_{-0.15}(\text{syst.}) \times 10^{20} \text{ y} \tag{5.6}$$

This value is compatible with past results [44][116][90], and represents the most precise half life measurement of ^{130}Te $2\nu\beta\beta$ decay to date. Fig. 5.6 shows the M1 reconstructed spectrum compared to the measured data, and the contribution due to ^{130}Te $2\nu\beta\beta$ decay is highlighted.

Chapter 6

Search for Double Beta Decay of ^{128}Te

The observation of the $0\nu\beta\beta$ decay would demonstrate that neutrinos are Majorana particles regardless of the physics mechanism underlying this process. As mentioned in section 1.4.1, the most favoured hypothesis involves the exchange of a light Majorana neutrino, but several other extended models are theorized, and the detection of a positive signal for the $0\nu\beta\beta$ decay of a single isotope could not determine the mechanism that triggers this reaction[117]. A significant help in the discrimination of the existing models would be provided by the comparison of the $0\nu\beta\beta$ decay half lives of different isotopes: in particular, it can be shown that in the assumption that one mechanism is dominant in the generation of this decay, the ratio between different isotopes half lives depends on such mechanism, and thus could be compared with the other theoretical predictions[118]. Significant information can be obtained not only in case of two half lives measurements, but also by the comparison of one measurement and one upper limit of a different nucleus. In addition, the comparison of half life ratios represents a suitable technique to test calculations of the nuclear matrix elements (NME); indeed, it was shown that the ratio of the lifetimes is very sensitive to the different models describing the nuclear structure[119]. In the hypothesis of light Majorana neutrino exchange, the knowledge of the NME and the phase space factors is required to interpret the $0\nu\beta\beta$ decay rate in terms of the effective Majorana mass $m_{\beta\beta}$ (eq. 1.19), whose major source of uncertainty is currently represented by the disagreement among the NME calculations from different models.

Observing the $0\nu\beta\beta$ decay of different nuclei can thus shed light both on the underlying mechanism and on the correct nuclear structure model. For these reasons, a great scientific effort is put nowadays in the search of $0\nu\beta\beta$ decay of several different nuclei. As it was extensively discussed in the previous chapters, the main goal of the CUORE experiment is to probe the $0\nu\beta\beta$ decay of ^{130}Te, but thanks to its ton-scale mass and low background, another tellurium isotope candidate for the $0\nu\beta\beta$ decay can be studied: the ^{128}Te. The study of this isotope is particularly interesting, since it can provide a powerful discriminator in the theoretical model comparison from the study of the half lives ratios[118].

Together with ^{130}Te, ^{128}Te is characterized by the highest natural isotopic abundances among the nuclei that can undergo $0\nu\beta\beta$ decay (fig. 1.7): its natural abundance of 31.75%[37] makes it an attractive candidate for the search of $0\nu\beta\beta$ decay to ^{128}Xe. However, the transition energy at $Q_{\beta\beta} = (866.6 \pm 0.9)$ keV [120] lies in a highly populated region of the energy spectrum, dominated by the natural γ background due to environmental radioactivity, as it was discussed in chapter 4. For this reason, past experiments using tens of kg of TeO_2 were characterized by a poor sensitivity to this process. The latest ^{128}Te $0\nu\beta\beta$ decay half life limit from direct search experiments was set by MiDBD in 2003[44]: with an array of 20 TeO_2 crystals for a total mass of 6.8 kg and two crystals isotopically enriched in ^{128}Te at 82.3%, a limit of

$$T^{0\nu}_{1/2} > 1.1 \cdot 10^{23}\ y \tag{6.1}$$

was set for the half life of this isotope by direct measurement.

More stringent limits are instead obtained indirectly from geochemical experiments. This experimental technique consists of evaluating the presence of the $\beta\beta$ decay products which have accumulated in geological mineral samples of known age, by measuring the parent/daughter nuclei ratio. The measurements and limits extracted with this method are thus not sensitive to the $\beta\beta$ decay mode, and refer to the sum of all the possible ones ($2\nu\beta\beta$ or $0\nu\beta\beta$, to the ground state or to excited states). The most recent recommended half life value for $\beta\beta$ decay of ^{128}Te is[121]

$$T_{1/2} = (2.0 \pm 0.3) \cdot 10^{24}\ y \tag{6.2}$$

whose dominant contribution is expected to be given by the two-neutrino mode. Currently, no information about the ^{128}Te $2\nu\beta\beta$ decay is available from the CUORE Background Model, as its contribution is not included in the BM reconstruction fit. The reason is that, as mentioned in sec. 5.2, the lower energy of the present fit range is 350 keV, thus a significant fraction of $2\nu\beta\beta$ events are excluded from the analysis. By inverting eq. 1.23 and assuming the half life value in eq. 6.2, the expected number of counts from this decay in the 300.72 kg$\cdot$y exposure spectrum (as in the last BM fit) is $\sim$120; thus, just $<$100 counts contribute to the analyzed data. We are currently working to include lower energies in the BM fit, to minimize the excluded events and to add the ^{128}Te $2\nu\beta\beta$ decay component to the fit model.

The CUORE experiment operates a total TeO_2 mass of 742 kg, corresponding to 188.5 kg of ^{128}Te. With its ton-scale mass, its low background level and the unprecedented amount of accumulated exposure, CUORE can achieve a factor 10 higher sensitivity to the $0\nu\beta\beta$ decay of this isotope with respect to past direct experiments, and can aim at a very sensitive result, being competitive with the geochemical results.

This chapter is entirely dedicated to the analysis work I performed on the search of the ^{128}Te $0\nu\beta\beta$ decay during my PhD. The first required ingredient for this analysis is the *containment efficiency* of the process, namely the fraction of $0\nu\beta\beta$ events that are expected to deposit all the energy in a single crystal. The procedure I adopted for the evaluation of this quantity will be described in sec. 6.1. The second needed information regards the definition of a region of interest (ROI) of the CUORE spectrum, namely an energy window in the vicinity of the $Q_{\beta\beta}$ where the $0\nu\beta\beta$ candidate events should be searched for. An accurate knowledge of the present background contributions is necessary when choosing this region. This aspect will be discussed in sec. 6.2. The technique I then used to extract a statistical inference on the $0\nu\beta\beta$ decay signal rate consists of a binned Bayesian fit of the CUORE spectrum in the ROI where the posterior sampling is performed taking advantage of a Markov Chain Monte Carlo. From the results of the fit whose model includes both the background structures and the signal component, I extracted the limit corresponding to the 90% C.I. of the signal rate marginalized posterior. This procedure will be illustrated in detail in sec. 6.3. Before the implemented fit model could be run on the CUORE data, the fit was tested and validated on toyMC simulations of the ROI spectrum: sec. 6.4 will be dedicated to the description of these tests and their outcome. Finally, after the validation of the whole analysis procedure on the simulations, the fit could be performed on the CUORE data, and the final results of this analysis could be extracted. The main results consist of the 90% C.I. limit on the $0\nu\beta\beta$ decay half life and the extraction of the CUORE median exclusion sensitivity, the latter defined as the median of the distribution of the $T^{0\nu}_{1/2}$ 90% C.I. limits extracted from 10^4 fit on toyMC simulations of pseudo-CUORE experiments. These will be discussed in sec. 6.5.

This analysis is performed with a total exposure of 309.33 kg·y, and includes 5 datasets. The same two excluded from the ^{130}Te $2\nu\beta\beta$ decay study were excluded from this analysis as well: as mentioned in sec. 5.2, several detectors in these datasets presented calibration and performance issues at energies far from the ^{130}Te $0\nu\beta\beta$ decay ROI, including the energy region involved in the analysis described in this chapter. A fraction of bolometers presented such misbehaviors in the other datasets as well: among these, the detectors showing this issue in the alpha region of the spectrum only were included in this study, whose involved energy region is well far from the affected one.

6.1 Containment efficiency evaluation

The first step towards the selection of events that could be generated by the ^{128}Te $0\nu\beta\beta$ decay regards the identification of the signatures produced by this process. As it was discussed in section 1.5, the summed energy of the two electrons emitted in the $0\nu\beta\beta$ decay is expected to produce a sharp peak at $Q_{\beta\beta}$: a crucial aspect of this analysis consists of evaluating which fraction of these events corresponds to the two electrons fully absorbed by the same single CUORE crystal. This is the definition of *containment efficiency*.

An effective technique to extract this information consists of performing a known number N_{MC} of Monte Carlo simulations of the studied decay in the CUORE bolometers, and to evaluate the number $N_{0\nu}$ of events reconstructed at the $Q_{\beta\beta}$ peak. The containment efficiency ϵ_{MC} is then computed as the ratio:

$$\epsilon_{MC} = \frac{N_{0\nu}}{N_{MC}} \tag{6.3}$$

In order to evaluate the containment efficiency for the ^{128}Te $0\nu\beta\beta$ decay, the CUORE Monte Carlo software `qshields` (sec. 4.1.1) was used to generate $N_{MC} = 10^8$ decays uniformly distributed in the bulk of the CUORE crystals. The resulting simulations were then processed with the `g4cuore` software (sec. 4.1.2) to reproduce the detector operation details and to compute the event coincidences. As explained in sec. 3.4.3, in the coincidences calculation the events are assigned a multiplicity, a value indicating the number of crystals simultaneously involved in that interaction. From this information it is possible to determine the multiplicity distribution of the events induced by the generated $0\nu\beta\beta$ decays, and thus to evaluate the exact fraction corresponding to single crystal energy releases.

The percentage of events assigned to the various multiplicities is reported in table 6.1. For the 98.3% of the simulated $0\nu\beta\beta$ decays, the energy is deposited in a single crystal, while only for a small fraction of events 2 or more bolometers are involved. The relevant information for the containment efficiency calculation is now related to the fraction of these M1 events that are reconstructed at the $Q_{\beta\beta}$ peak: in order to evaluate it, a binned maximum likelihood fit is performed on the M1 simulated events with a model function that describes the contributions to this spectrum in the proximity of the $Q_{\beta\beta}$.

To precisely identify these contributions and define a proper model, the M1 simulated spectrum with a Gaussian smearing accounting for the detector response was compared with the same spectrum at infinite energy resolution (fig. 6.2): in this way, it was possible to disentangle close structures that would be indistinguishable otherwise. Multiple X-ray escape peaks are identified in fig. 6.2-a: starting from lower energies, the first is due to the K_{b2} shell X-rays at 31.704 keV, the second is given by the two superimposed ones from K_{b3} and K_{b1} shells at 30.944 keV and 30.995 keV respectively, and the third is related to the X-rays from K_{a2} and K_{a1} shells at 27.202 keV and 27.472 keV. These escape peaks are considered in this fit model as three Gaussian distributions. Moving closer to the $Q_{\beta\beta}$ peak, a small contribution due to escape peaks from low intensity L shell X-rays and Auger electrons with energies between 4 and 5 keV is visible; however, these are not included in the fit model, since they introduce a negligible fraction of counts with respect to those

Multiplicity	% of events
M1	98.3
M2	1.2
M>2	0.5

TABLE 6.1: ^{128}Te $0\nu\beta\beta$ decay multiplicity distribution. Most of the decays is assigned to multiplicity 1, meaning that the two emitted electrons are absorbed by the same crystal. For 1.24% of the cases, the electrons deposit their energy in two crystals, while less than 1% involve more than 2 detectors.

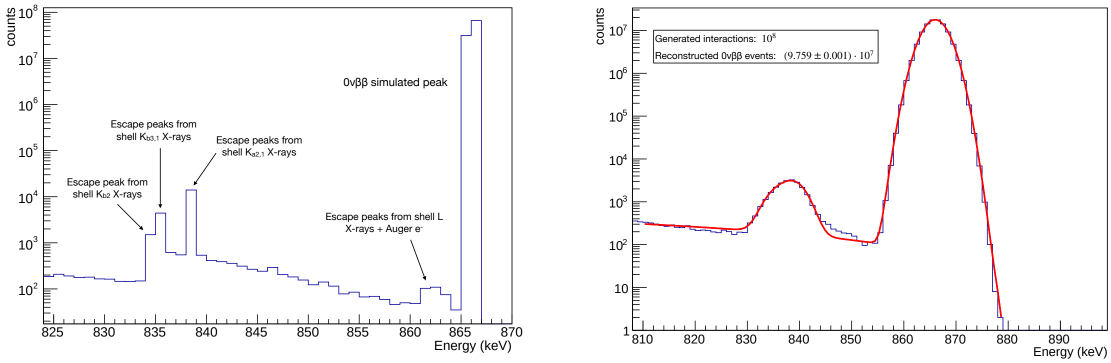

(a) (b)

FIG. 6.2: Multiplicity 1 simulated spectra of ^{128}Te $0\nu\beta\beta$ decay, at the energy region close to $Q_{\beta\beta}$. (a) With infinite energy resolution, the contributions due to the escape peaks from Te X-rays can be distinguished. (b) A Gaussian distribution smearing is applied to mimic the detector response: a binned maximum likelihood fit is performed on the spectrum with a model function including the escape peaks from the Te X-rays, the signal peak and a linear continuum contribution, to extract the number of reconstructed events at the $Q_{\beta\beta}$ peak.

of the $0\nu\beta\beta$ decay peak, and do not affect the containment efficiency calculation. The latter, dominant peak is modelled in the fit as a Gaussian distribution, and finally a linear background is adopted to approximate the end of the continuum spectrum due to the incomplete absorption of the two electrons.

The curve corresponding to the described fit is shown in fig. 6.2-b: the resulting number of $0\nu\beta\beta$ decay events reconstructed at the $Q_{\beta\beta}$ peak is $N_{0\nu} = (9.759 \pm 0.001) \cdot 10^7$. From the 6.3 and reminding that $N_{MC} = 10^8$ decays were generated, the ^{128}Te $0\nu\beta\beta$ decay containment efficiency is obtained:

$$\epsilon_{MC} = (97.59 \pm 0.01)\% \tag{6.4}$$

The other efficiency contributions considered in this analysis are evaluated as described in section 5.1.1 for the ^{130}Te $0\nu\beta\beta$ decay analysis.

6.2 Choice of the Region Of Interest

Since the M1 efficiency is ~100% (tab. 6.1), the energy spectrum for the ^{128}Te $0\nu\beta\beta$ decay search is constructed by selecting M1 events. The definition of an energy region of interest (ROI) around the $Q_{\beta\beta} = (866.6 \pm 0.9)$ keV is then required to select the fraction of events among the detected ones that might include $0\nu\beta\beta$ decay candidates. To this purpose, a correct identification of the background contributions present in the proximity of the $Q_{\beta\beta}$ is crucial to choose a ROI that allows to precisely constrain these components and avoid biases on the signal rate reconstruction.

The M1 spectrum at the energy region close to $Q_{\beta\beta}$ from the CUORE Background Model simulations is shown in figure 6.3. Multiple peaks populate this energy window.

The closest expected structure to $Q_{\beta\beta}$ is a γ line at 860.6 keV with a branching ratio (BR) of 12.4% produced by the decay of ^{208}Tl, which belongs to the ^{232}Th chain. A prominent peak at 834.8 keV due to a ^{54}Mn γ line with 99.98% BR is also identified: the presence of ^{54}Mn stems from the cosmogenic activation of copper. The visible peak at the right of $Q_{\beta\beta}$ is instead the 911.2 keV γ line with 25.8% BR from the decay of ^{228}Ac, which is another element of the ^{232}Th chain. In addition to the identified peaks, a continuous background contribution mainly induced by the $2\nu\beta\beta$ decay of ^{130}Te and by the multiple Compton scattering of the various γ rays from environmental radioactivity and cosmic radiation is observed.

The choice of the analysis ROI was then guided by the need of an energy window that fully contains the events of the hypothesized $0\nu\beta\beta$ peak, but that is large enough to also include the background structures that need to be constrained to correctly evaluate the signal rate. For the sake of simplicity, a uniform FWHM energy resolution of 5 keV is assumed in the energy window just to make the following considerations . The ROI upper edge was set to 890 keV: this energy is $> 11\sigma$ higher than $Q_{\beta\beta}$, so it ensures to fully contain events from $0\nu\beta\beta$ decay, and it is $> 9\sigma$ lower than the ^{228}Ac peak at 911.2 keV, thus providing a safe cut to exclude its contribution. The ^{208}Tl peak at 860.6 keV is too close to $Q_{\beta\beta}$ to be excluded from the ROI, thus it is included. The ^{54}Mn peak is included as well, to be sure that all the events from the left tail of the ^{208}Tl peak are selected, and thus its rate is correctly constrained. The ROI lower edge is then set to 820 keV: this is $> 6\sigma$ away from the ^{54}Mn line, providing a safe cut to fully include it.

The events analyzed for the ^{128}Te $0\nu\beta\beta$ decay search are then selected in the M1 spectrum within a ROI corresponding to [820 - 890] keV, and the background structures included in the likelihood model are the ^{54}Mn peak, the ^{208}Tl peak and the continuum distribution. The M1 spectrum represented in figure 6.3 shows that the continuum background contribution decreases from lower energies towards higher ones in the ROI. To account for this behavior, this component is modelled with a linear function. This model will be described in detail in section 6.3.1.

6.3 Statistical approach to $0\nu\beta\beta$ peak search: Bayesian Fit

The approach adopted for the analysis of the ^{128}Te $0\nu\beta\beta$ decay search consists of a Bayesian binned fit simultaneously performed on the five included datasets. Differently from the ROI of ^{130}Te, which is populated by $\sim$100 background events at the analyzed exposure, the background structures that characterize the energy region defined in sec. 6.2 contribute with a number of counts a factor 100 higher. In this framework, an unbinned fit as the one adopted for the search of ^{130}Te $0\nu\beta\beta$ signal (sec. 5.1) is not suited, since exploiting the information of each single event becomes unnecessarily heavy given the large statistics. For this reason, a binned fit represents a more appropriate choice for the of ^{128}Te $0\nu\beta\beta$ decay ROI.

As it was already mentioned in section 4.2, this statistical approach is based on the

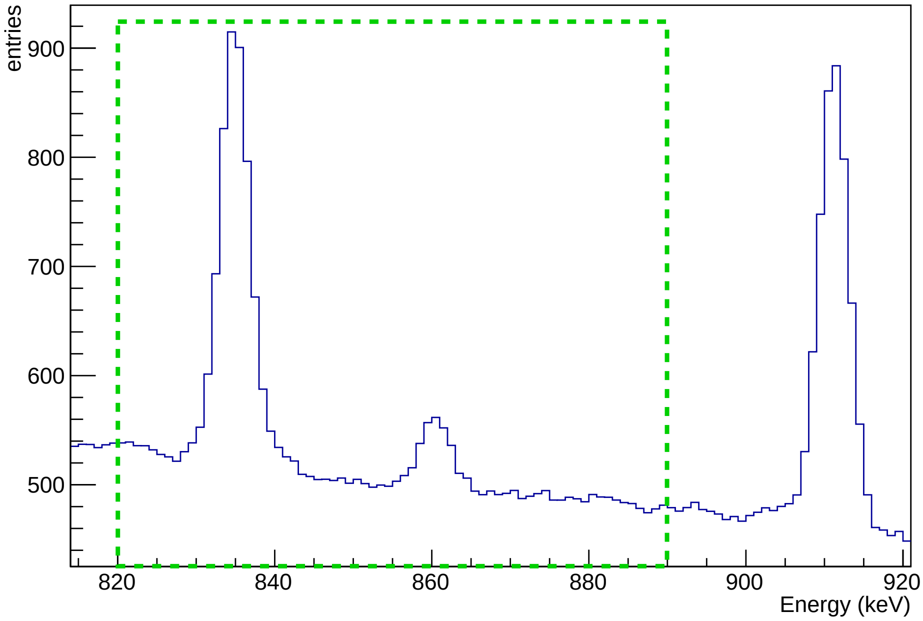

FIG. 6.3: M1 spectrum from BM simulations in the proximity of ^{128}Te $0\nu\beta\beta$ decay Q-value. From left to right: ^{54}Mn γ at 834.8 keV, ^{208}Tl γ at 860.6 keV and ^{228}Ac γ at 911.2 keV. The ROI chosen for the analysis is delimited by the dashed green box, and includes the ^{54}Mn and ^{208}Tl lines.

Bayes' theorem, according to which it is possible to make an inference on an observable by evaluating its posterior probability distribution from the product of the likelihood function and the prior probabilities (see app. A). The Bayesian fit for the ^{128}Te $0\nu\beta\beta$ decay search is performed with the Bayesian Analysis Toolkit (BAT): this software samples from the parameters posterior probability by performing a Markov Chain Monte Carlo (MCMC), exploiting the Metropolis-Hastings algorithm[122]. An overview of the numerical implementation of the Bayesian analysis with MCMC can be found in app. A.1. In the following, the parameters values corresponding to the maximum of the full posterior, i.e. the multi-dimensional posterior containing the dependence on all the parameters, will be referred to as *global mode*; the *marginalized mode* will instead indicate the maximum of the marginalized posteriors. After the full posterior sampling is completed, the point with the highest probability is found by the MCMC, but this does not necessarily correspond to the global mode. BAT performs then a more precise estimation of the mode by means of the Minuit minimization algorithm, which explores the parameters' space around the MCMC maximum following the function's gradient until the real mode is found.

The lower limit on the $0\nu\beta\beta$ decay is taken as the rate corresponding to the 90% of the marginalized posterior, i.e. the posterior distribution integrated over all the parameters of the fit but the signal rate.

6.3.1 Fit model

The parameter of interest in the $0\nu\beta\beta$ decay search analysis is the decay rate $\Gamma^{0\nu}$. This section is dedicated to the detailed description of the model used in the Bayesian fit to make a statistical inference on it.

The fit performed in this analysis does not operate on each single event of the data as for the ^{130}Te $0\nu\beta\beta$ decay search, but on binned histograms. In particular, a histogram is produced for each dataset, and the fit is simultaneously performed on the five involved ones. Given a histogram containing a certain number of events in each bin, the probability of observing n_i events in the i-th bin when on the average μ_i are expected is described by a Poisson probability. The binned likelihood for each histogram is then the product of Poissonian terms, and the total likelihood is given by:

$$\mathscr{L} = \prod_{ds} \prod_{i}^{N_{bins}} \frac{\mu_i^{n_i}\, e^{-\mu_i}}{n_i!} \tag{6.5}$$

In the approximation of small bin width, the number of expected counts μ_i in the i-th bin can be taken as the value of the model function at the center of the bin:

$$\mu_i = S \cdot f_S^{ds}(i) + C_{Mn} \cdot f_{Mn}^{ds}(i) + C_{Tl} \cdot f_{Tl}^{ds}(i) + C_b \cdot f_{flat}(i) + f_{linear}(i) \tag{6.6}$$

where S, C_{Mn} and C_{Tl} are the number of counts at the signal, ^{54}Mn and ^{208}Tl peaks, C_b is the number of counts due to the continuous background and $f_S^{ds}(i)$, $f_{Mn}^{ds}(i)$, $f_{Tl}^{ds}(i)$, $f_{flat}(i)$ and $f_{linear}(i)$ are the values at the i-th bin of the probability density functions used to model the shape of each component. A bin width multiplication factor is included in the definition of each term with the only exception of $f_{linear}(i)$, as it will be shown later in this section.

Before entering in the detail of the definition of each contribution, it is worth to spend few words on the function used to model the peaks. Their shape is modelled with the sum of three Gaussian distributions according to the CUORE detector response function (the *lineshape function*, sec. 5.1.2), but this had to be adapted to the framework of a binned likelihood. Indeed, the response function of eq. 5.1 is defined for each detector-dataset pair as a continuous function of energy; thus, in case of an unbinned fit, its value can be computed at each event energy. This approach cannot be applied for a binned fit, where the likelihood of eq. 6.5 defined for each dataset histogram runs over the bins, instead of the events: in this case, the lineshape has to be applied to each bin. To this purpose, an average lineshape function mediated over all the detectors is defined for each dataset, such that its value at the i-th bin is given by:

$$f_j^{ds}(i) = \frac{\sum_c f_j^{c-ds}(i) \cdot \text{exposure}_{c-ds} \cdot w_i}{\sum_c \text{exposure}_{c-ds}} \qquad j = S,\, Mn,\, Tl \tag{6.7}$$

where the index c runs over all the detectors (c as 'crystal'), $f_j^{c-ds}(i)$ is the value of the lineshape function of the component j for the $c-ds$ pair at the center of the i-th bin (in the assumption that the bin width w_i is small enough to consider the lineshape as linear in the bin), and exposure$_{c-ds}$ is the exposure of the c-th detector in the dataset ds. The $f_j^{c-ds}(i)$ are corrected by the corresponding values of the resolution *scaling* and *bias* in the energy reconstruction, according to eq. 5.2.

In the following, the definition of each of the four components of eq. 6.6 are detailed, and the dependence of each term on the fit parameter will be shown. With the exception of the $0\nu\beta\beta$ decay rate $\Gamma^{0\nu}$, all the others represent nuisance parameters.

Signal term

The $0\nu\beta\beta$ decay rate $\Gamma^{0\nu}$ in units of y^{-1}, namely the parameter of interest of this analysis, is implemented in the definition of the expected number of signal counts S for a given dataset:

$$S = \Gamma^{0\nu} \cdot \frac{N_A}{A_{TeO_2}} \cdot \eta_{128} \cdot (M\Delta t)_{ds} \cdot \epsilon_{ds}^{cut} \cdot \epsilon_{MC} \tag{6.8}$$

where N_A is the Avogadro constant, A_{TeO_2} is the TeO_2 molar mass, η_{128} is the natural isotopic abundance of ^{128}Te, $(M\Delta t)_{ds}$ is the exposure of the dataset in kg·y units, ϵ_{ds}^{cut} is the total analysis efficiency of the dataset, while ϵ_{MC} is the full containment efficiency obtained in 6.4 from the Monte Carlo simulations of the signal. The decay rate $\Gamma^{0\nu}$ is assumed in the model as a global parameter, namely common to all the datasets.

^{54}Mn term

The ^{54}Mn is produced by cosmogenic activation of copper, which took place before the concerned cryostat and detector structure components were moved underground at the LNGS. This element has a half life of 312.2 days; the analyzed data were taken over a period of ∼2 years, thus the number of events due to ^{54}Mn decay contributing to the ROI is expected to decrease over time according to the well known

$$N(t) = N\, e^{-\frac{t}{\tau}} \tag{6.9}$$

To account for this reduction, an exponential multiplicative factor is included in the definition of the number of expected ^{54}Mn events at each dataset:

$$C_{Mn} = \Gamma_{Mn} \cdot e^{-\frac{t_{ds}}{\tau_{Mn}}} \cdot (M\Delta t)_{ds} \cdot \epsilon_{ds}^{cut} \tag{6.10}$$

where t_{ds} is taken as the start-time of the dataset with respect to the beginning of the data taking. The ^{54}Mn rate Γ_{Mn} is expressed in units of counts/(kg·y), and represents a nuisance parameter of the fit common to all the datasets.

^{208}Tl term

The ^{208}Tl belongs to the natural occurring ^{232}Th chain. This element is characterized by a short half life of 3 minutes, thus its rate is expected to be constant in time according to the secular equilibrium of the chain, assuming that this is satisfied. The expected number of events at the ^{208}Tl peak in the ROI for a given dataset is then defined as:

$$C_{Tl} = \Gamma_{Tl} \cdot (M\Delta t)_{ds} \cdot \epsilon_{ds}^{cut} \tag{6.11}$$

where the ^{208}Tl decay rate Γ_{Tl} is expressed in units of counts/(kg·y). As for the ^{54}Mn rate, this represents a nuisance parameter of the fit, and according to its definition and to the assumption of secular equilibrium, it is considered as common to all the datasets.

Continuous background term

The continuous background distribution is modelled with a first order polynomial function of energy according to the following expression:

$$C_b \cdot f_{flat}(i) + f_{linear}(i) = \frac{C_b}{\Delta E_{ROI}} + \frac{m_{ds}}{\Delta E_{ROI}}(E_i - E_{1/2}) \tag{6.12}$$

where ΔE_{ROI} is the region of interest width in energy, C_b and m_{ds} are the expected number of events and the background slope for a given dataset, E_i is the energy at the center of the i-th bin and $E_{1/2}$ is the energy corresponding to the half of the ROI window. This parametrization of $f_{linear}(i)$ is represented in figure 6.4, and is particularly convenient since its integral is 0, thus the meaning of C_b remains unchanged. The expected number of events C_b at each dataset is defined as:

$$C_b = \mathrm{BI}_{ds} \cdot (M\Delta t)_{ds} \cdot w_i \tag{6.13}$$

being BI_{ds} the *background index* corresponding to the dataset in units of counts/(keV·kg·y), and the other terms have the same meaning as in the previous definitions. The slope and the background index are also included as nuisance parameters in the fit, and are treated as dataset-dependent quantities.

The described model including both the background structures and the hypothesized $0\nu\beta\beta$ peak will be referred to in the following as the *signal plus background model* (S+B), while in the *background-only model* (B) the signal contribution is not included.

To sum up, the S+B model of the Bayesian fit for the search of the ^{128}Te $0\nu\beta\beta$ decay includes one parameter of interest, which is decay rate $\Gamma^{0\nu}$, plus 12 of nuisance, corresponding to the ^{54}Mn and ^{208}Tl decay rates, and one background index and slope for each dataset, for a total of 13 parameters.

After the detailed description of the likelihood, the choice of the prior functions is discussed. A flat non-informative prior was used for each parameter of the fit, for the reasons that will be clear in the following. The past limit on the parameter of interest $\Gamma^{0\nu}$ was obtained with a different analysis approach, based on the minimization of the likelihood

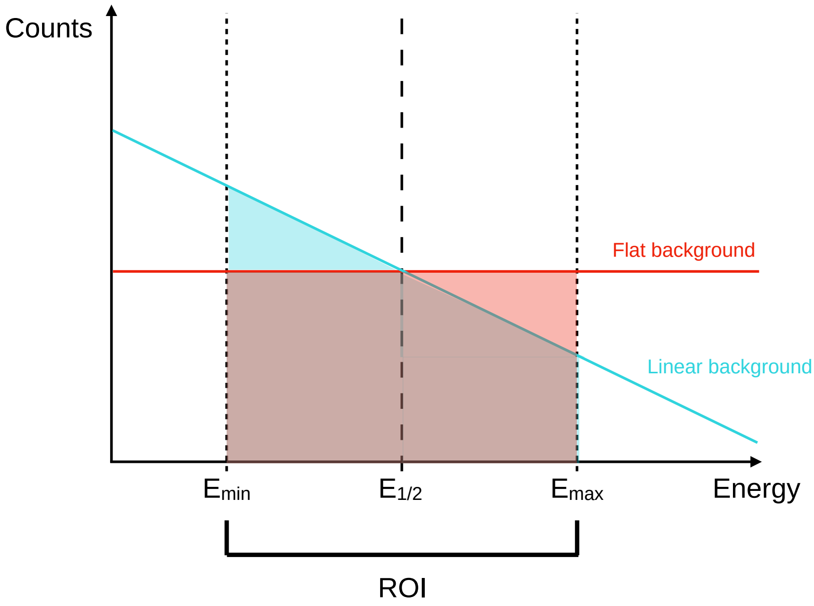

FIG. 6.4: Scheme of the linear background parametrization as an odd function. This implementation is convenient since no additional normalizing factors are required in the code.

chi-square[44], thus no information on the signal rate posterior probability is available. In addition, the limit was achieved with a factor ∼100 lower experimental mass with respect to CUORE, whose sensitivity to this process is expected to be a factor ∼10 higher. The absence of knowledge on $\Gamma^{0\nu}$ at the range that CUORE is able to probe justifies the choice of a uniform prior for $\Gamma^{0\nu} > 0$ according to the Principle of Indifference, which assigns equal probabilities to all the possible values up to a maximum that can be greater that the past limit. For what concerns the nuisance parameters of the fit, which are all related to the background structures in the ROI, information can be extracted from the CUORE Background Model: however, this is constructed by performing a fit on the same data that are used for the present analysis, and including such information would introduce a bias in the result. Thus, in absence of independent measurements, a uniform prior is chosen for each of the nuisance parameters as well.

6.4 Testing the fit quality on toy Monte Carlo simulations

Before performing the analysis on the real data to extract the final results, the fit method was tested and validated on toy Monte Carlo simulations (toyMC) of the ROI spectrum. It is important to optimize the fit strategy on an independent set of data to avoid the introduction of possible bias. To this purpose, a specific code was developed in order to simulate the components of the ROI spectrum according to the model implemented in the likelihood. A single toyMC consists of 5 separate simulations corresponding to the exposures of the 5 datasets included in this analysis, and the events are represented as continuous variables of energy rather than in binned histograms. In this way, the CUORE data organization is reproduced in the simulations. The parameters Γ^{toy}_{Mn}, Γ^{toy}_{Tl}, BI^{toy} and m^{toy} according to which the various components are generated were estimated from the available knowledge of the CUORE Background Model: a binned maximum likelihood fit with two gaussian distributions for the peaks plus a linear background was performed on the BM simulations, that include the events of the five datasets together (fig. 6.5). From this fit, the number of events C^{BM}_{Mn}, C^{BM}_{Tl} and C^{BM}_{b} of the three components and the slope m^{BM} were extracted; the first three were used to estimate Γ^{toy}_{Mn}, Γ^{toy}_{Tl} and BI^{toy} as follows. These counts represent the sum of the events at each dataset:

$$C^{BM}_{Mn} = \sum_{ds} C^{ds}_{Mn} \quad , \quad C^{BM}_{Tl} = \sum_{ds} C^{ds}_{Tl} \quad , \quad C^{BM}_{b} = \sum_{ds} C^{ds}_{b} \tag{6.14}$$

By plugging the 6.10, the 6.11 and the 6.13 in the respective expressions, the Manganese and Thallium rates Γ^{toy}_{Mn}, Γ^{toy}_{Tl} and the background index BI^{toy} are obtained:

$$\Gamma^{\text{toy}}_{Mn} = \frac{C^{BM}_{Mn}}{\sum_{ds} e^{-\frac{t_{ds}}{\tau}} \cdot (M\Delta t)_{ds} \cdot \epsilon^{PSA}_{ds}} \tag{6.15}$$

$$\Gamma^{\text{toy}}_{Tl} = \frac{C^{BM}_{Tl}}{\sum_{ds} \cdot (M\Delta t)_{ds} \cdot \epsilon^{PSA}_{ds}} \tag{6.16}$$

$$\text{BI}^{\text{toy}} = \frac{C^{BM}_{b}}{\sum_{ds} (M\Delta t)_{ds} \cdot \Delta E_{ROI}} \tag{6.17}$$

where the total analysis efficiency ϵ^{cut}_{ds} was replaced by the PSA efficiency ϵ^{cut}_{PSA} coherently with the BM simulations, which are produced accounting for it only, and ΔE_{ROI} is the ROI energy window. For the sake of simplicity, a common value of BI for all the datasets was considered in the toyMC simulations.

The resulting Γ^{toy}_{Mn}, Γ^{toy}_{Tl}, BI^{toy} and m^{toy} are summarized in table 6.6. The toyMC are produced by Poisson floating the expected number of counts at each dataset corresponding to these values; the generated slope is the one extracted from the fit, thus $m^{\text{toy}} = m^{BM}$.

The Bayesian fit and the procedure to extract the CUORE exclusion sensitivity to the ^{128}Te $0\nu\beta\beta$ decay were validated on toyMC simulations produced with the described method, before performing the analysis on the data. Several tests were made and will be described in the following sections: the first consisted of verifying if the fit correctly reconstructs the simulated background parameters (sec. 6.4.1). The validation of the exclusion sensitivity study was then carried out taking advantage of the toyMC simulations and fits performed during the previous test (sec. 6.4.2); finally, a study aimed at inspecting if a bias is introduced in the $0\nu\beta\beta$ decay rate reconstruction in presence of a signal contribution in the toyMC was performed (sec. 6.4.3).

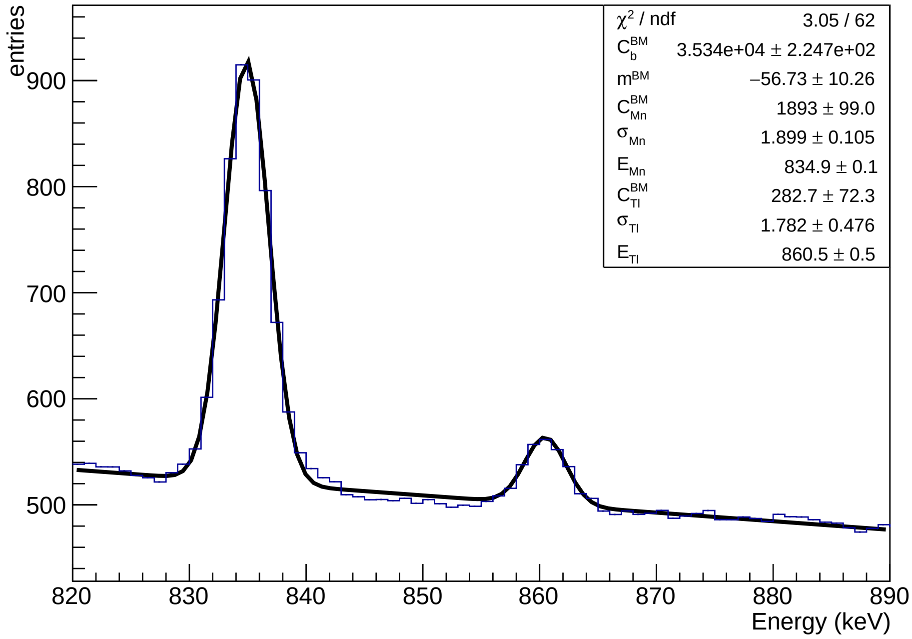

FIG. 6.5: Binned extended maximum likelihood fit performed on the CUORE BM simulations, to extract the number of events due to the ^{54}Mn, the ^{208}Tl and to the continuous contribution.

Parameter	Units	Value for toyMC
Γ^{toy}_{Mn}	cts/(kg·y)	16.27
Γ^{toy}_{Tl}	cts/(kg·y)	0.95
BI^{toy}	cts/(keV·kg·y)	1.68
m^{toy}	1/keV	-56.73

TABLE 6.6: Values of the ^{54}Mn and ^{208}Tl rates, background index and slope used in the toyMC generation. These are obtained from the results of the fit on the BM simulations.

6.4.1 Background components reconstruction test

In order to test if the simulated background components are correctly reconstructed by the fit, 10^4 toyMC were produced without the signal contribution, according to the parameters listed in table 6.6; a S+B Bayesian fit was then performed on each toyMC independently. In order to compare the parameters extracted from each fit with the generated ones, the distributions of the best fit values from all the toyMC were built for each parameter. These are expected to be centered at the values used to produce the toyMC.

The mean position of each distribution was evaluated by means of a gaussian fit, as shown in fig. 6.7 for the BIs, in fig. 6.9 for the slopes and fig. 6.11 for the ^{54}Mn and ^{208}Tl rates. Due to the fact that the linear term defined in eq. 6.12 is not multiplied by the bin width, the returned background slope value corresponds to m^{toy}/N_{bins}. In the present case $N_{bins} = 140$, since a bin size of 0.5 keV/bin is adopted for a ROI of 70 keV width.

The means are summarized in tables 6.8, 6.10 and 6.12: the large number of toyMC adopted for this test allowed to identify a small bias in the reconstruction of the BI and the slope, corresponding to a $<0.15\%$ underestimation and a $\leq 1.6\%$ overestimation of the generated BI and m, respectively. No correlations were found between BI and m; a typical 2D plot of the distribution of these parameters is shown in figure 6.13. The reconstructed values of the ^{54}Mn and ^{208}Tl rate are instead compatible with the injected values. These results show that the tested model is well describing the features of the simulated spectrum.

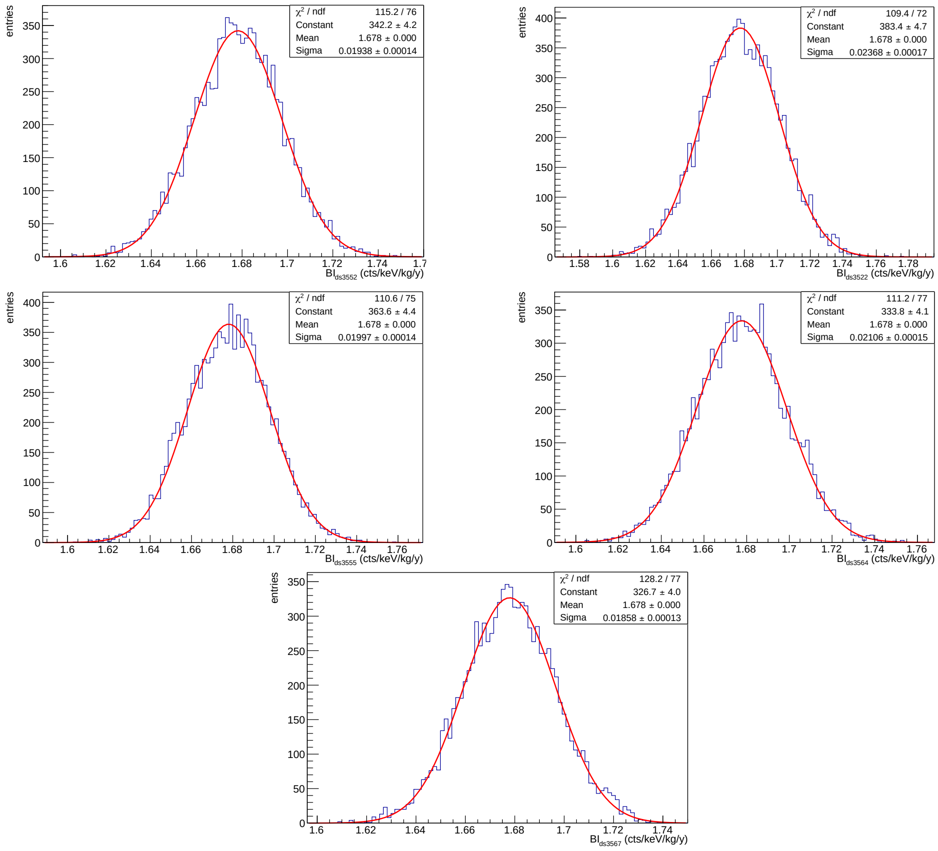

FIG. 6.7: Distributions of the BI global mode for each dataset, as reconstructed by the Bayesian fit on the 10^4 toyMC background-only simulations. The distributions are fitted with a gaussian function to determine the mean value.

Parameter	Value [counts/(keV·kg·y)]
BI_{ds3522}	1.6775 ± 0.0002
BI_{ds3552}	1.6782 ± 0.0002
BI_{ds3555}	1.6781 ± 0.0002
BI_{ds3564}	1.6776 ± 0.0002
BI_{ds3567}	1.6779 ± 0.0002
$\mathbf{BI^{toy}}$	**1.68**

TABLE 6.8: Summary of the mean values of the BI global mode distributions for each dataset. The BI according to which the toyMC were generated is also reported in the last row as comparison.

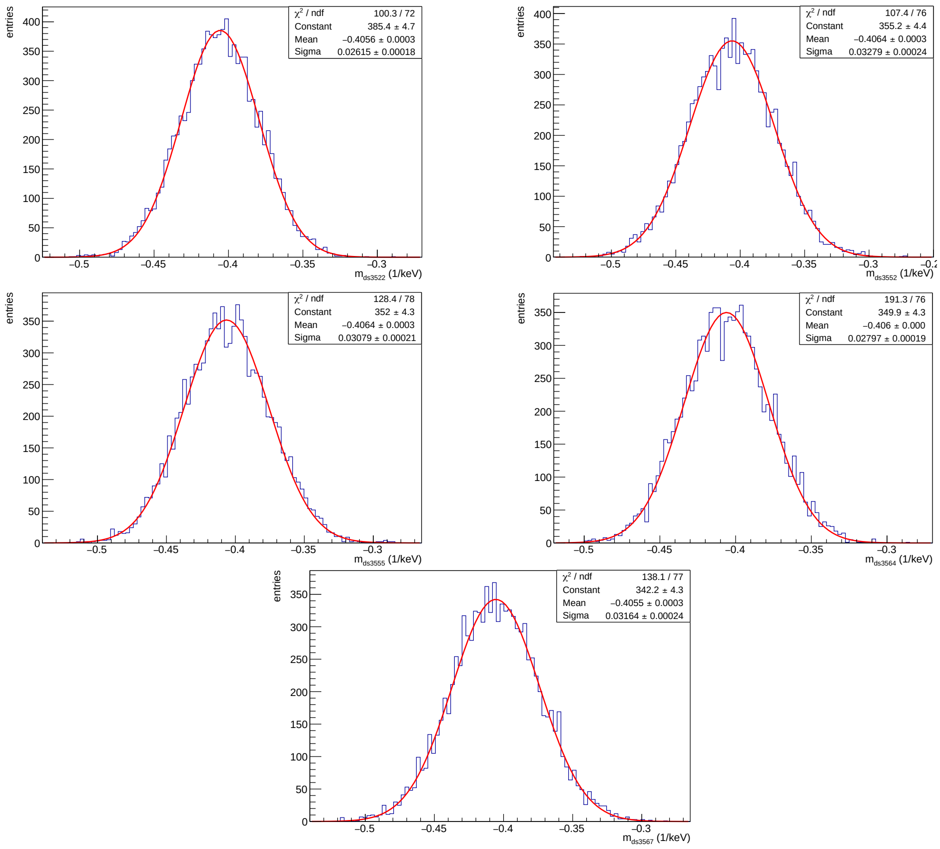

FIG. 6.9: Distributions of the m best fit values for each dataset, as reconstructed from the fit on the 10^4 toyMC background-only simulations.

Parameter	Value [1/keV]
m_{ds3522}	-0.4056 ± 0.0003
m_{ds3552}	-0.4064 ± 0.0003
m_{ds3555}	-0.4064 ± 0.0003
m_{ds3564}	-0.4060 ± 0.0003
m_{ds3567}	-0.4055 ± 0.0003
$\boldsymbol{m^{\mathbf{toy}}/\mathbf{N_{bins}}}$	**-0.4**

TABLE 6.10: Summary of the mean values of the m global mode distributions for each dataset. The slope according to which the toyMC were generated is also reported in the last row as comparison, divided by the number of bins of the Bayesian fit.

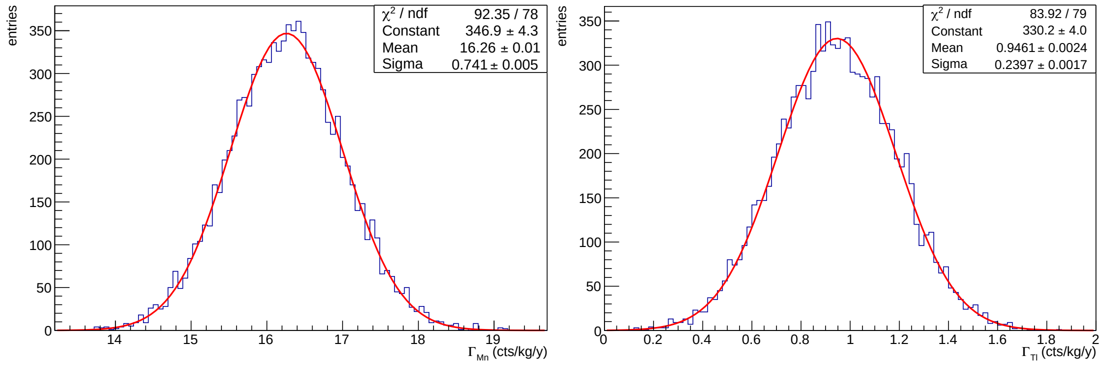

FIG. 6.11: Distributions of the ^{54}Mn and ^{208}Tl best fit values, as reconstructed from the fit on the 10^4 toyMC background-only simulations.

Parameter	Value [1/(kg·y)]
Γ_{Mn}	16.259 ± 0.007
Γ_{Tl}	0.946 ± 0.002
$\boldsymbol{\Gamma_{Mn}^{toy}}$	**16.27**
$\boldsymbol{\Gamma_{Tl}^{toy}}$	**0.95**

TABLE 6.12: Summary of the mean values of the Γ_{Mn} and Γ_{Tl} global mode distributions. The rates according to which the toyMC were generated are also reported in the last row as comparison.

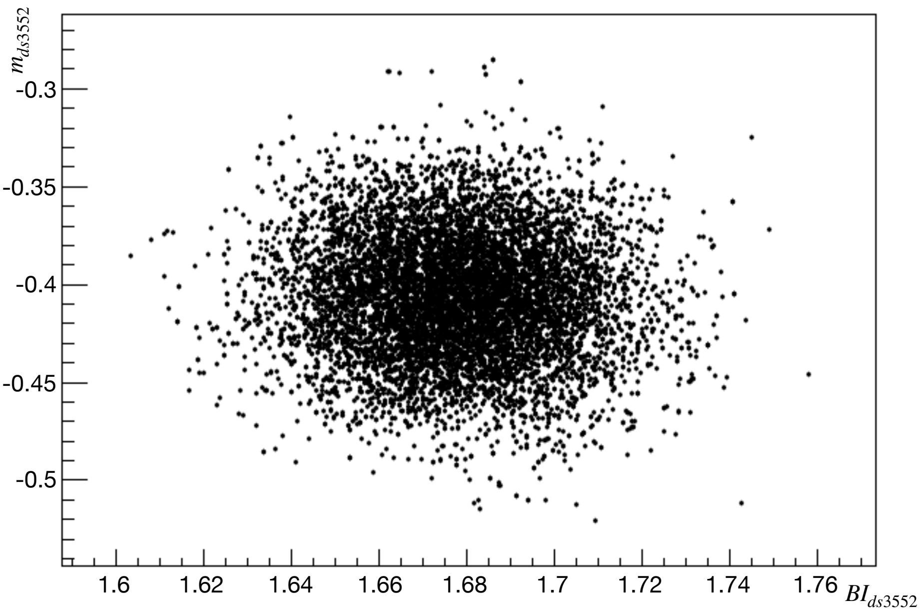

FIG. 6.13: Example of 2D plot of the BI and slope parameters, as reconstructed by the fit on the 10^4 toyMC. No correlation is observed.

6.4.2 Exclusion Sensitivity test

The median exclusion sensitivity is defined as the median of the distribution of the 90% C.I. limits on the $0\nu\beta\beta$ decay half life, each resulting from a S+B fit to one of the 10^4 background-only toyMC simulations. Taking advantage of the toyMC and fits performed during the test described in the previous section, the distribution of the 90% C.I. extracted limits on $T^{0\nu}_{1/2}$ was built, and a median exclusion sensitivity of $\hat{T}^{0\nu}_{1/2} = 2.2 \cdot 10^{24}$ y was obtained (fig. 6.14). This value refers to the toyMC performed with the parameters extracted from the BM as described in sec. 6.4, and provides a preliminary indication of the actual CUORE exclusion sensitivity, that will be discussed in sec. 6.5.

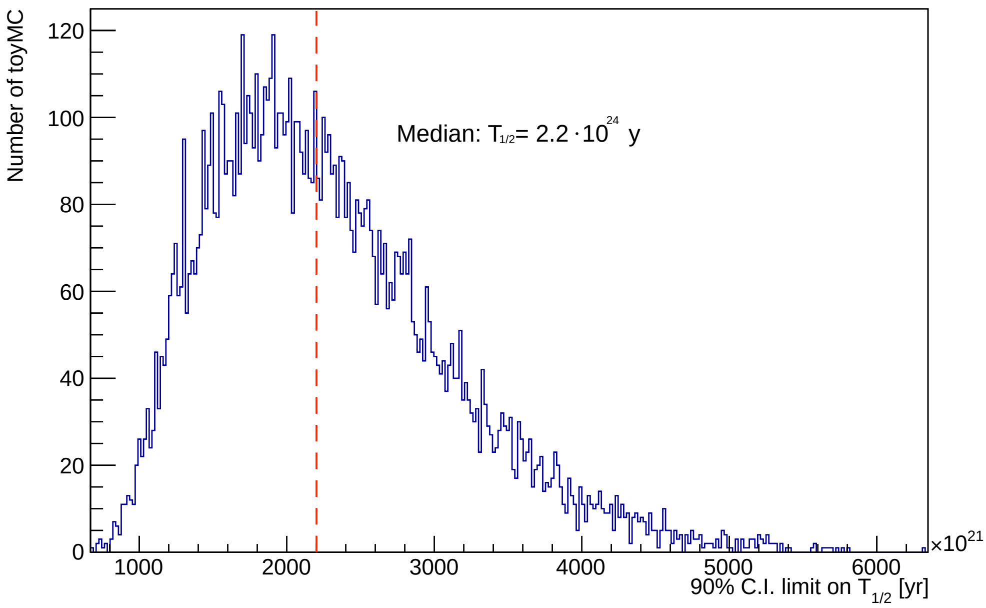

FIG. 6.14: Test distribution of the 90% half life limits extracted from the S+B fits on the background-only toyMC simulations. The toyMC were produced with the parameters extracted from the BM, as described in sec. 6.4.

6.4.3 Signal rate reconstruction test

The test described in the following was aimed at evaluating if a bias is artificially introduced by the Bayesian fit on the signal rate reconstruction. This is an essential aspect for a correct interpretation of the final results of this analysis, whose goal is to make a statistical inference on this parameter. To this purpose, the S+B fit was repeated on five sets of 2000 toyMC where different signal contributions were introduced. In order to effectively evaluate the presence of a bias in the reconstructed $\Gamma_{0\nu}$, the $\Gamma_{0\nu} > 0$ condition in the prior was released, so that the rate is also allowed to assume non-physical values. The rate $\Gamma_{0\nu} = 3.2 \cdot 10^{-25}\ y^{-1}$ corresponding to the test median exclusion sensitivity $\hat{T}^{0\nu}_{1/2} = 2.2 \cdot 10^{24}\ y$ (sec. 6.4.2) was taken as reference to select the five signal rates according to which the $0\nu\beta\beta$ events should be generated: these are $2 \cdot 10^{-25}\ y^{-1}$, $4 \cdot 10^{-25}\ y^{-1}$,

$6 \cdot 10^{-25}\ y^{-1}$, $8 \cdot 10^{-25}\ y^{-1}$ and $10^{-24}\ y^{-1}$.

The distributions of the $\Gamma_{0\nu}$ global modes extracted from the Bayesian fits on each toyMC set were built and fitted with a gaussian function, to evaluate the mean reconstructed rate. As for the background components test (sec. 6.4.1), these distributions are expected to be centered at the injected values, if the fit properly estimates the signal contribution.

The $\Gamma_{0\nu}$ distributions relative to each generated signal rate are shown in fig. 6.15; the corresponding means and simulated rates are summarized in table 6.16. These were represented in the plot of fig. 6.17, to evaluate the reconstructed signal rate as a function of the injected one. The relation between the two is well described by a linear function, whose intercept is compatible with 0 at a $\sim 1.3\sigma$ statistical significance and the slope is compatible with 1 within 1σ. These results allow to safely assume that no bias is introduced by the tested Bayesian fit on the reconstruction of the parameter of interest.

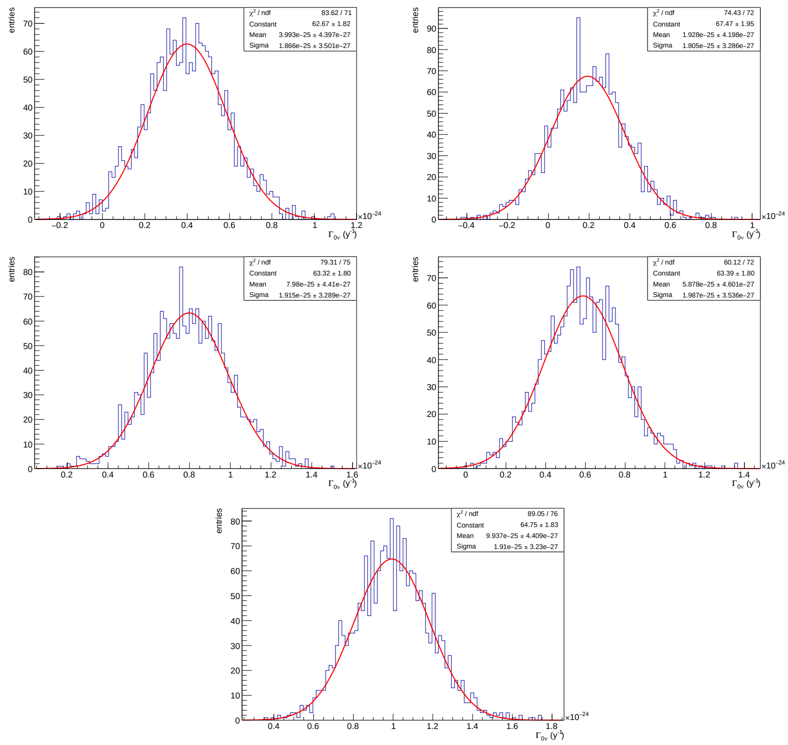

FIG. 6.15: Distributions of the reconstructed values of $\Gamma_{0\nu}$ for the five different injected rates. A gaussian fit is performed on each distribution to extract the value of the mean reconstructed signal rate.

Injected $\Gamma_{0\nu}$ [10^{-25} 1/y]	Reconstructed $\Gamma_{0\nu}$ (mean) [10^{-25} 1/y]
2	1.93 ± 0.04
4	3.99 ± 0.04
6	5.88 ± 0.05
8	7.98 ± 0.04
10	9.94 ± 0.04

TABLE 6.16: Summary of the signal rates injected in the toyMC sets for the bias study and the corresponding reconstructed mean rate, as extracted from the gaussian fit on the respective distributions. The values are slightly underestimated, but are compatible within 2σ with the generated ones.

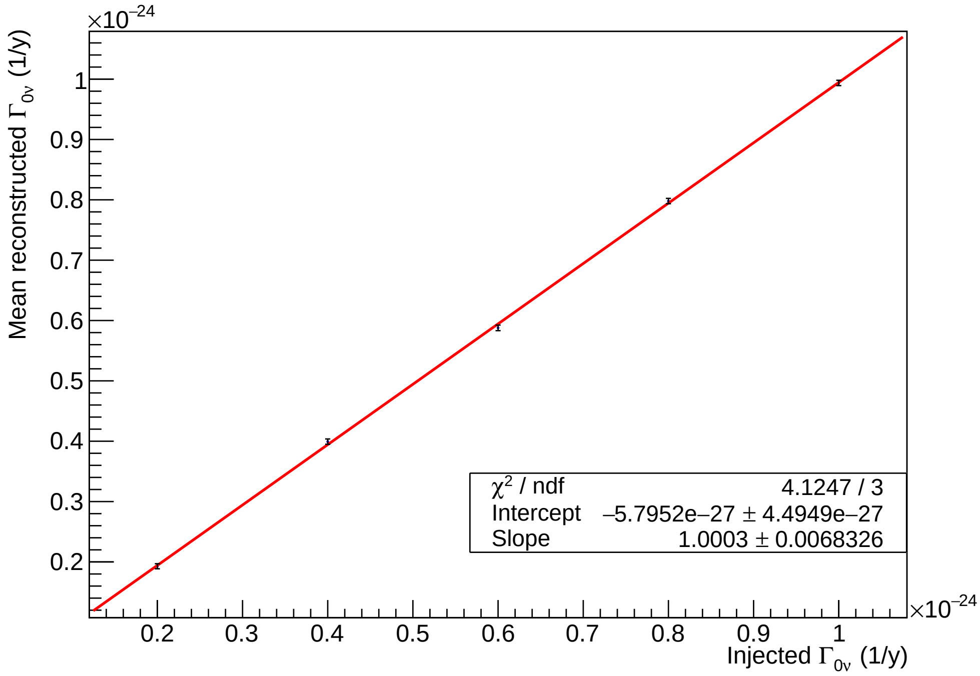

FIG. 6.17: Linear fit on the mean reconstructed signal rate as a function of the injected one. The points of this plot correspond to the values reported in table 6.16. The resulting intercept and slope are compatible with 0 and 1, respectively.

6.5 ^{128}Te $0\nu\beta\beta$ decay search results

This section is dedicated to the presentation of the outcome of my PhD work, namely the final results of the ^{128}Te $0\nu\beta\beta$ decay search with the CUORE detectors. After the test and validation campaign on the analysis procedure described in the previous sections, the Bayesian fit was performed on the CUORE data corresponding to a 309.33 kg·y total exposure.

6.5.1 Results of signal+background fit on data

The results of the signal plus background binned Bayesian fit on the ^{128}Te $0\nu\beta\beta$ decay ROI are summarized in table 6.22. The definition of the $\Gamma_{0\nu}$ prior is restricted to physical values only ($\Gamma_{0\nu} > 0$). For each of the 13 parameters, both the values of the global mode and the marginalized mode are reported; the uncertainty on the global modes is given by the error resulting from the minimization algorithm (Minuit), while the uncertainties calculated from the 16% and 84% quantiles of the posteriors, i.e. $+[q(84\%)-\text{mode}]$ $-[\text{mode}-q(16\%)]$, are associated to the marginalized modes. The biases identified during the tests in the reconstruction of the BIs and the slopes result to be irrelevant, as the uncertainties on the values resulting from the fit are larger (>1% for the BIs and >40% for the slopes).

No evidence is found for the ^{128}Te $0\nu\beta\beta$ decay. The signal rate marginalized posterior is shown in fig. 6.18-(a); the 90% C.I. is shown by the filled area. The 90% C.I. limit on the signal rate extracted from this posterior is given by:

$$\boldsymbol{\Gamma_{0\nu} < 1.9 \cdot 10^{-25}\ y^{-1}} \tag{6.18}$$

According to the relation $T_{1/2} = \ln 2/\Gamma_{0\nu}$, such lower limit on $\Gamma_{0\nu}$ corresponds to a 90% C.I. upper limit on the ^{128}Te $0\nu\beta\beta$ decay half life of:

$$\boldsymbol{T^{0\nu}_{1/2} > 3.6 \cdot 10^{24}\ y} \tag{6.19}$$

These results represent the most stringent limits on the $0\nu\beta\beta$ decay of ^{128}Te to date; the half life limit obtained in this work is ~33 times higher than the last limit of $1.1 \cdot 10^{23}$ y gathered by MiDBD in 2003. In addition, this is the first time that a direct experiment is able to set a more stringent limit on this isotope with respect to the geochemical experiments.

The combined fit on the ROI spectrum is represented in fig. 6.18-(b): the red line is the best fit curve where all the parameters assume the values of the global mode, while $\Gamma_{0\nu}$ was fixed at its 90% C.I. limit in the dashed blue one. The marginalized posterior distributions obtained for the nuisance parameters are shown in fig. 6.19.

The S+B fit on the data was then repeated after having released the constrain $\Gamma_{0\nu} > 0$, so that the signal rate is allowed to assume negative values. The results of this fit are summarized in table 6.23; in this situation, an underfluctuation with a statistical significance of $\sim 1.4\sigma$ is observed, as it can be inferred from the full-range $\Gamma_{0\nu}$ marginalized posterior shown in fig. 6.20-(b) and from the $\Gamma_{0\nu}$ global and marginalized modes of $(-2.5 \pm 1.8) \cdot 10^{-25}$ y^{-1} and $(-2.3^{+1.6}_{-2.1}) \cdot 10^{-25}$ y^{-1} respectively.

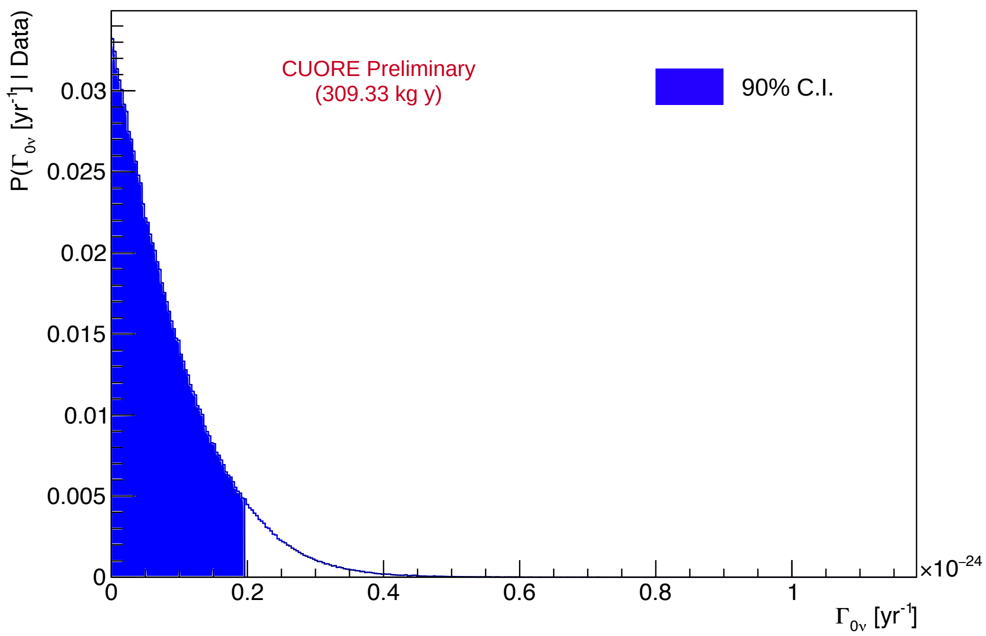

(a)

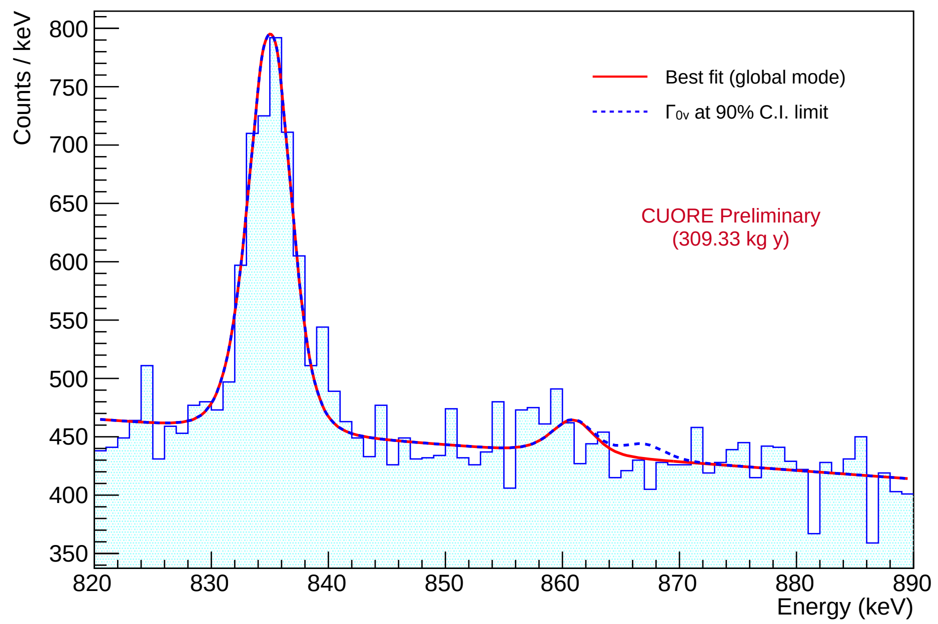

(b)

FIG. 6.18: (a) Signal rate marginalized posterior, as obtained from the S+B fit on data where $\Gamma_{0\nu}$ is restricted to positive values only. (b) Signal plus background fit on the ROI spectrum. The red curve refers to the best fit function, where all the parameters assume the global mode values. In the dashed blue line, the signal rate $\Gamma_{0\nu}$ is instead fixed at its 90% C.I. limit.

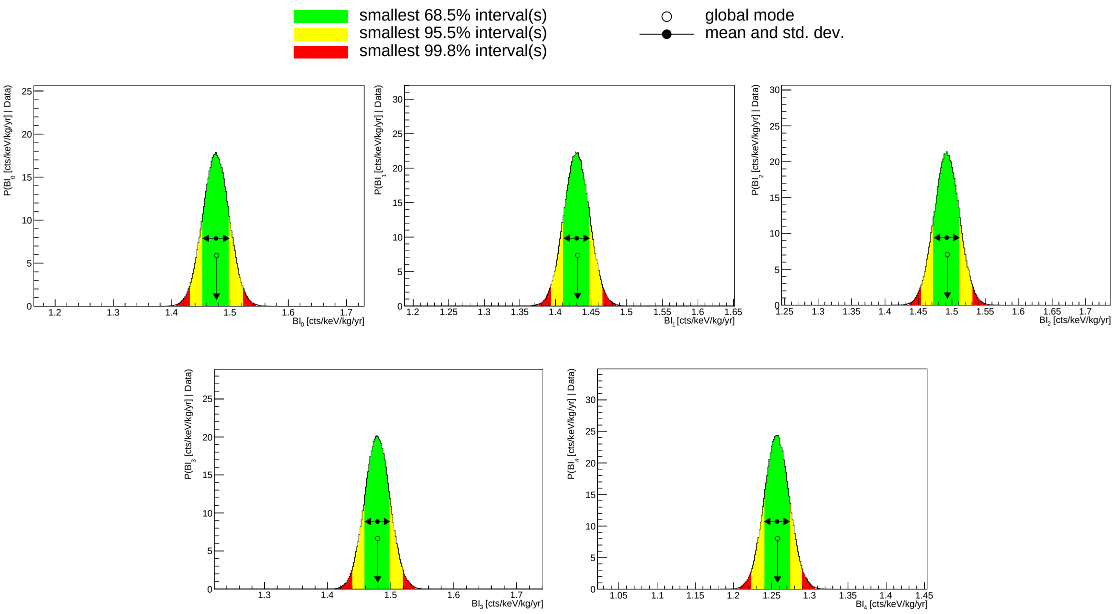
smallest 68.5% interval(s)
smallest 95.5% interval(s)
smallest 99.8% interval(s)
global mode
mean and std. dev.
P(BI_0 [cts/keV/kg/yr] | Data)
BI_0 [cts/keV/kg/yr]
P(BI_1 [cts/keV/kg/yr] | Data)
BI_1 [cts/keV/kg/yr]
P(BI_2 [cts/keV/kg/yr] | Data)
BI_2 [cts/keV/kg/yr]
P(BI_3 [cts/keV/kg/yr] | Data)
BI_3 [cts/keV/kg/yr]
P(BI_4 [cts/keV/kg/yr] | Data)
BI_4 [cts/keV/kg/yr]

(a)

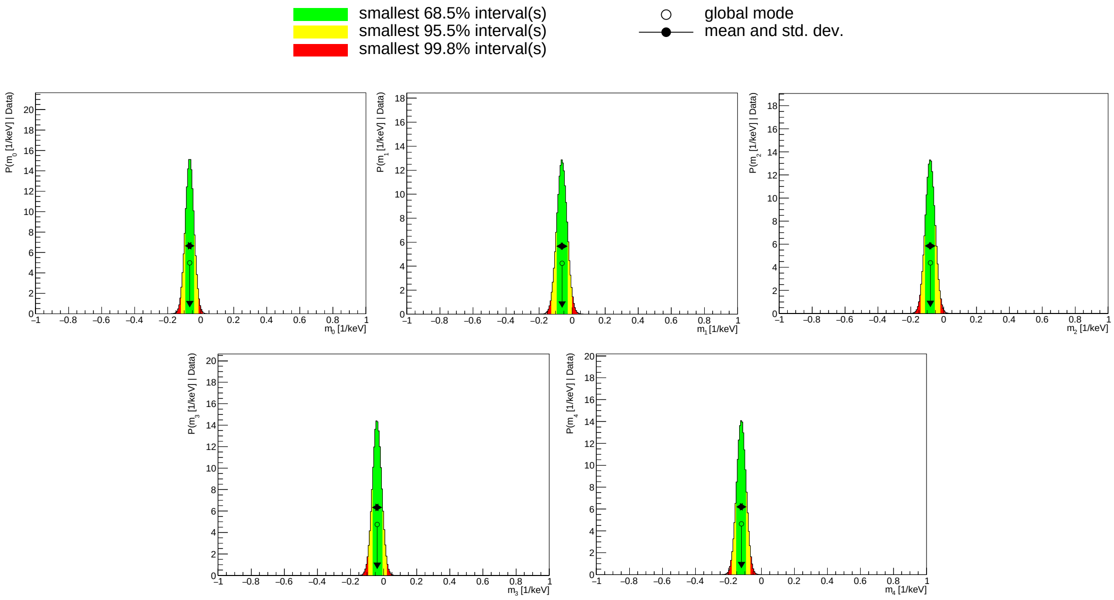
smallest 68.5% interval(s)
smallest 95.5% interval(s)
smallest 99.8% interval(s)
global mode
mean and std. dev.
P(m_0 [1/keV] | Data)
m_0 [1/keV]
P(m_1 [1/keV] | Data)
m_1 [1/keV]
P(m_2 [1/keV] | Data)
m_2 [1/keV]
P(m_3 [1/keV] | Data)
m_3 [1/keV]
P(m_4 [1/keV] | Data)
m_4 [1/keV]

(b)

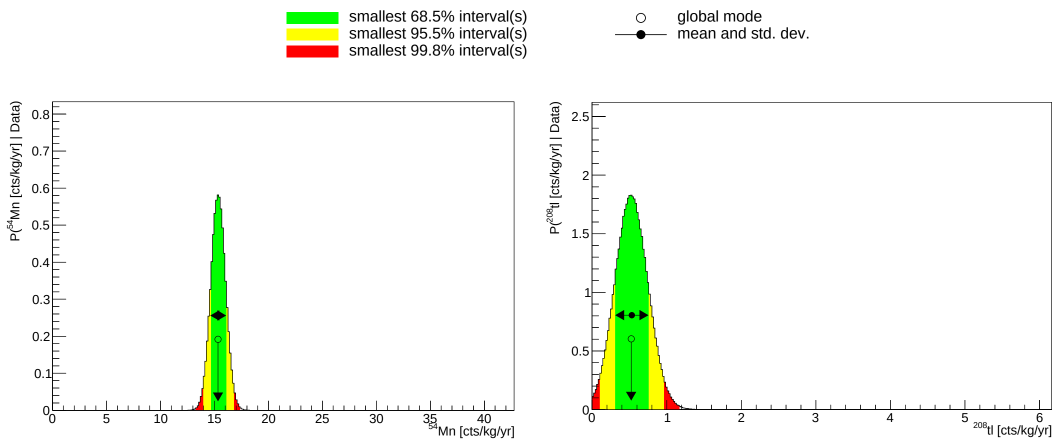

(c)

FIG. 6.19: Marginalized posterior distributions resulting from the signal plus background fit on CUORE data for the BIs (a), the slopes (b) and the ^{54}Mn and ^{208}Tl rates (c).

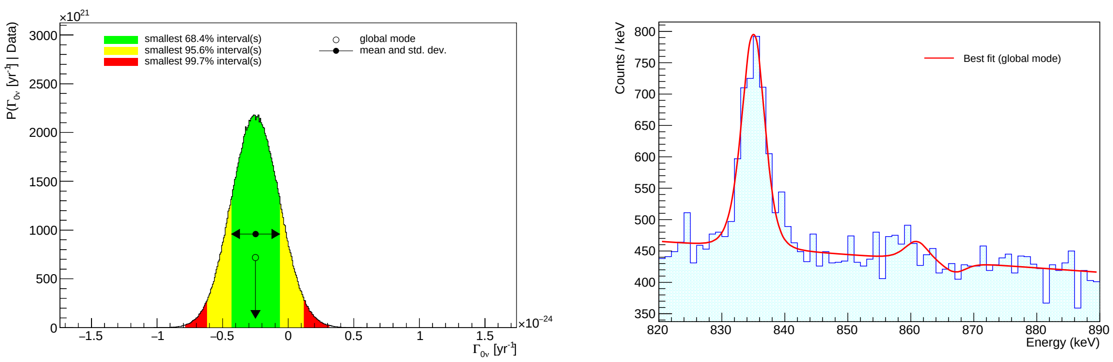

(a) (b)

FIG. 6.20: (a) Posterior distribution of the signal rate resulting from the S+B fit where $\Gamma_{0\nu} < 0$ is allowed. A $\sim 1.4\sigma$ significance underfluctuation is observed. (b) Signal plus background fit on the ROI spectrum. The red curve refers to the best fit function; the signal rate $\Gamma_{0\nu}$ is allowed to assume non-physical values.

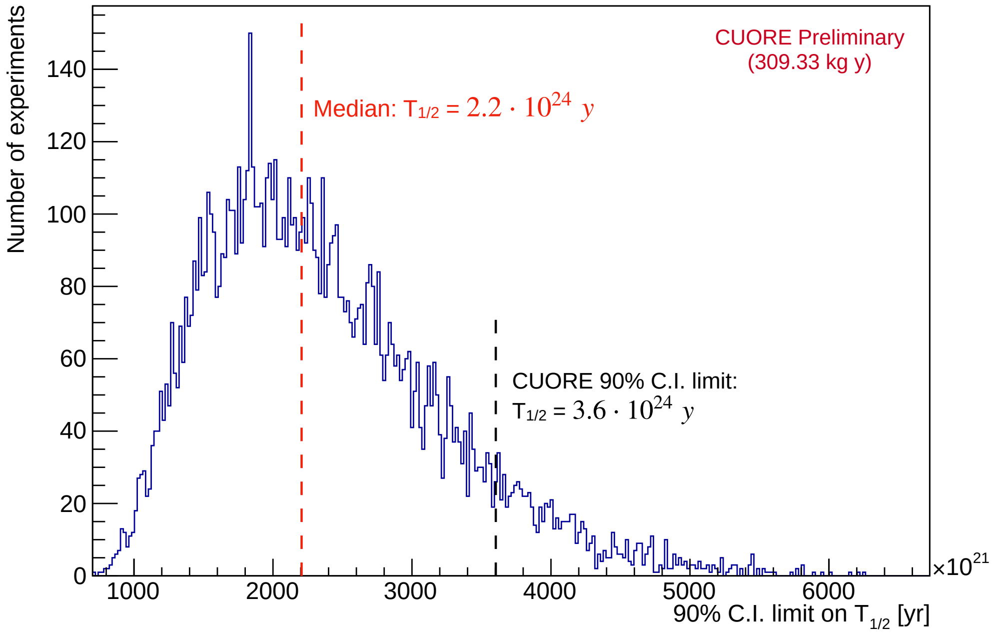

FIG. 6.21: Distribution of the 90% C.I. limits on $T_{1/2}$ extracted from the S+B fits on the background-only toyMC. The parameters used to produce the toyMC are the results on the B fit performed on CUORE data. The dashed red line highlights the median exclusion sensitivity, while the dashed black one shows the position of the 90% C.I. CUORE limit in the distribution.

6.5.2 Results of background-only fit on data and exclusion sensitivity

The background-only Bayesian fit was finally performed on the CUORE data; the resulting global and marginalized modes for all the parameters are summarized in table 6.24. The global modes were then used to produce 10^4 toyMC simulations of the CUORE experiment, with the aim of extracting the median exclusion sensitivity. A S+B fit was performed on each toyMC, and the distribution of the 90% C.I. limits on $T^{0\nu}_{1/2}$ was constructed as in fig. 6.21. The median of such distribution represents the CUORE exclusion sensitivity to the $0\nu\beta\beta$ decay of ^{128}Te:

$$\boldsymbol{\hat{T}^{0\nu}_{1/2} = 2.2 \cdot 10^{24}\ y} \tag{6.20}$$

This value corresponds to the expectation resulting from the test, where the toyMC were constructed according to the BM knowledge (sec. 6.4.2, fig. 6.14). The CUORE limit on the half life is also reported in the figure. From this distribution of the 90% C.I. limits, a 8.8% probability to get a more stringent limit with respect to the current one is obtained.

Parameter	Units	Global Mode	Marginalized Mode
$\Gamma_{0\nu}$	1/y	0	0
BI_{ds3522}	cts/(keV·kg·y)	1.48 ± 0.02	$1.48^{+0.02}_{-0.02}$
BI_{ds3552}	cts/(keV·kg·y)	1.43 ± 0.02	$1.43^{+0.02}_{-0.02}$
BI_{ds3555}	cts/(keV·kg·y)	1.49 ± 0.02	$1.49^{+0.02}_{-0.02}$
BI_{ds3564}	cts/(keV·kg·y)	1.48 ± 0.02	$1.48^{+0.02}_{-0.02}$
BI_{ds3567}	cts/(keV·kg·y)	1.26 ± 0.02	$1.26^{+0.02}_{-0.02}$
m_{ds3522}	1/keV	-0.07 ± 0.03	$-0.06^{+0.02}_{-0.03}$
m_{ds3552}	1/keV	-0.06 ± 0.03	$-0.06^{+0.03}_{-0.03}$
m_{ds3555}	1/keV	-0.08 ± 0.03	$-0.08^{+0.03}_{-0.03}$
m_{ds3564}	1/keV	-0.04 ± 0.03	$-0.04^{+0.03}_{-0.02}$
m_{ds3567}	1/keV	-0.12 ± 0.03	$-0.12^{+0.03}_{-0.03}$
Γ_{Mn}	cts/(kg·y)	15.3 ± 0.7	$15.3^{+0.7}_{-0.6}$
Γ_{Tl}	cts/(kg·y)	0.5 ± 0.2	$0.5^{+0.2}_{-0.2}$

TABLE 6.22: Results of s+b fit with physical range only allowed for the signal rate on data.

Parameter	Units	Global Mode	Marginalized Mode
$\Gamma_{0\nu}$	1/y	$(-2.5 \pm 1.8) \cdot 10^{-25}$	$-2.3^{+1.6}_{-2.1} \cdot 10^{-25}$
BI_{ds3522}	cts/(keV·kg·y)	1.48 ± 0.02	$1.48^{+0.02}_{-0.02}$
BI_{ds3552}	cts/(keV·kg·y)	1.44 ± 0.02	$1.43^{+0.02}_{-0.02}$
BI_{ds3555}	cts/(keV·kg·y)	1.50 ± 0.02	$1.50^{+0.02}_{-0.02}$
BI_{ds3564}	cts/(keV·kg·y)	1.48 ± 0.02	$1.48^{+0.02}_{-0.02}$
BI_{ds3567}	cts/(keV·kg·y)	1.26 ± 0.02	$1.26^{+0.02}_{-0.02}$
m_{ds3522}	1/keV	-0.06 ± 0.03	$-0.06^{+0.03}_{-0.03}$
m_{ds3552}	1/keV	-0.06 ± 0.03	$-0.06^{+0.03}_{-0.03}$
m_{ds3555}	1/keV	-0.08 ± 0.03	$-0.08^{+0.03}_{-0.03}$
m_{ds3564}	1/keV	-0.04 ± 0.03	$-0.04^{+0.03}_{-0.03}$
m_{ds3567}	1/keV	-0.12 ± 0.03	$-0.12^{+0.03}_{-0.03}$
Γ_{Mn}	cts/(kg·y)	15.3 ± 0.7	$15.3^{+0.7}_{-0.7}$
Γ_{Tl}	cts/(kg·y)	0.5 ± 0.2	$0.5^{+0.2}_{-0.2}$

TABLE 6.23: Results of s+b fit with free rate (negative values allowed) on data.

Parameter	Units	Global Mode	Marginalized Mode
BI_{ds3522}	cts/(keV·kg·y)	1.48 ± 0.02	$1.48^{+0.02}_{-0.02}$
BI_{ds3552}	cts/(keV·kg·y)	1.43 ± 0.02	$1.43^{+0.02}_{-0.02}$
BI_{ds3555}	cts/(keV·kg·y)	1.49 ± 0.02	$1.49^{+0.02}_{-0.02}$
BI_{ds3564}	cts/(keV·kg·y)	1.48 ± 0.02	$1.48^{+0.02}_{-0.02}$
BI_{ds3567}	cts/(keV·kg·y)	1.26 ± 0.02	$1.26^{+0.01}_{-0.02}$
m_{ds3522}	1/keV	-0.07 ± 0.03	$-0.06^{+0.02}_{-0.03}$
m_{ds3552}	1/keV	-0.06 ± 0.03	$-0.06^{+0.03}_{-0.03}$
m_{ds3555}	1/keV	-0.08 ± 0.03	$-0.08^{+0.03}_{-0.03}$
m_{ds3564}	1/keV	-0.04 ± 0.03	$-0.04^{+0.03}_{-0.03}$
m_{ds3567}	1/keV	-0.12 ± 0.03	$-0.12^{+0.03}_{-0.03}$
Γ_{Mn}	cts/(kg·y)	15.3 ± 0.7	$15.3^{+0.7}_{-0.7}$
Γ_{Tl}	cts/(kg·y)	0.5 ± 0.2	$0.5^{+0.2}_{-0.2}$

TABLE 6.24: Results of background-only fit on data. These values were used to simulate 10^4 toyMC of the CUORE experiment for the extraction of the median exclusion sensitivity.

Chapter 7

Conclusion

My PhD work was focused on the search of the $0\nu\beta\beta$ decay of ^{128}Te. I developed a software dedicated to the study of this process: the analysis is based on a Bayesian statistics approach, and a binned fit is performed on the ROI spectrum of the CUORE data for a total exposure of 309.33 kg·y. I found no evidence for this decay, and with this analysis it was possible to set the most stringent 90% C.I. limits on the signal rate and on the half life of this process currently in literature:

$$\Gamma_{0\nu} < 1.9 \cdot 10^{-25}\ y^{-1} \tag{7.1}$$

$$T_{1/2}^{0\nu} > 3.6 \cdot 10^{24}\ y \tag{7.2}$$

This upper limit on the ^{128}Te $0\nu\beta\beta$ decay half life improves by a factor ∼33 the previous limit of $1.1 \cdot 10^{23}$ y that was obtained by MiDBD in 2003. For the first time, a direct experiment is setting limits that also overcome those obtained from geochemical experiments, whose latest estimate of the ^{128}Te $\beta\beta$ decay half life is $(2.2 \pm 0.3) \cdot 10^{24}$ y. This technique only measures the parent/daughter nuclei ratio present in geological samples and thus cannot distinguish between the double beta decay modes ($2\nu\beta\beta$ or $0\nu\beta\beta$ decay, to the ground state or to the excited states).

To complete this work, I performed the study of the CUORE exclusion sensitivity to this process with the analyzed exposure: the obtained median limit setting sensitivity is given by

$$\hat{T}_{1/2}^{0\nu} = 2.2 \cdot 10^{24}\ y \tag{7.3}$$

and the probability of getting a more stringent limit with respect to the achieved one turns out to be 8.8%. The presented results do not include the systematic uncertainties, that will be subject of further analysis and will be then published by the CUORE Collaboration.

Before getting into these results, I acquired experience on different aspects of the CUORE experiment, and I gave my contribution to three main activities: the detector optimization, the data processing and the background modelling.

I contributed to the on-site detector operation aimed at providing the optimal data taking conditions: in particular, I was responsible for the CUORE detector noise abatement procedure exploiting the destructive interference of the relative Pulse Tubes (PT) phases. The PT valve rotation and the He gas pulsation introduce vibrations at 1.4 Hz and related harmonics in the CUORE apparatus: the combination of this effect from 4 simultaneously operating PT can disrupt the detector performance. This downside is significantly reduced with the active noise cancellation technique I periodically performed on CUORE: this consists of driving the relative PT phases and performing dedicated data acquisitions to evaluate the detector noise at each phase configuration, with the aim of identifying the one that minimizes the noise. Keeping the minimum noise configuration is an essential ingredient for improved data quality and detector energy resolution.

During the acquisition of more than one third of the data used to extract the presented ^{128}Te limits and the last published CUORE results on ^{130}Te, I took care of the online data processing and monitoring, with the aim of providing the Collaboration a quick but reliable feedback on the quality and stability of the acquired data. In this framework, I became expert in handling the whole analysis sequence that leads the raw data to the higher level analysis.

In addition, I took part to the CUORE Background Model working group, a small group of collaborators whose purpose is to investigate the phenomena that contribute to the CUORE measured spectrum. This study includes the identification of the radioactive contaminations, their activity and position in the detector, the decay chains secular equilibrium conditions. In this group I provided an original contribution towards a better comprehension of the alpha region of the CUORE spectrum, whose reconstruction has always been particularly challenging in terms of understanding the bolometric detector response to energy depositions from these particles, and of modelling the non-ideal surface contamination profile. It was observed in CUORE and previously by its predecessors operating TeO_2 crystals that the signal amplitude due to the energy released by alpha particles is slightly higher than expected from the γ calibration; as a consequence, the reconstructed energy of the alpha peaks is shifted towards higher energies. My contribution consisted of an accurate identification of all the lines contributing to the alpha energy region, followed by the investigation and quantification of this effect (α *quenching*) in the CUORE detectors. In parallel with this, I performed the study of the secular equilibrium in the ^{238}U radioactive chain, and I identified the present breaking points. This study could not be performed for the ^{232}Th chain isotopes, since only few lines are visible in the CUORE spectrum. Both the information on the α *quenching* and on the radioactive chains secular equilibrium breaking points aim at improving the present CUORE Background Model.

The CUORE experiment demonstrated the feasibility of operating a ton-scale array of cryogenic bolometers in reliable and stable conditions. The data taking is currently proceeding with an average rate of 50 kg·y per month; at the end of 2020, the milestone of 1 ton·y collected exposure was accomplished. CUORE is scheduled to take data for

5 years live time, corresponding to $\sim$3.7 ton$\cdot$y exposure; this unprecedented amount of accumulated data with TeO_2 crystals makes CUORE one of the leading experiments in the search of the $0\nu\beta\beta$ decay of ^{130}Te, and, as demonstrated by this PhD thesis work, of ^{128}Te as well.

Appendix A

Overview on Bayesian Statistics

In the Bayesian approach to statistics, the probability of a given observable is intended as a measure of the degree of belief of a parameter[123], expressed through a combination of conditional probabilities ruled by the Bayes theorem:

$$P(B) \cdot P(A|B) = P(B|A) \cdot P(A) \tag{A.1}$$

This concept of probability is applied both on observables, such as data, and on hypotheses. One of the most interesting aspects of making probability statements in this context is that information from independent past measurements can be included: the conditional probability of an observable given some measured data can be evaluated from the probability of measuring those data given the observable (*likelihood*), and from the previous knowledge on the observable itself (*prior probability*). The Bayes Theorem provides a straightforward expression of this statement: given the observed data D and a model M described by a set of parameters $\vec{\theta}$, the conditional probability of $\vec{\theta}$ given the data is written as

$$P(\vec{\theta}|D,M) = \frac{\mathscr{L}(D|\vec{\theta},M)\,\pi(\vec{\theta})}{\int_{\Theta}\mathscr{L}(D|\vec{\theta},M)\,\pi(\vec{\theta})\,d\vec{\theta}} \tag{A.2}$$

where the terms assume the following meanings:

- $P(\vec{\theta}|D,M)$ is the *Posterior Probability*, namely the probability of the parameters after observing the data;
- $\mathscr{L}(D|\vec{\theta},M)$ is the *Likelihood Function*, which represents the probability of the data assuming the model is described by $\vec{\theta}$;
- $\pi(\vec{\theta})$ is the *Prior Probability*, describing the previous knowledge of the parameters, before observing the data D;
- the denominator is a normalization involving the integral over the whole parameters space Θ.

The probability is then subjective, since there is no a unique prescription for priors. In this inference, the probability density function of a model can be updated whenever data from a new experiment are available, since a posterior probability obtained from a past independent analysis can be used as a prior for the new one. In case of no specific previous information on the hypothesis probability, a uniform distribution is chosen as prior.

To make a statistical inference on the parameter of interest, the value of its point estimator is taken. An example of point estimator $\hat{\Gamma}$ for the parameter Γ is the maximum of the marginalized posterior probability:

$$\hat{\Gamma} = \max P(\Gamma|D, M) = \max \int_{\Theta, \theta \neq \Gamma} P(\vec{\theta}|D, M) \tag{A.3}$$

The integral of the posterior probability distribution is performed over the whole parameter space but the parameter of interest. The other parameters of the model are called *nuisance parameters*.

A.1 Markov Chain Monte Carlo

Let us consider a posterior probability $P(\vec{\theta}|D)$ and an arbitrary function $g(\vec{\theta})$ having a finite expectation value under P[124]:

$$E_P[g] = \int P(\vec{\theta}|D) g(\vec{\theta}) d\vec{\theta} < \infty \tag{A.4}$$

The *fundamental Monte Carlo principle* states that a set of independent or correlated samples $\vec{\theta}_i$ with i=1...N from the posterior P, i.e. such that $\vec{\theta}_i$ are approximately distributed as P, is sufficient to obtain an estimate of the expectation value:

$$\hat{E}_P[g] \approx \frac{1}{N} \sum_{i=1}^{N} g(\vec{\theta}_i) \tag{A.5}$$

In Bayesian analysis it is common to deal with multi-dimensional problems, specifically with posterior distributions depending on several parameters, and usually the analyst is interested in making a statistical inference on them separately. This implies integrating the multi-dimensional posterior distribution over all the parameters but the interesting one. In general, this operation cannot be done analytically, thus numerical integration techniques are used. The Monte Carlo method is one of the most powerful at $d > 3$ parameters, since its complexity does not depend on the dimension d. In this framework, if one is interested in the marginalized posterior of one parameter θ_1 among $\vec{\theta}$, this can be estimated starting from the full posterior and taking a $g(\vec{\theta})$ in the A.5 where the other parameters are simply ignored:

$$g(\vec{\theta}) = \begin{cases} 1 & \theta = \theta_1 \\ 0 & \text{otherwise} \end{cases} \tag{A.6}$$

The major advantage of the Monte Carlo method in Bayesian statistics is then that by sampling the full posterior it is possible to access to the marginalized posterior distribution of each parameter.

The Markov Chain Monte Carlo (MCMC) is a procedure that is frequently used in the numerical implementation of a Bayesian analysis for the posterior sampling. A Markov Chain is a stochastic model performing a sequence of slightly correlated samples, such that the probability of each is only dependent on that of the immediately previous one:

$$P(\vec{\theta}_{t+1}|\vec{\theta}_t, \vec{\theta}_{t-1}, ..., \vec{\theta} = P(\vec{\theta}_{t+1}|\vec{\theta}_t) \tag{A.7}$$

The rule dictating how to move from one point to another in the parameters space can be defined by different algorithms: two examples are the Gibbs sampling and the Metropolis-Hasting algorithm[97][122]. The first is used in CUORE for the MCMC sampling in the Bayesian analysis of the Background Model construction (sec. 4.2), and the second is employed in the $0\nu\beta\beta$ decay analyses (sec. 5.1 and 6.3).

Appendix B

From Binned to Unbinned Extended Maximum Likelihood

In the following paragraph, the equivalence of building an unbinned extended maximum likelihood and a binned likelihood in the limit of small bin size will be described.

Let us consider a set of data $\vec{x}$ distributed according a probability density function $f(\vec{x})$. Let us bin the domain of this function with a number M of bins: the number n_i of events into the i-th bin is a random variable distributed as a Poissonian. The binned Likelihood function assumes the form:

$$\mathscr{L}_B(\vec{x}|f,\mu) = \prod_{i=1}^{M} \frac{\mu_i^{n_i} e^{-\mu_i}}{n_i!} \tag{B.1}$$

where μ_i is the expectation value for the i-th bin.

Let now us choose M large enough such that every bin contains 0 or 1 event and the probability for more that 1 event per bin is very close to 0. In this case, the number of events per bin can only be $n_i = 0, 1$. Let us call M_1 the number of bins containing 1 event and M_0 the number of bins containing 0 events, so that $M = M_1 + M_0$. The binned Likelihood becomes:

$$\begin{aligned}
\mathscr{L}_B(\vec{x}|f,\mu) &= \prod_{i=1}^{M} \frac{\mu_i^{n_i} e^{-\mu_i}}{n_i!} = \prod_{i=1}^{M_1} \frac{\mu_i^{n_i} e^{-\mu_i}}{n_i!} \prod_{j=1}^{M_0} \frac{\mu_j^{n_j} e^{-\mu_j}}{n_j!} = \\
&= \prod_{i=1}^{M_1} \frac{\mu_i^{1} e^{-\mu_i}}{1!} \prod_{j=1}^{M_0} \frac{\mu_j^{0} e^{-\mu_j}}{0!} = \prod_{i=1}^{M_1} \mu_i e^{-\mu_i} \prod_{j=1}^{M_0} e^{-\mu_j} = \\
&= \prod_{i=1}^{M_1} \mu_i \prod_{i=1}^{M_1} e^{-\mu_i} \prod_{j=1}^{M_0} e^{-\mu_j} = \prod_{i=1}^{M_1} \mu_i \prod_{m=1}^{M} e^{-\mu_m} = e^{-\mu} \prod_{i=1}^{M_1} \mu_i
\end{aligned} \tag{B.2}$$

where μ is the expected total number of counts. Moving to the more convenient log-Likelihood, we get:

$$\log \mathscr{L}_B(\vec{x}|f,\mu) = -\mu + \sum_{i=1}^{M_1} \log \mu_i \quad . \tag{B.3}$$

Let us now construct an unbinned extended likelihood as a poissonian probability of measuring n counts while expecting μ, multiplied by the product of the probability density function f evaluated on each data sample x_i:

$$\mathscr{L}_U = \frac{\mu^n e^{-\mu}}{n!} \prod_i f(x_i) \tag{B.4}$$

For the log-Likelihood, we get:

$$\begin{aligned} \log \mathscr{L}_U &= \log \frac{\mu^n e^{-\mu}}{n!} + \log \prod_i f(x_i) = \\ &= n \log \mu - \mu - \log n! + \sum_i \log f(x_i) \end{aligned} \tag{B.5}$$

Let us now introduce a binning with a very small bin width ϵ, such that the number of events per bin can be again only 0 or 1. In this frame, the expectation value μ_i for the i-th bin gets closer to 0 as ϵ also does. Being $\mu_i/\mu = f(x_i)\,\epsilon$, the unbinned log-Likelihood becomes:

$$\begin{aligned} \log \mathscr{L}_U &= n \log \mu - \mu - \log n! + \sum_i \frac{\mu_i}{\mu}\frac{1}{\epsilon} = \\ &= n \log \mu - \mu - \log n! - n \log \mu + \sum_i \log \mu_i - \sum_i \log \epsilon \end{aligned} \tag{B.6}$$

The terms $\log n!$ and $\sum_i \log \epsilon$ can be collected to a constant term and $n \log \mu$ vanishes, therefore we obtain this expression for the unbinned extended log-Likelihood:

$$\log \mathscr{L}_U = -\mu + \sum_i \log \mu_i + const \tag{B.7}$$

This equation B.7 is equivalent to the eq. B.3, up to a constant. From this comparison, it is straightforward that constructing a binned likelihood in the small bin size limit is equivalent to build an unbinned extended likelihood as in eq. B.4. This feature turns out to be very useful for the computational implementation of the likelihood function when an ubinned fit has to be performed.

List of Abbreviations

$0\nu\beta\beta$	Neutrinoless double beta decay
$2\nu\beta\beta$	Two-neutrino double beta decay
BM	Background Model
CMB	Cosmic Microwave Background
CUORE	Cryogenic Underground Observatory for Rare Events
CUPID	CUORE Upgrade with Particle IDentification
DAQ	Data AcQuisition
DCS	Detector Calibration System
EDCS	External Detector Calibration System
EDF	Energy Density Functional
DR	Dilution Refrigerator
DU	Dilution Unit
FWHM	Full Width Half Maximum (energy resolution)
HEX	Heat EXchanger
IBM	Interacting Boson Model
ISM	Interacting Shell Model
IH	Inverted Hierarchy
INFN	Istituto Nazionale di Fisica Nucleare
ISM	Interacting Shell Model
NSM	Nuclear Shell Model
IVC	Inner Vacuum Chamber
LNGS	Laboratori Nazionali del Gran Sasso
MC	Mixing Chamber or Monte Carlo (distinguishable context)
MiDBD	Milan Double Beta Decay (experiment)
MIT	Metal-Insulator Transition
MSP	Main Support Plate
NH	Normal Hierarchy
NME	Nuclear Matrix Element
NTD	Neutron Transmutation Doping/ed (technique/sensor)
OF	Optimum Filter
OFE	Oxygen-Free Electrolytic (copper) (OFHC C10100)
OFHC	Oxygen-Free High thermal Conductivity (copper)
OVC	Outer Vacuum Chamber
pdf	Probability Density Function
PT	Pulse Tube (refrigerator)
PTFE	PolyTetraFluoroEthene
QRPA	Quasiparticle Random Phase Approximation
ROI	Region Of Interest
RMS	Root Mean Square
SM	Standard Model
TSP	Tower Support Plate
TVL	Test Variable Left
TVR	Test Variable Right
UEML	Unbinned Extended Maximum Likelihood (fit)

List of Figures and Tables

Acknowledgements / Ringraziamenti

Ecco che finalmente mi appresto a scrivere la parte della tesi che verrà letta da più persone.
I Ringraziamenti.
The Acknowledgments.
Ci sono sempre un sacco di aspettative sui ringraziamenti. Quante volte mi sono chiesta: quando li scriverò? In che lingua? Chi dimenticherò? Quanto dovrebbero essere lunghi?
Mi sono detta: è un momento importante, in cui dovrò ripercorrere questi anni. Dovrò farlo con calma.
E invece, come è mio solito, sono qui alle undici di sera di domenica, a ridosso della consegna finalissima. Ma forse è mennlio così: dopotutto, c'è davvero bisogno di pensarci così tanto? I fatti e le persone che hanno lasciato il segno verranno da sé. Seguirò il mio flusso di coscienza.
Sì, è la cosa minnliore.
Inizierò con i miei super-supervisors, Oliviero e Paolo, due persone che in questi anni sono state per me guide, esempi, punti di riferimento in vari modi. Grazie, perchè (cosa tutt'altro che scontata) ho sempre potuto contare su di voi. Oliviero (©), nonostatante la distanza fisica, nonostante i tuoi numerosissimi impegni hai sempre trovato il tempo di essere presente - di esserlo davvero -, di insegnarmi una montagna di cose, di ascoltarmi tutte le volte (tante!) che ho avuto bisogno di aiuto, di scambiare idee, o di essere incoraggiata. Paolo, ti ricordi la mia minaccia profetica durante la tesi magistrale "io entrerò al GSSI e tu sarai il mio supervisor"? Ero serissima! Il tuo incubo. Grazie, perchè le mie svolte di produttività maggiori sono state sempre dopo un qualche tuo big statement: tra i minnliori vorrei ricordare "da oggi lavorerai ogni giorno, ti riposerai due volte, di cui una è Natale e l'altra devo ancora decidere" oppure, vedendomi appena appena esaurita "non è forse il caso di... ruotare le attività? Esci, fai qualcosa" e io sono uscita a fare la spesa. E ti ho fatto allungare i pranzi, VI ho fatto allungare i pranzi. Sì, perchè tutto il nostro gruppo dei laboratori ha dovuto estendere le pause pranzo! Grazie per aspettarmi sempre, bullizzandomi un po'.. ma alla fine restate sempre là! Questa cosa è particolarmente apprezzata da Carlo. Grazie Carlo, perchè oltre ad aspettarmi a pranzo, anche tu ci sei sempre stato e mi hai insegnato tantissime cose. Far parte di questo gruppo è per me come far parte di una faminnlia.

Ringrazio Nello e Laura, amici veri e riferimenti costanti, per un milione di cose che non posso elencare altrimenti non finirei mai più. Quindi cercherò di riassumere le minnliori: quante giornate fuori, in galleria, consinnli, arrosticini, corse, ciao sono Dory, allenamenti, partitazze a tennis? Quante GRINNLIATE? Quanti calzini tirati, calzini parati, autoinviti, spiegazioni, insegnamenti, passeggiate, sbevazzate, risate fino a sentirsi male? Quanti? Non lo so. Un numero in crescita inesorabile.
Ringrazio ora una persona senza la quale questo lavoro non sarebbe esistito. I mean, literally. Grazie Giovanni. Non vedevi l'ora che arrivassero i ringraziamenti, sei contento? Spero che saranno anche mennlio delle aspettative. Grazie per avermi insegnato BAT da zero, per aver ascoltato e sciolto i miei dubbi più strampalati e per essere diventato il Grande Mago Sbacatore. Grazie per tutti nnli aneddoti di vita tua e di gente che a volte manco so chi è ma fa sempre ridere, anche quando li racconti la terza volta perchè Ciao sono Dory. Grazie anche per lo scherzo più terrificante della storia con complici Guido e pure Paolo (che almeno poi mi ha consolata), perchè anche se mi avete fatto piangere - MANNAGGIA A VOI -, ci ripenso e rido tantissimo.
Grazie a Irene: sarai pure a Milano da più di due anni ma per me appartieni ai laboratori, no way! Grazie per avermi insegnato tantissime cose, per esserci sempre nonostante la distanza (nnli amici veri non si accorgono nemmeno!), per avermi incoraggiata, sostenuta e capita sempre.
Grazie a Miri e Ste, per le best pause post pranzo e per le centinaia di cioccolatini. Questa tradizione non si deve perdere, SIO lavora per noi. Grazie per aver condiviso con me i momenti importanti. Grazie per nnli scherzoni (penso sempre al mondo parallelo in cui, quel giorno, sono partita con la macchina, Ste è sbucato e ci siamo spiaccicati sul muro della divisione ricerca), per nnli accidenti presi e quelli che mi prenderò (adesso che Stefano ha imparato a salire le scale in silenzio vivo nel terrore...).
Grazie a Lorenzo per i consinnli preziosi sempre pronti, fondamentali, fin dall'inizio di tutto. Noi delle Marche ci spallegiamo sempre.
Grazie a Guido. Non so più per quante cose dovrei ringraziarti, anche qui finirei tra un anno. Grazie per avermi aiutato sempre, lo vonnlio ripetere, sempre. Ti meriti una medannlia. Grazie per le millemila idee scambiate (di ogni tipo) e per aver apprezzato e pubblicato le mie hit. Quando diventeranno famose, la tua tesi avrà una miriade di citazioni! Grazie per i CAVALLO a tradimento, che cerco disperatamente di restituirti ma oh, non ti distrai un attimo. Grazie ad Alice: ci siamo fatte laurea e dottorato in tandem, e ci siamo sostenute mille volte. Non vedo l'ora di poter fare un'altra esplorazione in bici dentro una camera, come a San Francisco! Fuori lo fanno tutti, troppo facile. E ricorda anche che se siamo sopravvissute a New York dopo aver dormito in quel posto, siamo invincibili. Intanto, ci accontentiamo di salire e scendere le scale di Genova con una valigia gigante.
Vorrei poi ringraziare tutto il gruppo di Milano, e in particolare Spozzi, Matteo (bella partita al grande gioco del reprocess, quanti segnalini '???' abbiamo preso?) Tonino, Chiara, Sdello (anche tu, per me apparterrai sempre ai laboratori!). Le mie trasferte a Milano sono sempre state costruttive e anche divertenti, grazie per nnli insegnamenti e i caffè coi

loacker. Spozzi è un'altra persona senza la quale questo lavoro non esisterebbe.. non finirò mai di ringraziarti per tutto ciò che mi hai insegnato, per avermi sempre risposto a tutte le ore, per il cane procione, per TAUP e Sestri, per Giuseppe Verdi, per aver avuto una pazienza infinita! INFINITA! Anche tu ti meriti una medannlia al valore.
Ma poi ragazzi, tutti, vonnliamo parlare delle conferenze e dei meeting?
Vonnliamo farlo?
No, non vonnliamo, non adesso.
Tanta scienza, anche.
Grazie ad Ambretta, con cui ho condiviso ogni giorno di questo percorso. Perchè si inizia insieme e si finisce insieme! Grazie per le ore passate a fare la spesa (che integrate in tre anni e mezzo dovrebbero equivalere a circa 10 giorni di fila a fare la spesa senza mai smettere) per le serate fuori e dentro casa, per sapere sempre dove sta il mio cellulare, per le chiacchierate infinite, nnli allenamenti, i gelati e i gelatini, nnli arrosticini, i sushini, per aver fatto le coatte finte ricche alla Tokyo Tower ("per noi solo dei tramezzini, grazie"), per l'unusual tomato e per 10^{10} cose che non posso riassumere qui. A te, amica mia, va la medannlia di world's best coinquilina.
Un grazie particolare va anche al nostro albero di Natale. Anche lui c'è sempre stato.
Grazie a Massimetto per le chiacchierate (giuro che l'ha fatto, non è tanto per dire!), le condivisioni, le serate e le sorprese. Grazie a tutti nnli alpaca dell'Argentina, di Sulmona e del mondo, ma soprattutto grazie al mio Alpachino. Se Massimetto non me l'avesse portato non sarebbe stato con me ogni secondo durante mio lavoro, a sopportare con me nnli spari in ufficio, a scrivere la tesi, e io non mi sarei mai dottorata.
Grazie a Marianna per i concerti privati di arpa e per tutte le micie, che miao miao purr purr.
Grazie ai membri del gruppo gssi_apAll@lngs.local per aver condiviso il minnlior trash, scientifico e non, in circolazione.
Let me now switch to English for a while. I want to say thank you to my PhD mates, the people that shared with me this adventure: my sister Nandita, that missed the Roma stop with me, taught me the "T" and shared with me the everyday-craziness of the last months of thesis writing. We ate a lot of brains. I thank Fra, for being with me during good and less good moments, for the broken non-broken hearts, for the hugs (you learnt it!) and for lunches and dinners at gssi while writing the thesis. I thank my bro Ashish for the many great moments together and just for being Ashish, and my lovely friend Austin, for his ability of instilling calm and for his infinite kindness; my cement mixer is the symbol of all this! Then, I thank Anto, for the biggest laugh of these years. How many stories have I heard? I don't know, hundreds, and I never get tired of hearing them again and again. Thank you for the funniest hang out days, for the gossip and for making less stressful the long days of thesis writing. I also thank Alessia, the best poker-face you will ever meet. You also had the ability of relieving the hard period of the thesis end; I thank you for being a pink vacuum cleaner from time to time (I am laughing while writing) and for playing with me at "what's the face under the mask?". You know what? Let me NOT thank Eddie

for not offering me the lunch at the canteen, at my birthday. Not kind at all, isn't it?
Grazie ai miei amici di Roma: Micol, Ale, Rich, Fede, Fra e Guido (mi ripeto), Bob, Vin, Pb, Cri, Eug che hanno seguito il mio percorso senza perdersi un giorno.
Ringrazio Claudia, perchè quattro anni fa mi ha fatto entrare nel mondo di CUORE da cui non sono più voluta uscire.
Grazie al GSSI che mi ha dato la possibilità di compiere questo percorso bellissimo e di prendere parte a tutte le iniziative di divulgazione che ho amato.
Grazie a Francesco Vissani, che è stato una guida e un amico.
Grazie a Luciano di 10 anni fa che ha copiato in formato digitale i suoi appunti fantastici del corso di Francesco, sono stati per me illuminanti. Grazie a Luciano di oggi, che mi ha insegnato tante cose.
Grazie alla mia faminnlia che ha sempre creduto in me: in particolare a mamma e nonna Tolita, che hanno preso con me laurea triennale, magistrale e adesso anche il dottorato. Grazie mammina! Sei da sempre il mio esempio, mi hai spinta a seguire la mia passione e mi hai sempre fatto sentire che sei fiera di me. Grazie per avermi insegnato a scalare le montagne (letteralmente)! Questo traguardo è anche tuo! E nonna, quanti passanti fermerai ora? Probabilmente tutti! Grazie per tutte le volte che mi hai ricordato, e mi ricordi, quanto è importante essere forti e non farsi mai scoraggiare. Grazie anche a nonna Anna per avermi sempre capita e perchè, nonna, non sai che soddisfazione mi dai quando mi chiedi di spiegarti le cose!
Ringrazio ora La persona, la mia. Grazie Luca, perché ci sei sempre e da sempre, da vicino e da lontano che era comunque vicino; abbiamo condiviso tutto, hai vissuto con me questo percorso da prima del primo giorno, quando non sapevo cosa avrei fatto "da grande".. hai sempre visto in me qualcosa che io ogni tanto mi perdo per strada, hai riso nella settimana dei lacrimoni, hai sentito le cose più assurde e non ti sei mosso di un millimetro. Non hai smesso di credere in me neanche un secondo, hai sempre saputo che sarei riuscita a cavarmela. Mannaggia a questa maledizione di avere sempre ragione! Devo dirtelo: avevi ragione. Ora però non ti abituare, leggilo qui di tanto in tanto, non mi ripeto. Ho parlato. E ho fatto il gesto definitivo con la mano.
Infine, lascio un messaggio per Valentina del futuro. Vorrei che ti ricordassi, leggendo queste righe, di quante volte in questo periodo hai incontrato ostacoli che credevi insormontabili, e che alla fine hai sempre superato. Di tutte le volte che eri sicura, sicurissima di non capire o non riuscire, ma alla fine l'hai fatto. Quindi, se per caso dovesse venirti ancora in mente, fammi il favore di rileggerti questa tesi dall'inizio alla fine, perché l'hai scritta tu. Keep going!

Bibliography

[1] Ettore Majorana. Teoria simmetrica dell'elettrone e del positrone. *Nuovo Cim.*, 14:171–184, 1937.

[2] E. Akhmedov and S. Esposito. Majorana neutrinos and other majorana particles: theory and experiment. In *The Physics of Ettore Majorana: Theoretical, Mathematical, and Phenomenological*, page 303–353. Cambridge University Press, 2014.

[3] E. Fermi. Tentativo di una teoria dell'emissione dei raggi beta. *Ric. Sci.*, 4:491–495, 1933.

[4] E. Fermi. Tentativo di una Teoria Dei Raggi $\beta. Nuovo\ Cim., 11:1, 1934$.

[5] C. L. Cowan, F. Reines, F. B. Harrison, H. W. Kruse, and A. D. McGuire. Detection of the free neutrino: A Confirmation. *Science*, 124:103–104, 1956.

[6] G. Danby, J.M. Gaillard, Konstantin A. Goulianos, L.M. Lederman, Nari B. Mistry, M. Schwartz, and J. Steinberger. Observation of High-Energy Neutrino Reactions and the Existence of Two Kinds of Neutrinos. *Phys. Rev. Lett.*, 9:36–44, 1962.

[7] K. Kodama et al. Observation of tau neutrino interactions. *Phys. Lett. B*, 504:218–224, 2001.

[8] A. B. McDonald. Nobel Lecture: The Sudbury Neutrino Observatory: Observation of flavor change for solar neutrinos. *Rev.Mod.Phys.*, 88(3):030502, 2016.

[9] T. Kajita, E. Kearns, and M. Shiozawa. Establishing atmospheric neutrino oscillations with Super-Kamiokande. *Nucl. Phys. B*, 908:14–29, 2016.

[10] P. A. Zyla and others (Particle Data Group). *Prog. Theor. Exp. Phys. 2020*, 083C01, 2020.

[11] P. F. de Salas, S. Gariazzo, O. Mena, Ternes C. A., and Tórtola M. Neutrino Mass Ordering From Oscillations and Beyond: 2018 Status and Future Prospects. *Front. Astron. Space Sci.*, 5:36, 2018.

[12] S. Abe et al. Precision Measurement of Neutrino Oscillation Parameters with KamLAND. *Phys. Rev. Lett.*, 100:221803, 2008.

[13] X. Qian and P. Vogel. Neutrino mass hierarchy. *Prog. Part. Nucl. Phys.*, 83:1–30, 2015.

[14] M. Goldhaber, L. Grodzins, and A. W. Sunyar. Helicity of Neutrinos. *Phys. Rev.*, 109:1015–1017, 1958.

[15] L. Pandola. Appunti del corso Frontiere del Modello Standard tenuto dal Dr. F. Vissani. 2010.

[16] F. T. Avignone, S. R. Elliott, and J. Engel. Double Beta Decay, Majorana Neutrinos, and Neutrino Mass. *Rev. Mod. Phys.*, 80:481–516, 2008.

[17] M. Goeppert-Mayer. Double beta-disintegration. *Phys. Rev.*, 48:512–516, 1935.

[18] S. R. Elliott, A. A. Hahn, and M. K. Moe. Direct Evidence for Two Neutrino Double Beta Decay in ^{82}Se. *Phys. Rev. Lett.*, 59:2020–2023, 1987.

[19] Barabash A. S. Precise Half-Life Values for Two-Neutrino Double-β Decay: 2020 review. *Universe*, 6(10):159, 2020.

[20] Laurent Canetti, Marco Drewes, and Mikhail Shaposhnikov. Matter and Antimatter in the Universe. *New J. Phys.*, 14:095012, 2012.

[21] M. A. Luty. Baryogenesis via leptogenesis. *Phys. Rev. D*, 45:455–465, 1992.

[22] B. Pontecorvo. Superweak interactions and double beta decay. *Phys. Lett. B*, 26:630–632, 1968.

[23] M. Mitra, G. Senjanovic, and F. Vissani. Neutrinoless Double Beta Decay and Heavy Sterile Neutrinos. *Nucl. Phys. B*, 856:26–73, 2012.

[24] V. Tello, M. Nemevsek, F. Nesti, G. Senjanovic, and F. Vissani. Left-Right Symmetry: from LHC to Neutrinoless Double Beta Decay. *Phys. Rev. Lett.*, 106:151801, 2011.

[25] S. Dell'Oro, M. Marcocci, S.and Viel, and F. Vissani. Neutrinoless double beta decay: 2015 review. *Adv. High Energy Phys.*, 2016:2162659, 2016.

[26] C. Brofferio, O. Cremonesi, and S. Dell'Oro. Neutrinoless Double Beta Decay Experiments With TeO_2 Low-Temperature Detectors. *Front. Phys.*, 7(86), 2019.

[27] J. Kotila and F. Iachello. Phase space factors for double-β decay. *Phys. Rev. C*, 85:034316, 2012.

[28] J. Engel and J. Menéndez. Status and future of nuclear matrix elements for neutrinoless double-beta decay: a review. *Rep. Prog. Phys.*, 80(4):046301, 2017.

[29] Fedor ˇ Simkovic, Vadim Rodin, Amand Faessler, and Petr Vogel. $0\nu\beta\beta$ and $2\nu\beta\beta$ nuclear matrix elements, quasiparticle random-phase approximation, and isospin symmetry restoration. *Phys. Rev. C*, 87(4):045501, 2013.

[30] Juhani Hyvärinen and Jouni Suhonen. Nuclear matrix elements for $0\nu\beta\beta$ decays with light or heavy Majorana-neutrino exchange. *Phys. Rev. C*, 91(2):024613, 2015.

[31] M.T. Mustonen and J. Engel. Large-scale calculations of the double-β decay of ^{76}Ge,^{130} Te,^{136} Xe, and ^{150}Nd in the deformed self-consistent Skyrme quasiparticle random-phase approximation. *Phys. Rev. C*, 87(6):064302, 2013.

[32] J. Menendez, A. Poves, E. Caurier, and F. Nowacki. Disassembling the Nuclear Matrix Elements of the Neutrinoless beta beta Decay. *Nucl. Phys. A*, 818:139–151, 2009.

[33] Andrei Neacsu and Mihai Horoi. Shell model studies of the ^{130}Te neutrinoless double-beta decay. *Phys. Rev. C*, 91:024309, 2015.

[34] J. Barea, J. Kotila, and F. Iachello. $0\nu\beta\beta$ and $2\nu\beta\beta$ nuclear matrix elements in the interacting boson model with isospin restoration. *Phys. Rev. C*, 91(3):034304, 2015.

[35] S. Dell'Oro, S. Marcocci, M. Viel, and F. Vissani. The contribution of light Majorana neutrinos to neutrinoless double beta decay and cosmology. *J. Cosm. Astropart. Phys.*, 1512:023, 2015.

[36] S. Vagnozzi et al. Unveiling ν secrets with cosmological data: Neutrino masses and mass hierarchy. *Phys. Rev. D*, 96:123503, 2017.

[37] M. A. Fehr, M. Rehkamper, and A. N. Halliday. Application of MC-ICPMS to the precise determination of tellurium isotope compositions in chondrites, iron meteorites and sulfides. *Int. J. Mass Spectrometry*, 232:83–94, 2004.

[38] I. Takashi. First result of the CANDLES III experiment searching for double beta decay of ^{48}Ca. *Proceeding of the Neutrino Conference*, 2018.

[39] M. Agostini et al. Final Results of GERDA on the Search for Neutrinoless Double-β Decay. *Phys. Rev. Lett.*, 125:252502, 2020.

[40] O. Azzolini et al. Final Result of CUPID-0 Phase-I in the Search for the ^{82}Se Neutrinoless Double-β Decay. *Phys. Rev. Lett.*, 123:032501, Jul 2019.

[41] G. Eurin. Search for the double-beta decay of ^{96}Zr with the NEMO-3 detector and ultra-low radioactivity measurements for the SuperNEMO experiment using the BiPo-3 detector. 2015. [Ph. D. thesis, University College London].

[42] E. Armengaud et al. A new limit for neutrinoless double-beta decay of ^{100}Mo from the CUPID-Mo experiment. arXiv:2011.13243v1, 2020.

[43] F. A. Danevich et al. Search for double beta decay of ^{116}Cd with enriched $^{116}CdWO_4$ crystal scintillators (Aurora experiment). *Journal of Physics: Conference Series*, 718, 2016.

[44] C. Arnaboldi et al. A Calorimetric search on double beta decay of ^{130}Te. *Phys. Lett. B*, 557:167–175, 2003.

[45] D. Q. Adams et al. Improved Limit on Neutrinoless Double-Beta Decay in ^{130}Te with CUORE. *Phys. Rev. Lett.*, 124:122501, Mar 2020.

[46] A. Gando et al. Precision Analysis of the ^{136}Xe Two-Neutrino $\beta\beta$ Spectrum in KamLAND-Zen and Its Impact on the Quenching of Nuclear Matrix Elements. *Phys. Rev. Lett.*, 122:192501, 2019.

[47] M. Agostini et al. Upgrade for Phase II of the Gerda Experiment. *Eur. Phys. J. C*, 78:388, 2018.

[48] B. Martìn-Albo et al. The NEXT experiment for neutrinoless double beta decay searches. arXiv:1910.07314, 2019.

[49] M. Ambrosio et al. Vertical muon intensity measured with MACRO at the Gran Sasso Laboratory. *Phys. Rev. D*, 52:3793–3802, 1995.

[50] A. Best, J. Görres, M. Junker, K. L. Kratz, M. Laubenstein, A. Long, S. Nisi, K. Smith, and M. Wiescher. Low energy neutron background in deep underground laboratories. *Nucl. Instrum. Meth. A*, 812:1–6, 2016.

[51] C. Alduino et al. CUORE sensitivity to $0\nu\beta\beta$ decay. *Eur. Phys. J.*, 77(9):532, 2017.

[52] E. Fiorini and T. O. Niinikoski. Low Temperature Calorimetry for Rare Decays. *Nucl. Instrum. Meth. A*, 224:83, 1984.

[53] A. Giuliani et al. A low temperature TeO_2 detector to search for double beta decay of ^{130}Te. *Proc. Joint Int. Lepton Photon Symposium at High Energies (15th) and European Phys. Soc. Conf. on High-energy Phys.*, pages 670–672, 1991.

[54] A. Alessandrello et al. Large mass, low temperature, low background detectors. *Nucl. Instrum. Meth. A*, 315:263–266, 1992.

[55] A. Alessandrello et al. Milano experiment on $0-\nu\ \beta\beta$ decay of ^{130}Te with a thermal detector. *Nucl. Phys. B (Proc. Suppl.)*, 31:83–87, 1993.

[56] E. Fiorini. CUORE: A cryogenic underground observatory for rare events. *Phys. Rep.*, 307:309–317, 1998.

[57] C. Alduino et al. CUORE-0 detector: design, construction and operation. *J. Instrum.*, 11(07):P07009, 2016.

[58] D. R. Artusa et al. Initial performance of the CUORE-0 experiment. *Eur. Phys. J. C*, 74(8):2956, 2014.

[59] K. Alfonso et al. Search for Neutrinoless Double-Beta Decay of ^{130}Te with CUORE-0. *Phys. Rev. Lett.*, 115(10):102502, 2015.

[60] J. C. Mather. Bolometer noise: nonequilibrium theory. *Appl. Opt.*, 21(6):1125–1129, 1982.

[61] C. Enss. *Cryogenic Particle Detection.* Springer, 2005.

[62] B. I. Shklovskii and A. L. Efros. *Electronic Properties of Doped Semiconductors.* Springer, 1984.

[63] E. E. Haller, N. P. Palaio, M. Rodder, W. L. Hansen, and E. Kreysa. Ntd germanium: A novel material for low temperature bolometers. In R. D. Larrabee, editor, *Neutron Transmutation Doping of Semiconductor Materials*, pages 21–36. Springer US, 1984.

[64] M. Redshaw, B. J. Mount, E.G. Myers, and F. T. Avignone. Masses of Te-130 and Xe-130 and Double-beta-Decay Q Value of Te-130. *Phys. Rev. Lett.*, 102:212502, 2009.

[65] N. D. Scielzo et al. Double-beta decay Q values of Te-13-, Te-128, and Te-120. *Phys. Rev. C*, 80:025501, 2009.

[66] S. Rahaman, V. V. Elomaa, T. Eronen, J. Hakala, A. Jokinen, A. Kankainen, J. Rissanen, J. Suhonen, C. Weber, and J. Äystö. Double-beta decay Q values of ^{116}Cd and ^{130}Te. *Phys. Lett. B*, 703:412–416, 2011.

[67] M. Barucci, C. Brofferio, A. Giuliani, E. Gottardi, I. Peroni, and G. Ventura. Measurement of Low Temperature Specific Heat of Crystalline TeO_2 for the Optimization of Bolometric Detectors. *J. Low Temp. Phys.*, 123(5-6):303–314, 2001.

[68] C. Arnaboldi et al. Production of high purity TeO_2 single crystals for the study of neutrinoless double beta decay. *J. Cryst. Growth*, 312(20):2999–3008, 2010.

[69] E. Buccheri, M. Capodiferro, S. Morganti, F. Orio, A. Pelosi, and V. Pettinacci. An assembly line for the construction of ultra-radio-pure detectors. *Nucl. Instrum. Meth. A*, 768:130–140, 2014.

[70] G. Benato et al. Radon-free environment for the installation of the CUORE $0\nu\beta\beta$ decay detector. 2017.

[71] M. Schwark, F. Pobell, W. P. Halperin, C. Buchal, J. Hanssen, M. Kubota, and R. M. Mueller. Ortho-para conversion of hydrogen in copper as origin of time-dependent heat leaks. *J. Low Temp. Phys.*, 53:685–694, 1983.

[72] M. Koláč, B. S. Neganov, and S. Sahling. Low Temperature Heat Release from Copper: Ortho-Para Conversion of Hydrogen. *J. Low Temp. Phys.*, 59:547–559, 1985.

[73] A. D'Addabbo et al. The CUORE cryostat. *J. Low Temp. Phys.*, 193:867–875, 2018.

[74] N. Nosengo. Roman ingots to shield particle detector. *Nature*.

[75] A. Alessandrello et al. Measurements on radioactivity of ancient roman lead to be used as shield in searches for rare events. *Nucl. Instrum. Meth. B*, 61:106–117, 1991.

[76] A.T.A.M. de Waele. Pulse-tube refrigerators: principle, recent developments, and prospects. *Physica B Condens. Matter*, 280:479–482, 2000.

[77] A. D'Addabbo et al. An active noise cancellation technique for the CUORE Pulse Tube Cryocoolers. *Cryogenics*, 93:56–65, 2018.

[78] V. Dompè et al. The CUORE Pulse Tube Noise Cancellation Technique. *J. Low Temp. Phys.*, 200:286–294, 2020.

[79] C. Enss and H. Siegfried. *Low Temperature Physics*. Springer, 2005.

[80] S. Copello, C. Branca, A. Caminata, L. Canonica, S. Di Domizio, A. Giachero, E. Guardincerri, L. Marini, M. Pallavicini, and M. Vignati. The CUORE Data Acquisition System. *J. Low Temp. Phys.*, 199, 2020.

[81] C. Arnaboldi, P. Carniti, L. Cassina, C. Gotti, X. Liu, M. Maino, G. Pessina, C. Rosenfeld, and B. X. Zhu. A front-end electronic system for large arrays of bolometers. *J. Instrum.*, 13:P02026, 2018.

[82] S. Di Domizio, C. Branca, A. Caminata, L. Canonica, S. Copello, A. Giachero, E. Guardincerri, L. Marini, M. Pallavicini, and M. Vignati. A data acquisition and control system for large mass bolometer arrays. *J. Instrum.*, 13:P12003, 2018.

[83] S. Di Domizio, S. Orio, and M. Vignati. Lowering the energy threshold of large-mass bolometric detectors. *Journal of Instrumentation*, 6(02):P02007–P02007, feb 2011.

[84] V. Dompè et al. Perspectives of lowering CUORE thresholds with Optimum Trigger. *Proceedings of International Nuclear Physics Conference 2019 in J. Phys. Conf. Ser.*, 1643, 2020.

[85] C. Alduino et al. Analysis techniques for the evaluation of the neutrinoless double-β decay lifetime in ^{130}Te with the CUORE-0 detector. *Phys. Rev. C*, 93:045503, 2016.

[86] M. J. Oreglia. A study of the reactions $\psi' \rightarrow \gamma\gamma\psi$. 1980. [Ph. D. thesis - Appendix D, Stanford Linear Accelerator Center, Stanford University, California].

[87] P. C. Mahalanobis. On the generalised distance in statistics. *Proc. Natl. Inst. Sci. India*, 49, 1936.

[88] R. De Maesschalck, D. Jouan-Rimbaud, and D. L. Massart. The mahalanobis distance. *Chemometr. Intell. Lab. Syst.*, 50(1):1–18, 2000.

[89] C. Alduino et al. The projected background for the CUORE experiment. *Eur. Phys. J. C*, 77(8):543, 2017.

[90] C. Alduino et al. Measurement of the Two-Neutrino Double Beta Decay Half-life of ^{130}Te with the CUORE-0 Experiment. *Eur. Phys. J. C*, 77(1):13, 2017.

[91] S. Agostinelli et al. Geant4 a simulation toolkit. *Nuclear Instruments and Methods in Physics Research Section A: Accelerators, Spectrometers, Detectors and Associated Equipment*, 506(3):250 – 303, 2003.

[92] M. Doi, T. Kotani, H. Nishiura, and E. Takasugi. Double beta decay. *Prog. Theor. Phys.*, 69:602, 1983.

[93] W. C Haxton and J. C. Stephenson. Double beta decay. *Prog. Part. Nucl. Phys.*, 12:409–479, 1984.

[94] S. Pozzi. Search for double-beta decay of ^{130}Te to the excited states of ^{130}Xe in cuore-0. 2017. [PhD thesis, Università degli Studi di Milano-Bicocca].

[95] V. Dompè et al. Study on the contributions to the CUORE energy spectra. *16th International Conference on Topics in Astroparticle and Underground Physics (TAUP 2019) in J. Phys. Conf. Ser.*, 1468, 2020.

[96] D. Q. Adams et al. Measurement of the $2\nu\beta\beta$ Decay Half-life of ^{130}Te with CUORE. arXiv:2012.11749v1, 2020.

[97] A. Gelman, J. B. Carlin, H. S. Stern, and D. B. Rubin. *Bayesian Data Analysis.* Chapman and Hall/CRC Press, Boca Raton, FL, 2014.

[98] Martyn Plummer et al. Jags: A program for analysis of bayesian graphical models using gibbs sampling. In *Proceedings of the 3rd international workshop on distributed statistical computing*, volume 124, pages 1–10. Vienna, Austria, 2003.

[99] Chiara Brofferio and Stefano Dell'Oro. Contributed Review: The saga of neutrinoless double beta decay search with TeO_2 thermal detectors. *Rev. Sci. Instrum.*, 89(12):121502, 2018.

[100] A. Alessandrello, C. Brofferio, D.V. Camin, P. Caspani, P. Colling, O. Cremonesi, E. Fiorini, A. Giuliani, A. Nucciotti, M. Pavan, G. Pessina, E. Previtali, L. Zanotti, and C. Bucci. The thermal detection efficiency for recoils induced by low energy nuclear reactions, neutrinos or weakly interacting massive particles. *Phys. Lett. B*, 408(1):465–468, 1997.

[101] A. Alessandrello, C. Brofferio, D.V. Camin, P. Caspani, P. Colling, O. Cremonesi, E. Fiorini, A. Giuliani, A. Nucciotti, M. Pavan, G. Pessina, E. Previtali, L. Zanotti, and C. Bucci. The bolometers as nuclear recoil detectors. *Nucl. Instrum. Methods Phys. Res. A*, 409(1-3):451–453, 1998.

[102] F. Bellini, M. Biassoni, C. Bucci, N. Casali, I. Dafinei, Z. Ge, P. Gorla, F. Ferroni, F. Orio, C. Tomei, M. Vignati, and Y. Zhu. Response of a teo_2 bolometer to α particles. *J. Inst.*, 5:P12005, 2010.

[103] S. Y. F. Chu, L. P. Ekström, and R. B. Firestone. The lund/lbnl nuclear data search. http://nucleardata.nuclear.lu.se/toi/.

[104] M. Biassoni, S. Capelli, O. Cremonesi, D. Chiesa, L. Gironi, M. Pavan, and M. Sisti. CUORE-0 Background Reconstruction. Internal note (unpublished), 2016.

[105] M. Vignati. Model of the response function of large mass bolometric detectors. *J. Appl. Phys.*, 108:084903, 2010.

[106] C. Alduino et al. First Results from CUORE: A Search for Lepton Number Violation via $0\nu\beta\beta$ Decay of ^{130}Te. *Phys. Rev. Lett.*, 120:132501, Mar 2018.

[107] C. et al. Alduino. Analysis techniques for the evaluation of the neutrinoless double-β decay lifetime in ^{130}Te with the cuore-0 detector. *Phys. Rev. C*, 93:045503, Apr 2016.

[108] A. D. Bryant. A Search for Neutrinoless Double Beta Decay of ^{130}Te. 2010. [Ph. D. thesis, University of California, Berkeley].

[109] A. Drobizhev and L. Marini. CUORE line shape. Internal note (unpublished), 2018.

[110] R. Huang. CUORE Calibration Lineshape Fitting Procedure. Internal note (unpublished), 2020.

[111] J. Kotila and F. Iachello. Phase space factors for double-β decay. *Phys. Rev.*, C85:034316, 2012.

[112] G. Benato, A. Campani, and G. Fantini. $0\nu\beta\beta$ decay analysis - PRL 2019. Internal note (unpublished), 2020.

[113] O. Moreno, R. Álvarez Rodríguez, P. Sarriguren, E. Moya de Guerra, F. Šimkovic, and A. Faessler. Single- and low-lying-states dominance in two-neutrino double-beta decay. *J. Phys. G: Nucl. Part. Phys.*, 36(1):015106, 2008.

[114] F. Šimkovic, R. Dvornický, D. Štefánik, and A. Faessler. Improved description of the $2\nu\beta\beta$-decay and a possibility to determine the effective axial-vector coupling constant. *Phys. Rev. C*, 97:034315, 2018.

[115] P. Domin, S. Kovalenko, F. Šimkovic, and S. V. Semenov. Neutrino accompanied $\beta^\pm\beta^\pm$, β^+/ec and ec/ec processes within single state dominance hypothesis. *Nucl. Phys. A*, 753(3-4):337–363, 2005.

[116] R. Arnold et al. Measurement of the Double Beta Decay Half-life of ^{130}Te with the NEMO-3 Detector. *Phys. Rev. Lett.*, 107:062504, 2011.

[117] S. M. Bilenky and C. Giunti. Neutrinoless Double-Beta Decay: a Probe of Physics Beyond the Standard Model. *Int. J. Mod. Phys. A*, 30(04n05):1530001, 2015.

[118] F. Deppisch and H. Päs. Pinning down the mechanism of neutrinoless double β decay with measurements in different nuclei. *Phys. Rev. Lett.*, 98:232501, 2007.

[119] S. M. Bilenky and J. A. Grifols. The possible test of the calculations of nuclear matrix elements of the $(\beta\beta)_{0\nu}$-decay. *Phys. Lett. B*, 550(3-4):154–159, 2002.

[120] M. Wang, G. Audi, F.G. Kondev, W.J. Huang, S. Naimi, and X. Xu. The Ame2016 atomic mass evaluation (II). Tables, graphs and references. *Ch. Phys. C*, 41(3):030003, 2017.

[121] A. S. Barabash. Average and recommended half-life values for two-neutrino double beta decay. *Nuc. Phys. A*, 935:52–64, 2015.

[122] A. Caldwell, D. Kollar, and K. Kroninger. BAT - The Bayesian Analysis Toolkit. *Computer Physics Communications*, 180(11):2197 – 2209, 2009.

[123] G. Cowan. *Statistical Data Analysis.* Clarendon Press - Oxford, 1998.

[124] *BAT manual Documentation*, https://bat.github.io/bat-docs/master/manual/html/cha-mcmc.html.